Air conditioning with TBAB clathrate hydrate slurry as distribution fluid.

L.E.T. Pronk

TU Delft

Delft
University of
Technology

Challenge the future

AIR CONDITIONING WITH TBAB CLATHRATE HYDRATE SLURRY AS DISTRIBUTION FLUID.

by

L.E.T. Pronk

in partial fulfillment of the requirements for the degree of

Master of Science

in Mechanical Engineering

at the Delft University of Technology,
to be defended publicly on Thursday June 22, 2017 at 14:00.

Student number: 4160622
Supervisor: Dr. ir. C. A. Infante Ferreira
                      Dr. ir. H. Zhou

Thesis committee:	Prof. dr. ir. T. J. H. Vlugt	TU Delft
	Dr. ir. C. A. Infante Ferreira	TU Delft
	Dr. W. G. Haije	TU Delft
	Ir. S. Lobregt	Sparkling Projects

TUDelft
Delft
University of
Technology

ABSTRACT

At the moment, the worldwide demand for air conditioning is rapidly growing, and it is expected to exceed the demand for space heating by the 2060s. However, traditional refrigerants such as CFCs and HCFCs are regulated or phased out by the Montreal and Kyoto protocol. Secondary loop refrigerant systems use less of these harmful refrigerants since they make use of a distribution fluid (for example water) as transport medium between the chiller and the coolers. The efficiency of these systems can be improved by using a phase change material as a secondary refrigerant.

Tetra-n-butylammonium bromide (TBAB) is a promising phase change material for air conditioning applications. TBAB is a white powder that has a good solubility in water. If the solution is cooled down to below it crystallization temperature then TBAB hydrates are produced at a almost constant temperature of 0-12.5 °C depending on the TBAB concentration. This has as advantage that for the same application the TBAB slurry can be produced at a higher temperature than chilled water. Furthermore, due to its phase change, the TBAB has a larger cooling capacity which can be utilized to reduce the flow rates in the system.

At his moment, the TU Delft has in collaboration with Hollander Techniek installed a small pilot air conditioning system in the sports hall 'De Jachtlust' located in Twello, the Netherlands. The system has a capacity of approximately 3.5 kW. It has a single 300 L storage tank of and it is equipped with sensors to monitor the performance of the system.

During this project an existing model of a secondary air conditioning system is improved and extended taking into account the design parameters of the installation in Twello. In the literature, it is found that the adhesion of the crystals composes the main challenge of these systems. The crystal can be removed by friction with the flow. In the model it is assumed the friction losses are equal to the removal work exerted on the crystal layer. Based on this principle the velocity and the thickness of the crystal layer is determined using experimental data for the required TBAB removal force. The heat transfer and pressure drop correlations are selected using experimental data. The model is validated with water as a secondary refrigerant using the experimental data from the pilot system in Twello.

The simulations predict that using a 36.5 wt % TBAB solution increases the COP from 2.96 to 4.00, while the energy consumption reduces by 24.8 %. This reduction is mainly due to a 30.5 % decrease in the power consumption of the compressor. At the same time, the generation side pump consumes 204 % more electricity due to adhesion of the produced crystals to the heat transfer surface. The performance of the TBAB can still be improved by lowering the initial TBAB fraction to 35.0 wt% or by further optimizing the control strategy for the crystal production.

Acknowledgments

NOMENCLATURE

LATIN

A	area, [m^2]
a	operand, [-]
B	bore, [m]
b	distance between the plates, [m]
Bd	Bond number, [-]
Bo	boiling number, [-]
C	concentration [1/m^3]
Co	convection number, [-]
COP	coefficient of performance, [-]
C_p	specific heat, [J/(kg K)]
D	diffusivity, [m^2/s]
d	diameter, [m]
E	energy, [J]
F	force, [N]
Fr	Fraude number, [-]
f	Darcy friction factor, [-]
G	mass flux, [kg/(m^2/s)]
$\dot{G}$	growth rate, [kg/s]
g	gravity constant, [m/s^2]
H	head, [Pa]
h	enthalpy, [J/(kg K)]
K'	fluid consistency index, [-]
k	mass transfer coefficient, [m/s]
L	length, [m]
l	stroke, [m]
M	molar mass, [kg/kmol]
m	mass, [kg]
$\dot{m}$	mass flow, [kg/s]
N	rotational speed, [rot/s]
Nu	Nusselt number, [-]
n	flow behavior index, [-]
nr	number, [-]
P	power, [W]
p	pressure, [Pa]
Pr	Prandtl number, [-]
$\dot{Q}$	heat flow, [W]
Re	Reynolds number, [-]
RH	relative humidity, [-]
Rp	roughness, [μm]
Sc	Schmidt number, [-]
Sh	Sherwood number, [-]
T	temperature, [K]
t	time, [s]
U	overall heat transfer coefficient, [J/(m^{2}K)]
V	volume, [m^3]
$\dot{V}$	volume, [m^3]
v	volume flow, [m^2/s]

$\dot{W}$	work, [W]
w	mass concentration, [-]
X	vapor fraction, [-]
x	axial position, [-]

GREEK

α	heat transfer coefficient, [W/(m^2 K)]
β	corrugation angle, [-]
$\dot{\gamma}$	shear rate, [1/s]
γ	corrugation aspect ratio, [-]
Δ	difference, [-]
δ	thickness, [m]
ζ	loss coefficient, [-]
η	efficiency, [-]
λ	thermal conductivity, [W/(m K)]
μ	viscosity, [Pa/s]
ρ	density, [kg/m^3]
σ	surface tension, [N/m]
τ	shear stress, [Pa]
Φ	surface enlargement, [-]
ϕ	volume fraction, [-]
ψ	operand, [-]
χ	operand, [-]
ω	mass fraction, [-]

SUPERSCRIPT

n	element number
sat	saturation
t	time step

SUBSCRIPT

0	initial
a	acceleration
app	apparent
amb	ambient
b	bend
c	crystals
$comp$	compressor
cr	critical
$cross$	cross section
d	design
e	equilibrium
ef	effective
$elec$	electric

eq	equivalent		rem	removal
$evap$	evaporating		s	isentropic
i	inner		sat	saturation
in	entering		$stor$	storage tank
ice	ice		$scrap$	scrapping
f	friction		set	settling
fan	fan		sol	solution
fin	fin		sl	slurry
G	vapor		$TBAB$	tetra-n-butyl ammonium bromide
gen	generator		v	virtual
h	hydraulic		vol	volumetric
L	liquid		w	wall
LG	phase change			
$latent$	latent heat			
m	mean			
max	maximum			
$mech$	mechanical			
mod	modified			
o	outer			
opt	optimum			
out	leaving			
p	plate			
pt	port			
$pump$	pump			
r	refrigerant			
ref	reference			

ABBREVIATIONS

ACH	air change per hour
CFCs	chlorofluorocarbons
CHS	clathrate hydrate slurry
COP	coefficient of performance
HCFCs	hydrochlorofluorocarbons
HVAC	heating ventilation and air conditioning
PCM	phase change materials
PTFE	polytetrafluoroethylene
TBAB	tetra-n-butylammonium bromide

DEFINITIONS

TBAB mass concentration of a solution:

$$w_{TBAB} = \frac{m_{TBAB}}{m_{sol}}$$

Solid mass fraction of a slurry:

$$\omega_c = \frac{m_c}{m_{sl}}$$

Solid volume fraction of a slurry:

$$\phi_c = \frac{V_c}{V_{sl}} = \frac{\omega_c/\rho_c}{\omega_c/\rho_c + (1-\omega_c)/\rho_{sol}}$$

CONTENTS

1

INTRODUCTION

Air conditioning systems are used all over the world to control the air temperature and humidity of a confined space by extracting heat from it. At the moment the worldwide demand for air conditioning is rapidly growing. This trend is expected to continue due to the increased welfare in developing countries [13, 18, 28]. Improved living standard in countries like China and India open up new markets with enormous potential for air conditioning technologies. By the 2060s the world wide energy demand for air conditioning is expected to exceed the energy demand for heating [28, 31].

Due to the high demand for air conditioning systems and the high CO_2 emissions associated with air conditioning, there is a need for improving the efficiency of these technologies. However, traditional refrigerants such as CFCs and HCFCs are regulated or phased out by the Montreal and Kyoto protocol due to either their contribution to the depletion of the ozone layer or their global warming potential. In order to limit the use of these harmful refrigerants secondary loop air conditioning systems are increasingly used. These systems make use of a distribution fluid (the secondary refrigerant) as transport medium between the chiller and the coolers. Water is commonly used as a secondary refrigerant in air conditioning system. Usually the water is cooled down in the chiller from 12 to 7 °C while the primary refrigerant evaporates at about 2 °C. Next, the chilled water is used to cool down the air from about 22 to 16 °C. The temperature glide of the water in the chiller and the air cooler limits the overall efficiency of the system. Furthermore, due to the low specific heat of chilled water, the pumps of the secondary refrigerant can account for up to 30 % of the total energy consumption of such a system [71]. Both problems can be solved by using change material (PCM) as a distribution fluid.

1.1. HYDRATE SLURRIES

Hydrate slurries are a group of the PCMs that have been proposed as possible replacement for water as the secondary refrigerant in air conditioning systems. Hydrate slurries are suspensions of crystals (hydrates) in a solution. At room temperature the PCM is a clear solution without any hydrates. If this solution is cooled down to below a certain temperature (referred to as the phase change or equilibrium temperature) hydrates are formed. The hydrates are produced at more or less constant temperature, so the temperature glide in the chiller and the coolers will be much smaller. Furthermore, due to latent heat of the phase change, the cooling capacity of these slurries is much larger than that of water.

One promising hydrate slurry is a solution of tetra-n-butyl ammonium bromide (TBAB) in water. TBAB is a white salt with a good solubility in water. The crystal hydrates can be produced at atmospheric pressure at a temperature ranging from 0-12.5 °C depending on the TBAB concentration. This temperature range nicely fits the desired temperature range for air conditioning applications. Due to its phase change the cooling capacity of the TBAB CHS is about 2-4 times larger than that of chilled water with a temperature glide of 7 °C [75]. Therefore it is sometimes referred to as high density thermal energy carrier [70].

Another advantage is the TBAB solution does not pose significant safety issues. The powder itself can cause irritation, severe eye damage and is toxic when it is swallowed [49]. The TBAB solution on the other hand does not impose these hazards when it is properly integrated in air conditioning systems. Other usefull properties of TBAB include that the solution does not deteriorate after repeated usage and it is even possible to recycle the substance after the system is dismantled [51]. Furthermore, the TBAB solution is nonflammable

and unlike CFCs and HCFCs it hardly contributes to global warming or the depletion of the ozone layer.

1.2. TBAB AIR CONDITIONING SYSTEMS

A schematic overview of a TBAB air conditioning system is included in figure 1.1. The system consists out of primary and a secondary loop. The primary loop uses a conventional refrigerant while the secondary loop makes use of the PCM (in this case the TBAB solution). The primary loop consist out of a conventional air conditioning unit. In this refrigerant cycle heat is extracted in the evaporator (the generator) and released to the environment in the condenser. The TBAB crystals are also produced in the generator. The generator is a heat exchanger in which heat is extracted from the solution while the refrigerant is evaporated. The TBAB solution is pumped from the storage vessel through the generator. In the generator the solution is cooled down to below its crystallization temperature so that TBAB crystals are produced. The result is a suspension of crystal in a TBAB solution. This suspension is usually referred to as a clathrate hydrate slurry or CHS.

The CHS is stored in the storage tank for future usage. If there is a cooling demand the utilization side pump is switched on. Then, the CHS is pumped through the air cooler, melting the crystal while cooling down the air in the room. When the crystal fraction in the storage vessel reduces below a certain set point then the generation side pump is switched on. Otherwise the CHS is replenished during the night when the crystal production is more efficient due to the lower ambient air temperature.
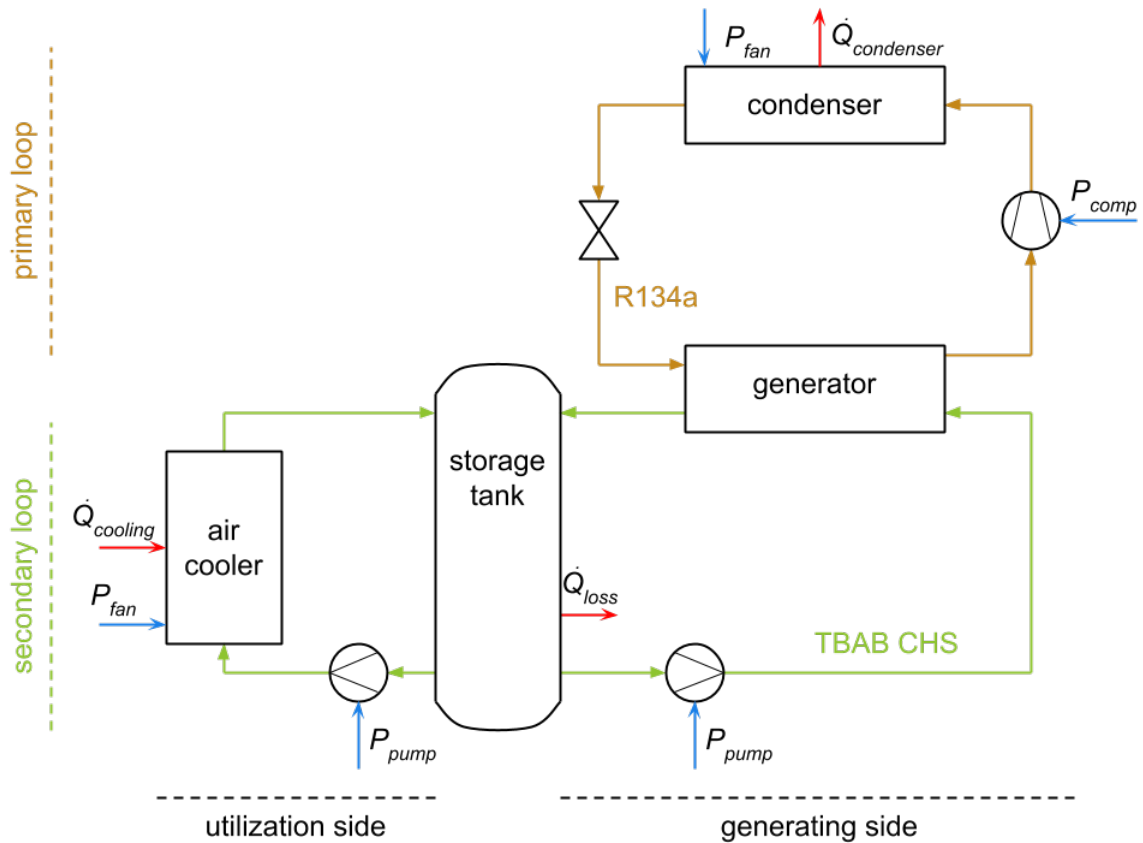
Figure 1.1: A schematic overview of the TBAB air conditioning system as installed in Twello.

The storage of the CHS offers the advantage that the system can also profit from the lower night tariff for the electricity. However, the main advantage of using TBAB is that it will reduce the electricity consumption because:

- The TBAB crystals can be produced at an almost constant temperature (which can be as high as 12.5 °C) while water is usually cooled down from 12 to 7 °C. So the crystals can be produced at higher temperature which means that the evaporation temperature in the condensing unit can be raised.

- Due to the storage the TBAB can be generated during the night when the ambient air temperature is

lower, so the temperature (and pressure) in the condenser can be reduced. This and the previous item will reduce the pressure ratio in the compressor and therefore also reduce the power consumption of the compressor.

- Due to the higher cooling capacity of the TBAB CHS the flow rates in the system can be reduced. This will reduce the pumping power in the utilization side of the system.

REALIZATION OF TBAB SYSTEMS

JFE Engineering Corporation already marketed TBAB air conditioning system under the name Neo White®. This company has already installed several large scale TBAB air conditioning systems in Japan, Southeast Asia and the USA [32]. For all these projects an energy saving of more then 20 % was reported. One of these projects was a 56000 m^2 shopping center for which an energy reduction of 40.17 % was achieved [75].

Besides these large scale installations a number of research installations have already been realized. Douzet et al. constructed a prototype installation but they still faced some challanges with crystal adhesion to the heat exchanger surface [21]. Ma et al. also installed a pilot plant, although they did not achieve a reduction in the energy consumption. They explained the lack of an energy reduction by the low pumping power (due to the short piping in their research installation) [45].

At his moment the TU Delft has in collaboration with Hollander Techniek installed a small air conditioning system in sports hall 'De Jachtlust' located in Twello, the Netherlands. The system has a capacity of approximately 3.5 kW and it is used to cool a single room with a floor area of about 100 m^2. The system has a single storage tank of 300 L and it is equipped with sensors to monitor the performance of the system. The system was taken into operation at 6 September 2016 using water as a secondary refrigerant. The water solution will later on be replaced for a 36.5 wt% TBAB solution.

1.3. OBJECTIVE

The objective of this thesis is to quantify the effect of the application of TBAB hydrate slurries on the energetic performance of secondary loop air conditioning systems. The hypothesis is as follows:

The energy consumption of the secondary loop air conditioning system installed in Twello can significantly be reduced if a TBAB hydrate slurry instead of water is used a secondary refrigerant.

The hypothesis is validated by extending and improving the model made by Zak [74]. New studies and experimental data will be used to find the most suitable correlations to implement in the model. The model will be validated with the experimental data obtained from the pilot system in Twello. Finally the model will be used to compare the performance of the TBAB air conditioning system with the performance of a conventional water system.

1.4. OVERVIEW OF THE REPORT

The report offers a more or less chronological overview of the research. An overview of the subject included in each chapter is presented below:

- Chapter 2: in this chapter an insight in the relevant phenomena occurring in TBAB systems is presented as wells as the most important findings of earlier studies to PCM air conditioning systems.

- Chapter 3: this chapter offers an overview of the correlations that are used to describe and model the properties of the TBAB solution, crystals and CHS.

- Chapter 4: the heat transfer and pressure drop correlations are presented in the model. Where possible the most suitable correlations are selected based on data available in the scientific literature.

- Chapter 5: here the model is discussed. The model is divided into one submodel for each separate component. In this chapter the correlations and methods that are used to model each separate component of the system are presented.

- Chapter 6: the validation of the model with the experimental data can be found in this chapter. It also includes the selection of the most suitable heat transfer and pressure drop correlations based on the experimental data.

- Chapter **??**: the mass flow of the TBAB CHS are optimized in order to reduce the energy consumption of the systems. The method and the optimized mass flows are presented in this chapter.

- Chapter 8: in this chapter the simulation and the control parameters are discussed. Furthermore the result of the simulations is presented in this chapter.

- Chapter 9: in this chapter the result presented in the previous chapter are further analyzed and discussed. The results are also compared with findings from the literature.

- Chapter 10: here the hypothesis is validated and the conclusion of the research is given.

- Chapter 11: finally some recommendations for further research are given. This chapter also includes some suggestions for the continued work on the model and the system in Twello.

2

AN OVERVIEW OF THE RESEARCH RELATED TO TBAB AIR CONDITIONING APPLICATIONS

In this chapter an overview of recent studies related to use of TBAB in air conditioning applications is presented. The studies provide insight in the relevant phenomena occurring in TBAB air conditioning systems. The literature about the properties of TBAB will be discussed separately in chapter 3.

2.1. CRYSTALLIZATION

Tetra-n-butylammonium bromide (TBAB) is a white salt with a high solubility in water at room temperature. However, when a TBAB solution is cooled down two distinctive types of TBAB crystals hydrates can be formed: type A and type B hydrates. The TBAB concentration and the temperature will determine which type of hydrate is formed. Figure 2.1 shows the two different hydrate types. The type A crystals have a columnar shape while the type B crystals are more irregularly shaped. It has been reported that type A crystals are more easy to produce, while the type B have a slightly higher specific heat due to its higher hydration number [53].
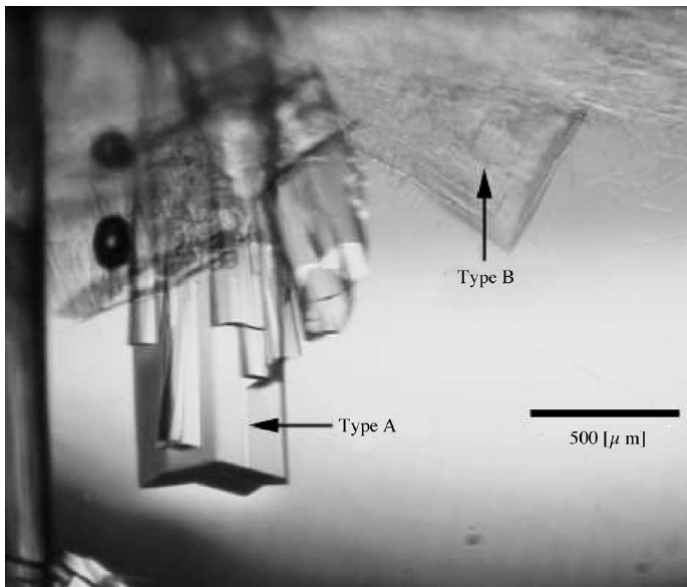

Figure 2.1: TBAB type A and type B crystals hydrates [53].

The crystallization process of TBAB can just as many other crystallization processes be described in three steps [75].

- The solution is cooled down to below the phase change temperature. This supercooling is the driving force behind the crystallization process. Even though the fluid is below its phase change temperature no hydrates are immediately formed.

- The nucleation will begin. Usually the nucleation will start around impurities in the fluid or at the surface walls. Another option is to use seed crystals so the nuclei are already provided.

- The crystals will start to grow. The subcooling remains the driving force for the crystal growth, however a smaller subcooling is required compared to the nucleation process.

2.2. Crystal production within air conditioning systems

One of the main challenges during the production of TBAB crystals is the a crystal layer that will be formed on the surface of the heat exchangers. This crystal layer provide the nuclei for the crystallization process. However, this layer wil also reduce the heat transfer in the heat exchanger and can even from a blockage of the flow passage. Several different TBAB crystal generation methods have been investigated by Shi and Zang [58]. They found that continuous cooling resulted in a two large crystal adhesion to the surface of the heat exchanger. They experimented with using a scrapper to detach the crystals. Unfortunately, the power consumption of the scraper was too large due to the high scrapping forces that are required. They obtained a better result by temporally shutting down the refrigerant cycle when the first crystals appeared. Then, the subcooling was reduced before the crystal production was continued. In this way the subcooling, and therefore the crystal growth, was reduced.

Ma et al. proposed another method to limit the growth of the crystal layer [45]. They designed an air conditioning system in which the TBAB was produced in a coil heat exchanger. Once in a while, when the crystal layer became to thick, they reversed the operation of the refrigerant cycle in order to melt the crystal layer. Then, they continued the crystallization process as before. In this fashion they could produce the crystal at a higher subcooling.

Zhou et al. used a different method to produce crystals. They also used a coil heating exchanger, however they used the friction with the flow to break of the crystals [80]. Meanwhile the subcooling was limited in order to prevent the formation of blockages. The shear force of the flowing fluid was sufficient to obtain an equilibrium between the crystal growth and removal. Zak [74] modeled this process in order to predict the thickness of the produced crystal layer. He assumed a steady state condition so crystal growth rate is the same as removal rate. The work exerted on the crystal layer was found by an energy balance:

$$\dot{V}\Delta p = \dot{W}_f \tag{2.1}$$

The work done by friction was related to the power consumption of scrapped surface heat exchangers. In this model the pressure drop is frictional, so it is a function the friction factor and the thickness of the crystal layer. So the work done by the friction could be expressed as:

$$\dot{W}_{rem} = \dot{W}_f = \dot{V} f \frac{L}{d_i - 2\delta_c} \frac{1}{2} \rho v^2 \tag{2.2}$$

The scrapping force for a TBAB crystal layer has has been investigated by Daitoku and Utaka [14]. The used a setup in which TBAB crystals produced on a vertical brass surface. A scrapped was used to remove the crystal layer. In their research the determined the force required to break of the crystals with this scrapper. They repeated this process and discovered that the scrapping force increased for repeatedly scrapped surfaces. They also discovered that the crystals adhere more strongly to the surface if the TBAB concentration of the solution increased.

2.3. Re-laminarization

The friction of a flowing slurry consists out of two seperate phenomena [46]. The first phenomena is the friction due to the viscosity of the fluid; the second is the mechanical friction caused by the solid particles. For laminar flows the viscous friction dominates. However, the mechanical friction rapidly increases when the flow becomes turbulent. This is because in a laminar flow the solid particles move predominantly in the axial direction. In a turbulent flow the radial component of the velocity is much larger. Usually, the mechanical friction increases with the solid fraction of the slurry. However, the presence of the solid particles in the slurry can also reduce the turbulence of a flow [68]. In this case the mechanical friction of the particles act as a resistance to the radial velocity of the flow. So a turbulent flow might suddenly become laminar when the

solid fraction of the slurry increases. This effect is known as re-laminarization. This phenomena is observed during many experiemnts with TBAB slurries [46, 68].

2.4. STORAGE

Several different storage mechanism have been considered for TBAB storage. These storage mechanism can be divided into two categories; homogeneous and heterogeneous. Both homogeneous and heterogeneous storage have been succesfully applied for TBAB storage [75]. TBAB crystals have a slightly higher density than the solution. So in the case of heterogeneous storage tank the crystals tend to slowly agglomerate and settle at the bottom of the tank. Therefore homogeneous storage tank must be stirred in order to prevent agglomeration and settling of the crystals.

Different storage mechanism have been compared by Shi and Zang [59]. They reported that the use of homogeneous storage tank results in a lower COP compared to heterogeneous storage tanks. In the heterogeneous storage tanks the crystals settle to the bottom so the subcooling at the outlet of the tank is higher. Furthermore, they reported that the TBAB mass concentration at the bottom of heterogeneous tanks is lower (due to its lower temperature) which helps to prevent crystal adhesion.

The storage tank in the system is not stirred, so it is a hetrogenous storage tank. Homogeneous storage tanks are easier to model because a single control volume with averaged properties is sufficient to describe to entire storage tank. Heterogeneous storage tanks require more complex relations in order to describe the gradients in the crystal mass fraction and concentration. Therefore an overview of several storage tank models is presented. Ice storage tanks are also included in this overview because the same physical processes occur as in TBAB storage tanks. Granted, the particles in a water storage tank settle on top instead of at the bottom of the tank. However, non of the models describe the flow pattern in such a detail that this will pose a problem. The equations presented in this section remain valid regardless of the direction of flow of the particles.

MODEL OF TAMASAUSKAS ET AL.

Tamasauskas et al. [63] studied the thermal performance of a solar assisted heat pump with a thermal storage. For this application they developed a model of a thermal ice storage tank. Their modeling approach included the following assumptions:

- The crystals and the fluid separate in two distinctive layers.

- The crystal layer has the same thickness everywhere.

- The temperature of the ice and the fluid does not vary within the control volume.

- The crystal layer always is at the phase equilibrium temperature so no subcooling occurs.

- The density and porosity of the crystals is constant throughout the crystal layer.

They divided the storage tank into a control volume for the crystal layer and a control volume for the fluid layer. A schematic overview of the modeling approach is shown in figure 2.2. For both control volumes an energy balance is made. The energy balance of the crystal layer can be expressed as:

$$-\Delta h_{latent}\frac{dm_{ice}}{dt} = \dot{m}_{in}C_p(T_{in}-T_{ice}) - \Delta h_{latent}\dot{G} + \alpha A(T_{amb}-T_{ice}) + \alpha A_{cross}(T_{sol}-T_{ice}) \qquad (2.3)$$

The mass flows in these equations represent only the fluid. The amount of crystals that enters the tank is represented by the term $\dot{G}$ while the amount of liquid entering the tank is represented by $\dot{m}$. The energy balance for the water layer can be expressed as:

$$C_p\frac{dm_{sol}T_{sol}}{dt} = \dot{m}_{in}C_p(T_{ice}-T_{sol}) + UA(T_{sol}-T_{ice}) + \alpha A_{cross}(T_{ice}-T_{sol}) \qquad (2.4)$$

The predicted temperature and crystal fraction are in good agreement with the experimental data. However they found some discrepancies between the predicted and measured crystal fraction during the charging process. This might be due to the placement of the sensors in combination with stratification in the fluid. This might have resulted in an overestimation of the ice fraction during the measurements.

The assumption that the storage tank can be divided into two separate layers may limit the accuracy in a model for TBAB storage tanks. Simulations and experiments performed by Douzet et al. [21] suggest that
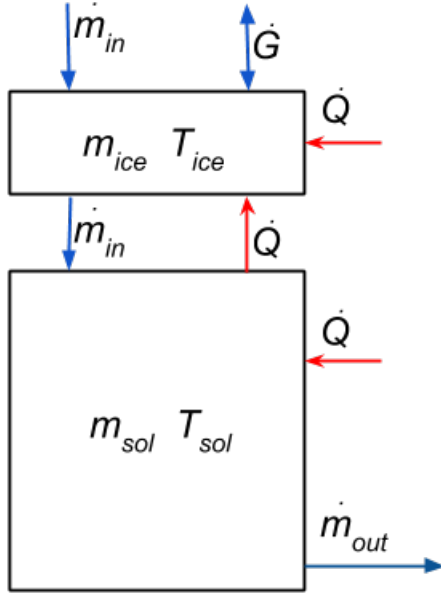
Figure 2.2: An overview of the model of the ice storage tank of Tamasauskas et al. [63].

the settling velocity of TBAB crystals is very slow which would result in a much larger boundary between the crystals and the fluid. Therefore the thermal interaction between the TBAB crystals might be underestimated by the model.

MODEL OF FLICK ET AL.

Another model for an ice slurry storage tank has been developed by Flick et al. [24]. They modeled the storage tank as a cylinder and reduced the problem to an 1D geometry. The following assumptions are used:

- The tank is 1D so the properties of the slurry are constant for a given cross section. The properties do depend on their vertical position in the tank.

- The total volume of the tank is constant so the change in volume as a result of crystallization process is neglected.

- The tank is always and everywhere at the equilibrium phase change temperature.

- The entering mass flows are also at the phase change temperature.

- The agglomeration of crystals is neglected.

The mean velocity of the slurry in the tank at a given height can be calculated with the flow rates entering and leaving the tank. This velocity can be described as the sum of the solution and crystal velocity.

$$v = (1 - \phi_c) v_{sol} + \phi_c v_c \tag{2.5}$$

The settling velocity of the ice crystals can be described by a modified Stokes' law. It assumes spherical crystals and a damping function that increases with increasing ice fractions.

$$v_c = v_{sol} + v_{set} = v_{sol} + g \frac{(\rho_{sol} - \rho_c) d_c^2}{18 \mu_{sol}} f(\phi_c) \tag{2.6}$$

The material balance of ice crystals can be expressed by:

$$\frac{\partial C}{\partial t} + \frac{\partial}{\partial x} \left(C v_c - D_{eq,c} \frac{\partial C}{\partial x} \right) = 0 \tag{2.7}$$

The volume fraction of the crystals is calculated with the energy balance.

$$-\Delta h_{latent}\frac{\partial}{\partial t}(A_{cross}\rho_c\phi_c) + \frac{\partial}{\partial x}\left(A_{cross}\left(\rho_c\Delta h_{latent}\left(D_{eq,c}\frac{\partial\phi_c}{\partial x} - \phi_c v_c\right) - \lambda_{sl}\frac{\partial T}{\partial x}\right)\right)$$
$$= \alpha\pi d(T_{amb} - T) \quad (2.8)$$

Finally the mass fraction of the crystals in the solution can be calculated using a mass balance.

$$\frac{\partial}{\partial t}(A_{cross}\rho_{sol} - (1-\phi_c)w) + \frac{\partial}{\partial x}\left(A_{cross}\rho_{sol}\left((1-\phi_c)wv_{sol} - (1-\phi_c)D_{sol}\frac{\partial w}{\partial x}\right)\right) = 0 \quad (2.9)$$

The equations are solved in the same order as they are presented. The calculated concentration and mass fractions are used to recalculate the mean equivalent diameter of the crystals used in equation 2.5:

$$\phi_c = C\frac{\pi d_c^3}{6} \quad (2.10)$$

Douzet et al. [21] modified and implemented this model to describe a TBAB storage tank. They used the additional assumption that only one specific type (in this case type A) hydrates are formed. The model was validated for a TBAB air conditioning system. The error in the estimated mass fraction was about 20 %. This is probably partly due to the entering mass flows which were not always at crystallization temperature. The additional cooling of these mass flows to the phase change temperature is neglected by the model.

2.5. CONCLUSION

In the literature several phenomena occurring in TBAB systems already have been investigated. TBAB can from two distinct hydrates which are produced under different conditions. The crystallization process of TBAB can just like any other crystallization process described in three steps, subcooling, nucleation and growth.

The crystal production has also been investigated. One of the major problems is that during the crystallization process crystal adhere to the surface of the heat exchanger. These crystals limit the heat flow and can obstruct the flow. The crystal growth could be limited by the shear rate of the fluid. This process has been modeled by [74] although this model could be further improved.

TBAB storage tanks can be divided in two categories: homogeneous and heterogeneous storage tanks. Two distinct models for heterogeneous storage tank are presented but neither model accurately describes all the relevant phenomena that occur in the actual system (the superheated flow into the tank and the settling of crystals). The model of Flick et al. [24] is much more elaborate however it does describe most of the relevent phenomena wheras the model of Tamasauskas et al. [63] has little added value compared to a lumped storage model. However, if the model of Flick et al. is used then it should be modified in order to also be able to describe the presence of a superheated solution.

<div align="right">

3

</div>

PROPERTIES OF TBAB

The properties of water, air and R134a are already well known. For this model the properties of these fluids are obtained from Fluidprop [12]. However not all the properties of every fluid are included in the Fluidprop library. For example certain properties of R134a, including the viscosity and the thermal conductivity, are not included in Fluidprop. However, these properties can be found in the Refprop library [38]. The data obtained from Refprop is used to construct first or second order polynomials in order to describe these properties. The properties of humid air can be obtained from the properties of air and water. Appendix A provides an overview of the relations used to determine the enthalpy of humid air.

The properties of TBAB are still the subject of research and are therefore not included in the library of Fluidprop and Refprop. Therefore, correlations from the literature will be used. In this chapter an overview of the available correlations of the properties of TBAB crystals, solutions and CHS is given. The mass concentration of TBAB in the hydrates is given by:

$$w_{TBAB,c} = \frac{M_{TBAB}}{M_{TBAB} + nr_{hyd} \times M_{H_2O}}$$

(3.1)

In this equation is nr_{hyd} the hydration number. As mentioned earlier TBAB can form two distinctive hydrates type A and type B hydrates. The hydration number of the hydrates is 28 and 36 for respectively type A and type B crystals. Based on the hydration number the mass fraction TBAB in the hydrate can be determined. For the type A hydrate it is equal to 0.4077.

The installation in Twello is designed for type A TBAB CHS because the type A crystals can be produced at a higher temperature. The system in Twello has an initial mass concentration of 36.5 wt% in order to maximize the crystallization temperature. The subcooling in the system is limited so only type A hydrates are formed. Therefore only models and relations for type A crystals are discussed in this chapter.

3.1. PHASE EQUILIBRIUM TEMPERATURE

The phase equilibrium temperature of TBAB is already thoroughly investigated. Depending on the temperature and the TBAB concentration either type A or type B crystals are formed. This is described by the graph in figure 3.1. The graph also includes the data points of a number of studies. Kumano et al. [35] derived a cubic polynomial to describe the crystallization temperature based on their measurements. During the experiments the initial concentration is varied from 10 to 30 wt% and as a result the polynomial is not that accurate for high mass concentrations. Furthermore, the correlation that they reported for type B crystals is incorrect.

$$\text{Type A: } T_e = 275.05 + 113.5 w_{TBAB} - 3.18 \times 10^2 w_{TBAB}^2$$

(3.2)

$$\text{Type B: } T_e = 266.64 + 108 w_{TBAB} - 1.62 \times 10^2 w_{TBAB}^2$$

(3.3)

A better correlations was derived by Zak [74]. He derived a polynomial based on the measurements found in the literature. This relation is in good agreement with the experimental data as shown in figure 3.1.

$$T_e = 267.98 + 94.91 w_{TBAB} - 1.27 \times 10^2 w_{TBAB}^2$$
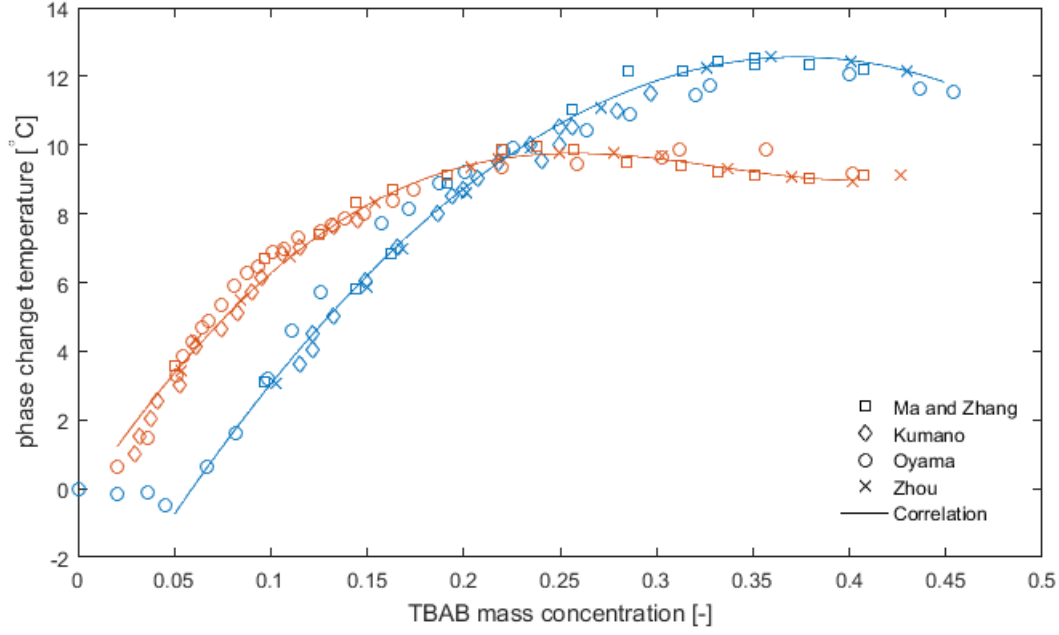
(3.4)

Figure 3.1: The crystallization temperature of the type A (blue) and type B (red) hydrates [35, 46, 53, 80]. The measurements are compared to equation 3.4 and equation 3.5.

In a similar way the experimental data can also be used to obtain a better correlation for the equilibrium temperature of type B crystals. In this way the following correlation is obtained:

$$T_e = 272.7445 + 83.36\,w_{TBAB} - 150.3\,w_{TBAB}^2 - 221.6\,w_{TBAB}^3 + 557.4\,w_{TBAB}^4 \tag{3.5}$$

3.2. DENSITY

The density of the hydrates is also thoroughly investigated. A summary of the result of some studies is shown in table 3.1. All the studies except for the study of Darbouret et al.[16] agree on the density of the type B crystals. Therefore the study of Darbouret is considered to be less reliable. Most of the studies seem to agree on a crystal density of about 1080 kg m^3 so this value will be used.

Table 3.1: The density of TBAB hydrates

Hydrate	Ma and Zhang [42]	Darbouret et al. [16]	Ogoshi and Takao. [52]	Ogoshi et al. [51]
Type A	1080	1082	1030	1086
Type B	1030	1067	1030	1030

The density of the solution has been measured by Ogashi and Takao [52] and Zhang et al. [78]. It is mainly dependent on the temperature and the TBAB mass concentration. This dependence could be described by a lineair correlation [60]:

$$\rho_{sol} = 1003.706 - 0.3959(T - 273.15) + 102.883\,w_{TBAB}; \tag{3.6}$$

Zak [74] proposed a different correlation based on the same measurements:

$$\rho_{sol} = 1036.8 + 13.7C - 0.5357(T - 273.15) - 0.2998C(T - 273.15) \tag{3.7}$$

With:

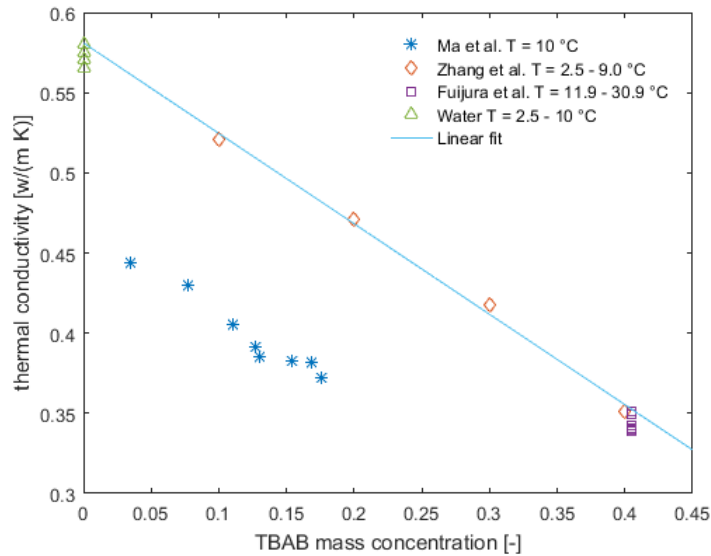$$C = \frac{w_{TBAB} - 0.30}{0.406 - 0.30} \tag{3.8}$$

Figure 3.2: Experimental data on the thermal conductivity of the TBAB solution at different mass fraction and temperatures [26, 46, 77].

Both correlations show a good agreement with the empirical data. The correlations of Zak however is slightly more complex without providing a better accuracy. Therefore, equation 3.6 will be used. The density of the slurry can be approximated using the definition of the volume fraction.

$$\rho_{sl} = \rho_c \phi_c + \rho_{sol}(1 - \phi_c) \tag{3.9}$$

3.3. THERMAL CONDUCTIVITY

The thermal conductivity of TBAB crystals was investigated by Fujiura et al. [26]. They used an initial mass concentration of 40.52 wt% and the supercooling was limited in order to ensure that only type A hydrates were formed. A transient hot wire apparatus was used for to measure the thermal conductivity for a range of temperatures. Their measurements showed that the temperature has a small influence on the thermal conductivity. This could be described by the following empirical relation:

$$\lambda_c(T) = 0.379 + 0.00020 \times (285 - T) \tag{3.10}$$

In another experiment a conductivity of 0.42 W/(m K) was reported at an unspecified temperature [77]. Li et al. also measured an almost linear temperature dependence around the phase equilibrium temperature [39]. They found a sharp increase in the conductivity at temperatures below the 265 K which was not observed in the other studies. However, such low temperatures are not expected to be encountered in the system and therefore the relation of Fujiura et al. will provide a reasonable result.

The thermal conductivity of the solution is experimentally investigated by Ma et al. [46]. They prepared several solutions with a different TBAB concentration and a temperature of 10 °C. The conductivity of each solution was measured using a hot wire. Their result could be fitted to a linear correlation [60]:

$$\lambda_{sol} = 0.581 - 0.564 \, w_{TBAB} \tag{3.11}$$

Other measurements were performed by Fujiura et al. [26]. They prepared a solution of 40.52 wt% TBAB and measured the conductivity while they lowered the temperature. Zhang et al. [77] investigated the conductivity at the phase change temperature for their research to the properties of TBAB CHS. The results of these studies are compared in figure 3.2. Notice that the results are obtained for different temperatures. The experimental data indicates that the thermal conductivity is much more dependent on the TBAB concentration than on the temperature. Therefore, the temperature dependence can be neglected in the correlation. The experiments performed by Zhang et al. are in agreement with the findings of Fujiura et al. and the thermal conductivity of the solution seems to approach the thermal conductivity of water when the TBAB concentration goes to zero. This is not the case with the results of Ma et al. so these measurements cannot be correct. Therefore,

equation 3.11 will be used to predict the thermal conductivity of the solution. The thermal conductivity of the slurry can be expressed with the help of a Maxwell relation [46]:

$$\lambda_{sl} = \lambda_{sol} \left(\frac{2\lambda_{sol} + \lambda_c + 2\phi_c(\lambda_c - \lambda_{sol})}{2\lambda_{sol} + \lambda_c - \phi_c(\lambda_c - \lambda_{sol})} \right) \tag{3.12}$$

3.4. SPECIFIC HEAT

One study found that the specific heat of type A crystals is 2.22×10^3 J/(kg K) [52] at unspecified conditions. Oyama et al. performed more specific measurements of the specific heat of the crystals [53]. They produced separately type A and type B crystals and measured the specific heat of the crystals at different temperatures with a differential scanning calorimeter. Their results for the type A hydrates can be fitted to the following polynomial:

$$C_{p,c} = -117293 + 1267.5T - 4.554T^2 + 5.5556 \times 10^{-3} T^3 \tag{3.13}$$

The specifc heat of the solution has been measured by Zhang et al. [77]. They concluded that the specific heat of the solution is 4.03×10^3 J/(kg K) at unspecified conditions. More specific measurements were performed by Asaoka et al. [5]. They prepared solutions with several different mass concentrations. They reported a negative dependence of the mass concentration on the specific heat.Fujiura et al. Their results can be fitted to a second order polynomial:

$$C_{p,sol} = 4234 - 568 w_{TBAB} - 1016 w_{TBAB}^2 \tag{3.14}$$

The specific heat of a slurry can be approximated by a mass based average of the specific heat:

$$C_{p,sl} = \omega_c C_{p,c} + (1 - \omega_c) C_{p,sol} \tag{3.15}$$

3.5. VISCOSITY

The viscosity of a fluid is defined as the shear stress divided by the shear rate:

$$\mu_{app} = \frac{\tau}{\dot{\gamma}} \tag{3.16}$$

For Newtonian fluid the shear stress is linearly dependent on the shear rate, so in other words the viscosity of the fluid is not dependent on the shear stress or the shear rate. This is not the case for non-Newtonian fluids. The viscosity of this type of fluids is dependent on the shear rate and the shear stress. Therefore the viscosity of non-Newtoninan fluid is not constant anymore. The viscosity of these fluids can be expressed by an apparent viscosity: the viscosity of the fluid for a given shear rate. So the apparent viscosity only corresponds to a single point of the viscosity curve.

The viscosity of TBAB solution has been meausred by Kumano et al. [35]. They measured the viscosity of solutions with a TBAB mass concentrations ranging between the 2.5 and 25 wt% at equilibirum temperature. They derived the following equation for the viscosity at phase equilibrium temperature:

$$\mu_{sol} = \rho_{sol} \left(3.035 \times 10^{-6} - 1.539 \times 10^{-7}(T_e - 273.15) + 2.73 \times 10^{-9}(T_e - 273.15)^2 \right) \tag{3.17}$$

Zhang et al.[76] also measured the viscosity of TBAB solutions at different temperatures and TBAB solutions. They reported that the solution is a Newtonian fluid and that viscosity of the solution could be described by the Vogel-Tamman-Fulche model. This model uses the fitting parameters A, B, C and D which are respectively 0.000298, 87.578, 286.510 and -47.942 for this solution.

$$\mu_{sol} = A e^{\left(\frac{B + C w_{TBAB}}{T - 273.15 - D} \right)} \tag{3.18}$$

The two models are compared in figure 3.3. The viscosity at the phase equilibrium temperature is represented by the lines while the markers correspond to the viscosity at higher temperatures. The models deviate more from each other at high TBAB concentrations; this can be explained by the limited range of mass concentrations at which measurements were done. The Vogel-Tamman-Fulche model also provides a correlation of the viscosity above the phase equilibrium temperature and is therefore the most suitable model.
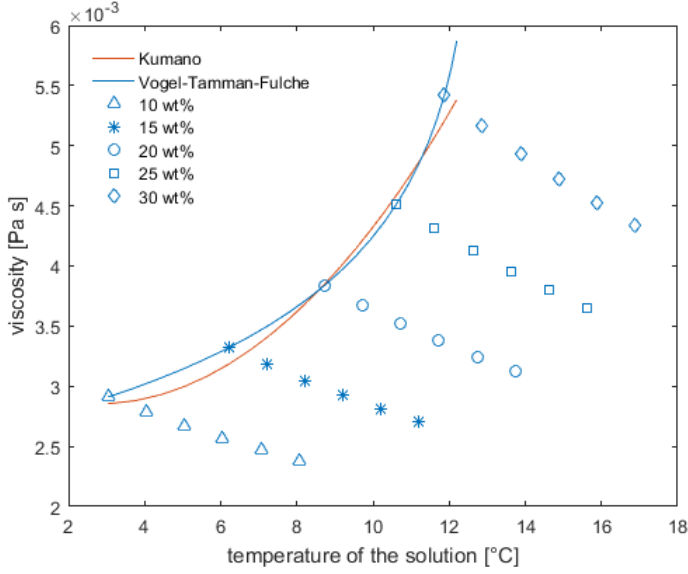
Figure 3.3: The viscosity of the solution. The lines represent the viscosity at phase equilibrium temperature and the markers the viscosity at higher temperatures.

The viscosity of the TBAB slurry can be described by a number of different empirical and theoretical models. Thomas [64] derived an empirical relation which relates the viscosity of a solution to the viscosity of the same solution with spherical particles in it:

$$\mu_{sl} = \mu_{sol}\left(1 + 2.5\phi_c + 10.05\phi_c^2 + 0.000273e^{16.6\phi_c}\right) \tag{3.19}$$

Darbouret et al. [17] proposed to use the Graham Steele Bird model for TBAB CHS. This model defines a volume fraction V_0 which represents the amount of liquid that is trapped by the hydrate clusters:

$$V_0 = 1 + \left(\frac{1}{\phi_{max}} - 1\right)\left[1 - \left(\frac{\phi_{max}-\phi_c}{\phi_{max}}\right)^2\right]^{\frac{1}{2}} \tag{3.20}$$

This volume fraction and the volume fraction of the crystals are used to estimate the viscosity of the solution:

$$\mu_{sl} = \mu_{sol}(1 - V_0\phi_c)^{-2.5} \tag{3.21}$$

The maximum packing fraction ϕ_{max} depends on the shape of the crystals that are formed. Spherical particles have a maximum packing fraction of 0.74. In that case the model is in good agreement with equation 3.19. Darbouret et al. also carried out experiments with TBAB CHS and they found a maximum packing fraction of 0.65 and 0.60 for respectively type A and type B TBAB CHS. Zhang et al. [76] also measured the viscosity of TBAB CHS. They observed a non Newtonian behavior for the CHS. They reported that the largest deviation from Newtonian behavior occurs at low shear stresses. Nevertheless they found that Eilers model provides a reasonable approximation of the viscosity of of type A CHS.

$$\mu_{sl} = \mu_{sol}\left(1 + \frac{0.5[\mu]\phi_c}{1 - \phi/\phi_{max}}\right)^2 \tag{3.22}$$

They proposed value of 2.5 for the intrinsic viscosity $[\mu]$ and a value of 0.74 for the maximum packing fraction. However these values were believed to be dependent on the shear stress so they could be used to fit the model to the measurements. A comparison between the models is shown in fig 3.4. The measured apparent viscosity at a given shear rate are also included in the graph. The figure shows that the Graham Steele Bird model provides the most accurate description of the viscosity of the CHS. Furthermore this model has the best theoretical foundation. The poor performance of Eilers model is probably due to the fact that the intrinsic viscosity and the maximum packing fraction are not fitted to these measurements. The experimental data showed the shear thinning in the fluid; the viscosity of the solution increases more for decreasing shear rates. This behavior is not described by any of the models however the effects of shear thinning is the most prevalent
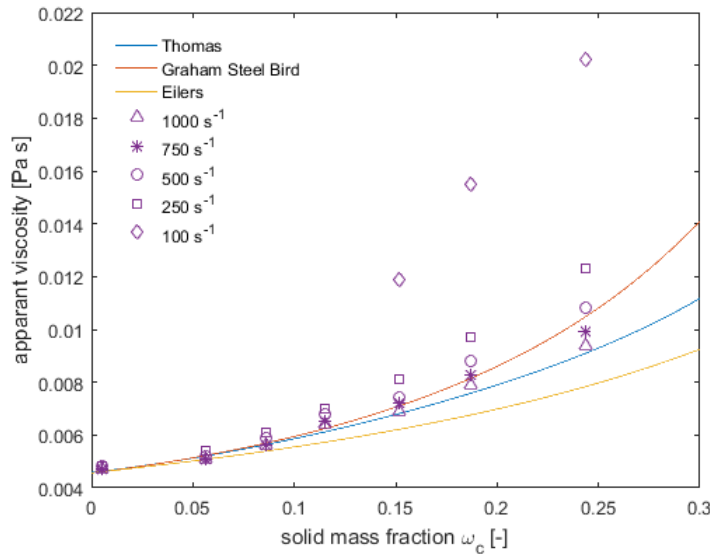
Figure 3.4: The viscosity models compared to the experimental data of Zhang et al. [76].

at low shear rates which are less likely to be encountered during the normal operation of the actual system. The influence of the shear rate on the apparent viscosity is much smaller at higher shear rates $(250 - 1000 s^{-1})$ so for this range the Newtonian model is not sufficiently accurate.

The shear rate is as shown in equation 3.16 dependent on the velocity gradient in the flow. For turbulent flow large velocity gradients and shear rates are expected. However the flow in the system might not always be turbulent; the flow rates are reduced due to the higher cooling capacity of the fluid and at high solid fractions re-laminarization may occur. So it is impossible to be sure that such low shear rates are not encountered in the system. Therefore, the model will also make use of the modified Reynolds number. This model is used to describe the Reynolds number of a non-Newtonian power law fluid. This model is further discussed in section 4.1.

3.6. ENTHALPY

Several different methods have been applied in order to measure the latent heat of TBAB. Oyama et al. first produced the crystals, next they isolated the crystals and stabilized the crystals using liquid nitrogen. Finally the latent heat of the crystals was measured using a differential scanning calorimetry meter [53]. Asaoka et al. prepared a solution in which the TBAB hydrates were added. They found the latent heat by measuring the temperature of the solution during the melting process [5]. An overview of these and other studies is shown in tabel 3.2. The result of Asaoka et al. is about 10% larger then the findings in the other studies. The validity

Table 3.2: The latent heat of TBAB

Hydrate	Oyama et al. [53] [kJ/kg]	Ogoshi and Takao. [52] [kJ/kg]	Asaoka et al. [5] [kJ/kg]
Type A	193.18 ± 8.52	193	210 ± 10
Type B	199.59 ± 5.28	205	224 ± 15

of the measurement of Oyama et al. is supported by the results of Ogoshi and Takao and will therefore be used.

The enthalpy of the solution can be expressed using the specific heat of the solution. The state at which the reference enthalpy is determined can be chosen arbitrarily:

$$h_{sol} = C_{p,sol} T \qquad (3.23)$$

The enthalpy of the slurry can be defined using the latent heat of the crystals [43].

$$h_{sl} = -\omega_c \Delta h_{latent} + \left(C_{p,sl} T \right) \qquad (3.24)$$

For this report the reference state is defined as a temperature of 20 ° and atmospheric pressure.

3.7. CONCLUSION

The properties of TBAB can be described by a number of different correlations obtained from the literature. A summary of the most suitable correlations is shown in table 3.3. These correlations are also used to construct an enthalpy diagram as shown in figure 3.5. In this diagram the enthalpy of type A CHS is plotted against the initial mass concentration. The black lines represent the transition between the superheated liquid, the CHS and the freezing point of the water. For the graph it is assumed to the hydrate slurry is at phase equilibrium temperature as long as the volume fraction is smaller than the maximum volume fraction of 0.65. The diagram also does not include the properties of the type B hydrates. This means that certain areas in the diagram (especially those of the CHS with an initial TBAB concentration of less than 20 wt%) will most likely never be reached.

Table 3.3: Summary of the properties of TBAB

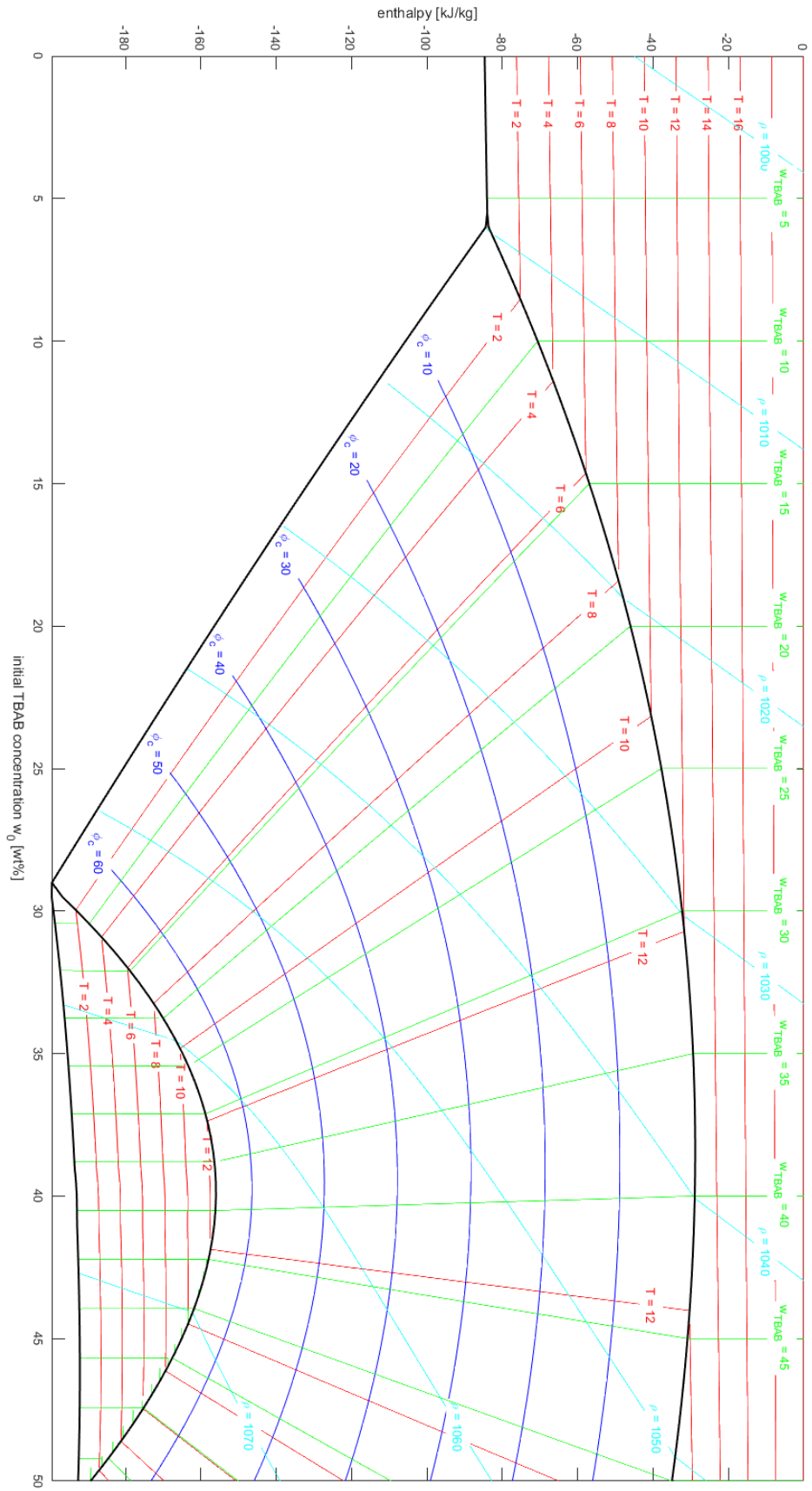|	Solution	Slurry	Hydrate (type A)
Density	equation 3.6	equation 3.9	1080 kg/m^3
Thermal conductivity	equation 3.11	equation 3.12	equation 3.10
Specific heat	equation 3.14	equation 3.15	equation 3.13
Viscosity	equation 3.18	equation 3.21	
Enthalpy	equation 3.23	equation 3.24	

Figure 3.5: Enthalpy as function of the initial TBAB mass concentration for type A TBAB CHS.

4

HEAT TRANSFER AND PRESSURE DROP CORRELATIONS

In this chapter an overview of heat transfer and pressure drop correlations for TBAB CHS is presented. Many of the correlations which are specifically obtained for TBAB CHS make use of the modified Reynolds number. The first section will discuss the relations and the properties of the modified Reynolds number. Next the different relevant correlations for type a TBAB CHS are discussed and the most suitable correlations for the model are selected. In the future these correlations should be further validated using the experimental data of the pilot plant. Finally the correlations for evaporation in plate heat exchangers are presented. These correlations are also relevant for the water system and are validated with experimental data as described in chapter 6.

4.1. MODIFIED REYNOLDS NUMBER

The modified Reynolds number is developed to describe the non-Newtonian behavior of power law fluids. As explained in section 3.5 the TBAB CHS is a non-Newtonian fluid, however the non-Newtonian behavior is neglected in the correlations for the viscosity of the slurry. Ma et al. [46] found that non-Newtonian behavior of TBAB CHS could be described by a power law fluid. Power law fluids are fluids in which the shear stress can be expressed as:

$$\tau = K'\dot{\gamma}^n \tag{4.1}$$

In this relation K' stands for the fluid consistency index and n is the flow behavior index. These indexes can be used to calculate the modified Reynolds number:

$$Re_{mod} = \frac{d^n v^{2-n} \rho}{K' 8^{n-1}} \tag{4.2}$$

The modified Reynols number was first introduced by Metzner and Reed [47] and it can be used for all kind of non-Newtonian fluids. The fluid consistency index and the flow behavior index are fluid properties which should be experimentally determined by measuring the pressure drop in smooth tubes. For laminar flow the friction factor can be directly related to the modified Reynolds number using Poiseuilles law.

$$f = \frac{64}{Re_{mod}} \tag{4.3}$$

For turbulent flow other relations should be used. For example Ma et al. determined the modified Reynolds number using the following semi-empirical relation [46]:

$$\frac{1}{\sqrt{f}} = \frac{2.0}{n^{0.75}} ln \left(Re_{mod}(0.25f)^{\frac{2-n}{n}} \right) - \frac{0.2}{n^{1.2}} \tag{4.4}$$

THE FLUID CONSISTENCY INDEX AND FLUID BEHAVIOR INDEX

Zhang et al. [76] performed a comprehensive study of the properties of n and K'. They prepared slurries of type A TBAB CHS with solid fraction ranging from 0 to 25 wt%. They used a setup in order to measure the pressure

drop of the slurry flowing through a long horizontal tube. They made use of equation 4.3 and 4.4 to relate the pressure drop to the indexes. Their result is shown in figure 4.1. They compared their findings with the result of Zhang and Ye [79] and Kumano et al. [35]. They concluded that the difference between the measurements was reasonable and that the deviations could be attributed to different measuring methods. Furthermore the shape and the size of the crystals can contribute to the difference. The measurements of Zhang et al. have been performed for an initial TBAB concentration of 20 and 25 wt%. They concluded however that theTBAB concentration has almost no influence on these indexes. Measurements of Ma et al. [46] on type B TBAB CHS indicated that the diameter of the tube can have influence on the index. This was attributed to the enhanced interactions between the particles for a small tube diameter. However this effect was not observed for type A CHS. The measurements of Zhang et al. are used to obtain a correlation for the indexes as shown in figure 4.1. In this correlation the flow behavior index is correlated as:

$$n = 1 - 0.7982\omega_c \tag{4.5}$$

And the fluid consistency index can be expressed as:

$$K' = 0.004652e^{8.101\omega_c} \tag{4.6}$$
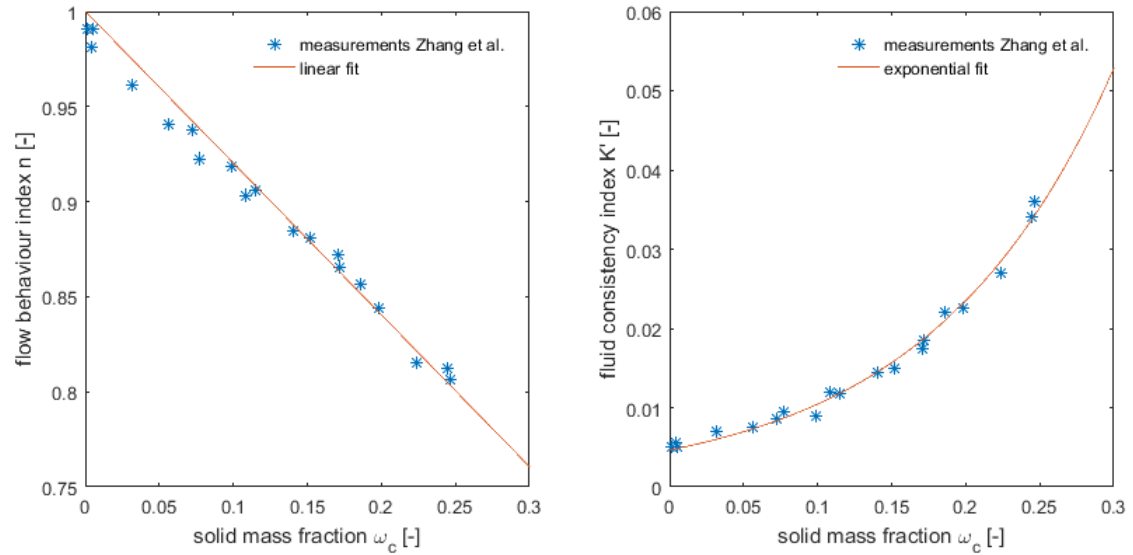

Figure 4.1: The flow consistency and the flow behavior index of type A TBAB CHS [76].

OTHER MODELS
Another study related to the modified Reynolds number was carried out by Xiao et al. [71]. They used the power law model for fluids to rewrite the modified Reynolds number as:

$$Re_{mod} = \frac{\rho v d_h}{\mu_{app}[(3n+1)/(4n)]^n(8v/d_h)^{n-1}} \tag{4.7}$$

They also conducted measurements to determine the flow behavior index n and the apparent viscosity. The pressure drop was measured over a 2 meter long tube with an internal diameter of 21 mm. The volume fraction of the crystals was varied between 0 and 20 wt%. They observed the following relation for the flow behavior index:

$$n = -2.7\phi + 1 \tag{4.8}$$

They concluded that the apparent viscosity depended on the initial TBAB concentration. Their result could be described by the following equations:

$$\mu_{app} = 0.8\phi_c^2 + 0.02\phi_c + 0.0036 \qquad \text{for} w_{TBAB,0} = 0.22 \tag{4.9}$$

$$\mu_{app} = 0.7\phi_c^2 + 0.07\phi_c + 0.0112 \qquad \text{for} w_{TBAB,0} = 0.30 \tag{4.10}$$

The modified Reynolds number was also studied by Wenji et al. [69]. These authors defined the modified Reynolds number as:

$$Re_{mod} = \frac{d\rho v}{\mu_{ef}} \tag{4.11}$$

They assumed that the TBAB CHS could be described as a Bingham fluid and used the Bingham fluid model to get to the following expression:

$$\mu_{ef} = \frac{\tau_w}{8v/d} = \frac{\Delta p/4L}{8v/d} \tag{4.12}$$

They carried out measurements to determine the relation between the wall shear stress and the factor $8v/d$. They produced type A TBAB CHS with crystal mass fractions ranging from 0 up to 25 wt%. The pressure drop was measured while these fluids flowed through a tube with velocity ranging from 0.2 to 1.7 m/s. The results of their experiments are shown in figure 4.2.
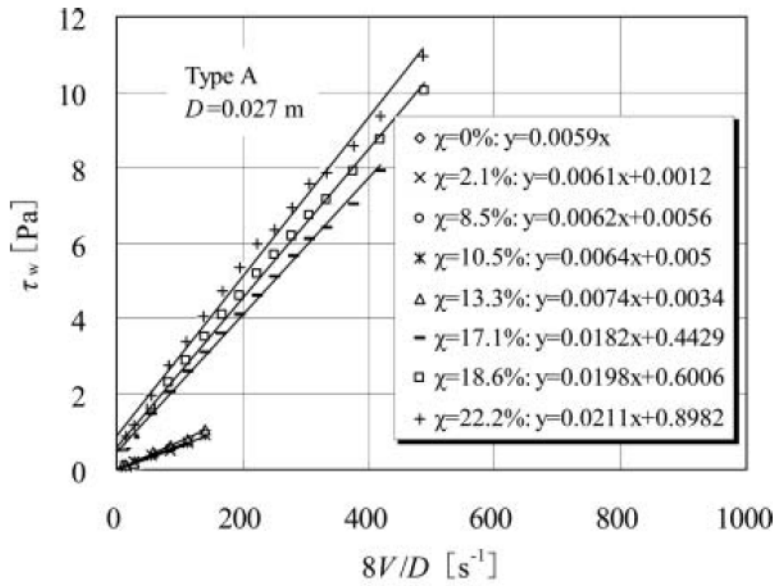

Figure 4.2: The result of the experiments performed by Wenji et al. [69].

Comparison

The modified Reynolds number is calculated according tho the method described by the different studies. A tube diameter of 10 mm and a velocity of 1 m/s is used for the comparison. The result for two different initial TBAB concentrations is shown in figure 4.3. The graphs clearly show that the results obtained by Xiao et al. [71] are not correct. The Reynolds number should decrease for higher solid fractions and this is supported by the observed re-laminarization of the CHS. This can only occur if the Reynolds number decreases with the solid mass fraction.

The graphs also show that there is only a very small difference between the modified Reynolds number and the actual Reynolds number at low solid fractions. This is because the only difference between these Reynolds numbers is that the modified Reynolds number also accounts for the effects of the non-Newtonian behavior of the fluid. The non-Newtonian behavior increases with the solid fractions and this is also observed in the graph. The aqueous solution has a Newtonian behavior [76] so the actual and the modified Reynolds number should be the same for a solid mass fraction of zero. This is the case for an initial mass TBAB concentration of 22 wt% but not for an initial TBAB concentration of 30 wt%. The flow behavior index is always 1 for a Newtonian fluid so the fluid consistency index should be dependent on the initial TBAB concentration. This is supported by the findings of Xiao et al. [71] in which they concluded that the apparent viscosity was function of the initial TBAB concentration. Based on these observation a correction factor can be developed to account for the influence of the initial TBAB concentration on the fluid consistency index:

$$K' = \left[44.11 w_{TBAB,0}^3 - 18.48 w_{TBAB,0}^2 + 4.516 w_{TBAB,0} + 0.314 \right] 0.004652 e^{8.101\omega_c} \tag{4.13}$$
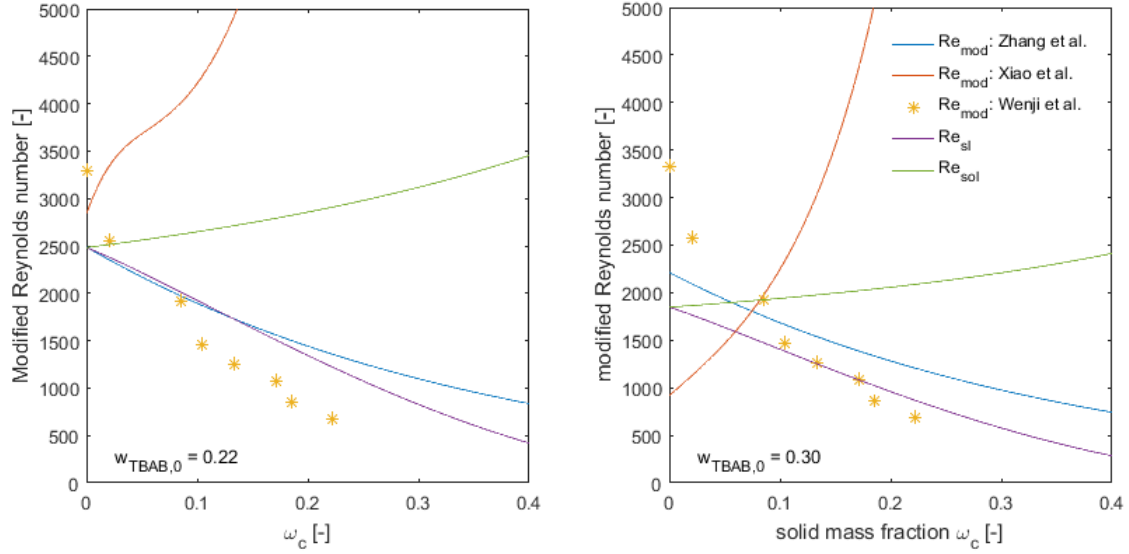
Figure 4.3: Comparison of the different modified Reynolds number models compared with the Reynolds number of the solution and the slurry.

4.2. The pressure drop of TBAB flowing in tubes

The pressure drop of TBAB CHS has already been the subject of several studies. All the studies mentioned in section 4.1 measured the pressure drop in smooth tubes in order to determine an expression for the modified Reynolds numbers. Based on their experimental data they proposed several different friction factor correlations for type A CHS. An overview of these correlations is shown in table 4.1. All the authors agree on using the modified Reynolds number and Poiseuilles law for the laminar flow regime. For the turbulent flow regime several different empirical correlations were proposed. The transition between laminar and turbulent flow occurs at the critical Reynolds number. This number is not a fixed value since the transition is also dependent on a number of other factors such as the particle size, the geometry and the roughness of the tubes. Furthermore the transition occurs smoothly and there is a transition region in which the flow is neither completely turbulent or completely laminar. However in general the critical Reynolds number is expected to increase with the solid mass fractions [35]. The range of Reynolds number at which the authors observed the transition is also included in table 4.1.

Table 4.1: On overview of the friction factor correlations.

Author	Correlation	Regime
Wenji et al. [69]	laminar: $f = \frac{64}{Re_{mod}}$ turbulent: $f = 4 \times 0.1021 Re_{mod}^{-0.2708}$	$Re_{mod,cr} = 2000 - 2300$
Xiao et al. [71]	laminar: $f = \frac{64}{Re_{mod}}$ turbulent: $f = 4 \times 0.3226 Re_{mod}^{-0.4271}$	
Zhang and Ye. [79] and Zhang et al. [76]	laminar: $f = \frac{64}{Re_{mod}}$ turbulent: $\frac{1}{\sqrt{f}} = \frac{2.0}{n^{0.75}} ln \left(Re_{mod} (0.25 f)^{\frac{2-n}{n}} \right) - \frac{0.2}{n^{1.2}}$	$Re_{mod,cr} = 1500 - 1900$ for d = 2 mm $Re_{mod,cr} = 1400 - 1900$ for d = 4.5 mm
Kumano et al. [35]	laminar: $f = \frac{64}{Re_{mod}}$ turbulent: $f = 0.3164 Re_{sol}^{-1/4}$	laminar $0 < Re_{mod}/Re_{sol} < 1$ turbulent $0 < Re_{mod}/Re_{sol} < 1$

The friction factor correlations are plotted against the modified Reynolds number in figure 4.4. The cor-
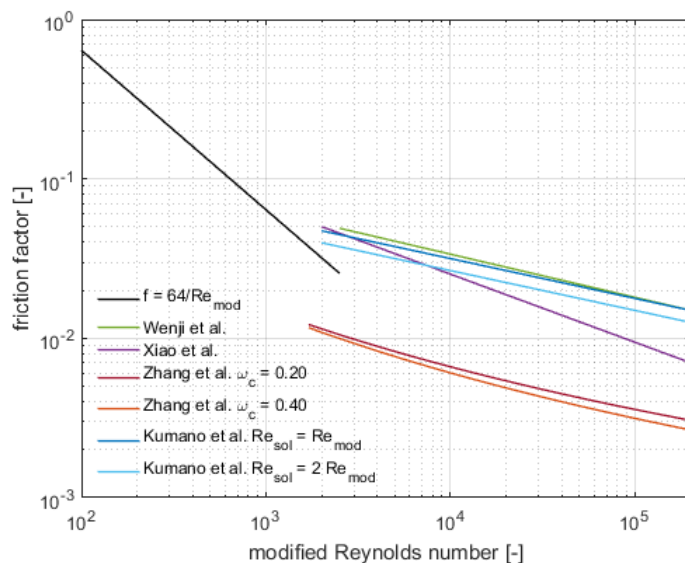
Figure 4.4: Comparison of the different friction factor correlations.

relation proposed by Kumano et al. makes use of the Reynolds number of the solution which can be as much as twice as high as the modified Reynolds number. Therefore the friction factor can lie anywhere in the area between the two lines plotted in the graph. From the graph it is clear that the correlation of Zhang et al. is not in agreement with the others correlations. This is probably since it is the only theoretical correlation while the other correlations are empirical relations fitted to experimental data. In this case the empirical correlations are preferable since the theoretical correlations are not able to describe all the complexities of the slurry flow. Another problem is that the equation of Zhang et al. is an implicit correlation for the pressure drop. This equation is iteratively which might affect the speed of the model.

The correlations are compared with experimental data in order to determine the most suitable correlation. The difference between the correlations is in the friction factor of the turbulent flow regime and in the critical Reynolds number. The pressure drop of different TBAB solid fractions and velocities has been measured by Wenji et al. [69]. Figure 4.5 compares the experimental data with the different correlations. The following observations can be made.

- The correlation of Wenji at al. gives the best approximation of the experimental data. This observation however has little value since the correlation of Wenji et al. is developed using the very same data.

- None of the correlations accurately predicts the critical Reynolds number. The correlation of Kumano et al. provides an accurate estimation of the critical Reynolds number for CHS with a solid fraction of 10.5 and 17.1 wt%. However this correlation fails to give good approximation of the critical Reynolds number for higher solid fractions.

- The solid fraction has distinct influence on the pressure drop for the turbulent flow regime. However this influence is almost completely neglected by Kumano et al. This is because their correlation for the turbulent flow regime uses the Reynolds number of the solution instead of the modified Reynolds.

As explained in section 2.3 the turbulent flow might become laminar when the solid mass fraction of the slurry increases. This phenomenon can easily be observed by measuring the pressure drop of the CHS at different solid fractions [34, 35, 69]. The experimental data indicates that both Kumano et al. and Wenij et al. provide an accurate prediction of the pressure in the turbulent regime before the re-laminarization occurs. The critical Reynolds at which the Re-laminarization occurs is best predicted by Kumano et al. however this correlations is not without some major flaws.

- The critical Reynolds number is determined by the ratio between the modified Reynolds number and the Reynolds number of the solution. If the velocity of the solution is very low or very high it means that the critical Reynolds number can also become very low or very high. Therefore the model may predict a
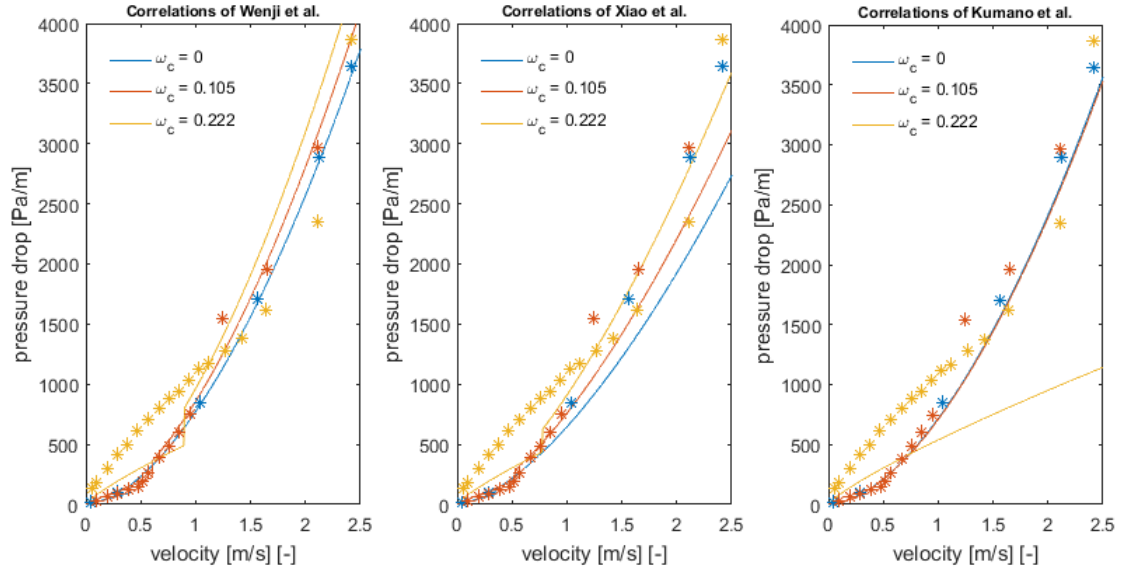
Figure 4.5: Comparison of the pressure drop correlations with the experimental data of Wenji et al. [69].

laminar flow with a Re_{mod} of 5000 in one situation and a turbulent flow with a Re_{mod} of 1000 in another situation. This is not supported by the measurements as shown for a solid fraction of 22.2 wt% in figure 4.5.

- For low mass fraction the modified Reynolds number is very close to the Reynolds number of the solution. This means that the flow will always be turbulent for low TBAB concentrations even if the Reynolds number is very low.

So in conclusion the correlation of Kumano et al. might provide the most accurate estimation of the critical Reynolds number. However this correlation is only valid for a limited range of solid fractions and Reynolds numbers. Therefore the correlation of Wenji et al. is selected as the most suitable correlation to use in the model.

4.3. Heat transfer during the melting of TBAB

Kumano et al. [36] measured the Nusselt number of melting TBAB in tubes. They compared their findings with a theoretical expression for the Nusselt number. They found that the actual Nusselt number was 1.5 to 2.5 times higher than the theoretical value. Based on their measurements they proposed a different correlation based on the modified Reynolds number and the Prandtl number. The Prandtl number for these relations has been defined as:

$$Pr = \frac{C_{p,sol}\mu_{sol}}{\lambda_{sol}} \tag{4.14}$$

Several different authors also investigated the heat transfer in tubes. They also proposed empirical correlations for the Nusselt number. An overview of the Nusselt number correlations developed for melting TBAB in a tube are shown in table 4.2.

The different correlations are compared with the measurments of Kumano et al. [36]. The experimental data has been obtained for an initial mass fractions of 22.5 wt% and inner diameter of the tube of 7.5 mm. A comparison is shown in figure 4.6.

Figure 4.6 shows a comparison of the data for one specific condition. The data show a sudden drop in the Nusselt number at a solid fraction of 0.16. This drop is caused by the re-laminariziation of the CHS. As explained earlier none of the correlations can accurately predict the critical Reynolds number at which this transition occurs. This also means that none of the correlations show this drop in the Nusselt number. The dotted line however represents the Nusselt number obtained with the correlation for a laminar flow regime. The paper the Kumano et al. [36] reports a better correlation between the experimental data and their correlation. The difference between their study and the result in figure 4.6 can be explained by the different

Table 4.2: On overview of the correlations for the Nusselt number of melting TBAB in tubes.

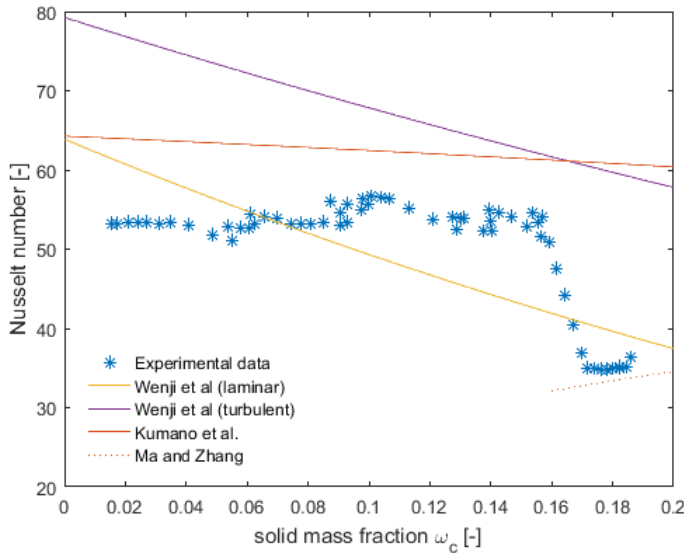| Author	Correlation	Regime
Wenji et al. [68]	$Nu = 1.231 \times 10^{-5} Re_{mod}^{1.6606} Pr^{0.7073}$	laminar
	$Nu = 5.254 \times 10^{-4} Re_{mod}^{0.9097} Pr^{1.1202}$	turbulent
Kumano et al. [36]	$Nu(x) = 3.33 Gz_{mod}^{0.18} \omega_c^{0.42} \left(\frac{d_i}{L_c} \right)^{0.55}$	laminar $120 \leq Gz_{mod} \leq 4300$
	with $Gz_{mod} = Pr Re_{mod} \frac{d_{in}}{x}$	$0.03 \leq \omega_c \leq 0.18$
		$18.3 \leq \frac{d_i}{L_c} \leq 24.8$
	$0.023 Re^{0.8} Pr^{1/3}$	turbulent
Ma and Zhang [44]	$Nu = 0.0598 Re_{mod}^{0.711} Pr^{1/3} \left(1 + \frac{\Delta \omega_c \Delta h_{melt}}{C_p \Delta T} \right)^{0.457}$	$0.10 < \omega_c < 0.25$

Figure 4.6: Nusselt number correlations compared to the experimental data of Kumano et al. [36].

correlations used to determine the properties of the fluid. For example the thermal conductivity of the solution was not known by Kumano et al. so they used the thermal conductivity of water instead. Furthermore they also used different equations for the modified Reynolds number, the viscosity and the specific heat.

The convective heat transfer coefficent has also been measured by Kumano et al. [36] and Wenji et al. [68]. The convective heat transfer coefficient can easily be expressed as a function of the Nusselt number:

$$\alpha = \frac{Nu \lambda_{sl}}{d_{in}} \tag{4.15}$$

The convective heat transfer coefficients obtained with the differents correlations are compared with the experimental data obtained by Wenji et al. [68]. During the experiments the crystals were produced from a solution with an initial TBAB concentration of 30 wt%. They used a tube with an inner diameter of 14 mm and with a constant heat flux imposed on the wall. A comparison between the experimental data and the correlations is shown in figure 4.7 and figure 4.8. The following observations are made:

- The correlation of Wenji et al. and Ma and Zhang provide a reasonable result for the convective heat transfer coefficient at low velocities. This is the case for both laminar (v = 0.70 m/s) and turbulent (v = 1.75 m/s) flow regime.

- All three models predict a negative influence of the solid fraction on the heat transfer coefficient. However the experimental data shows a positive effect on the heat transfer coefficient especially for higher solid mass fractions.

- The correlation of Wenji et al. provides the most accurate estimation although a better agreement should be expected since this correlations is obtained using the same experimental data. The main difference might be that the correlations are obtained using different correlations for the fluid properties.
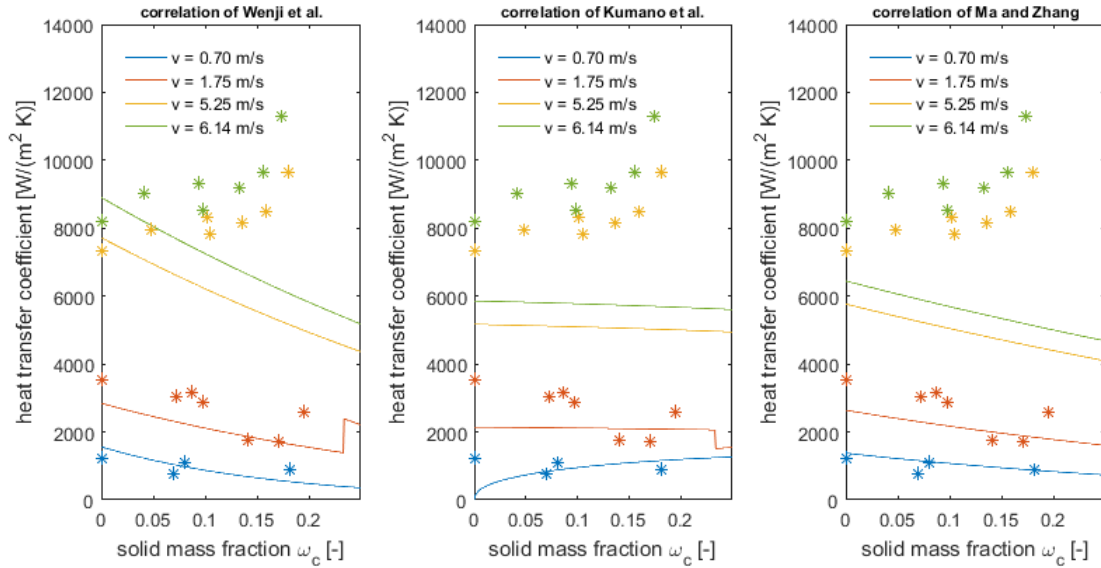
Figure 4.7: Convective heat transfer coefficient correlations compared with experimental data of Wenji et al. [68].
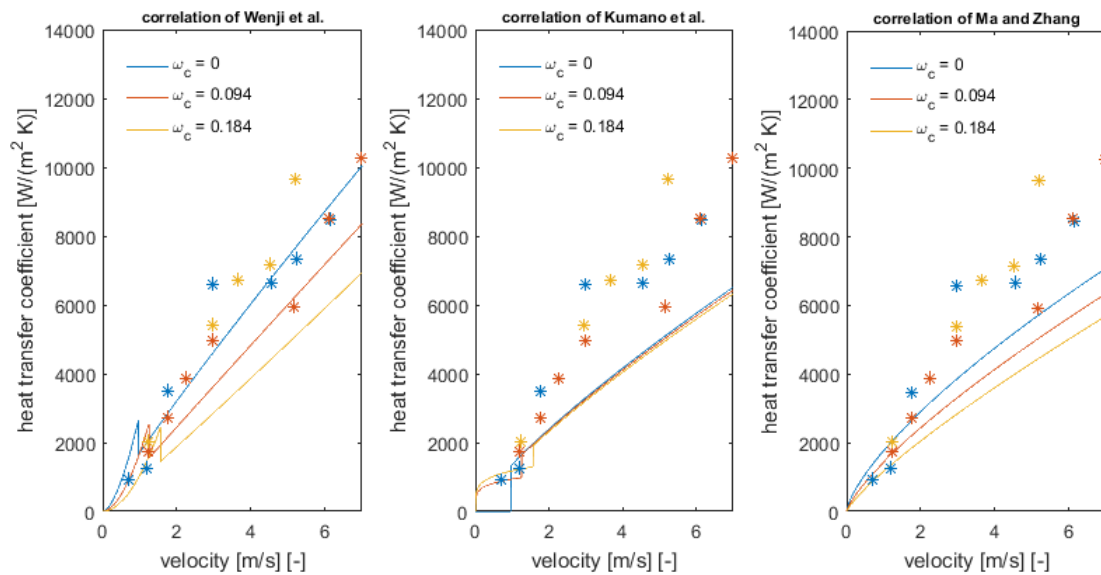
Figure 4.8: Convective heat transfer coefficient correlations compared with experimental data of Wenji et al. [68].

In conclusion the correlation of Wenji et al. provides the most accurate result and is therefore the most suitable to use in the model. However the correlations only has good accuracy for velocities up to 2 m/s. For higher velocities the accuracy of the correlations reduces especially for higher solid mass fractions.

4.4. PRESSURE DROP IN PLATE HEAT EXCHANGERS

In the pilot plant the TBAB crystals are produced in a plate heat exchanger. Very few studies have been conducted into the behavior of TBAB in plate heat exchangers. Ma and Zhang [42] did measure the pressure drop

of TBAB CHS flowing through a plate heat exchanger without any heat exchange. They repeated the experiment for several different solid mass fractions. Based on their data they derived an empirical correlation for the friction factor of the heat exchanger. This correlation was also validated for a melting TBAB CHS. Ma and Zhang reported that the pressure drop increased for higher mass fractions. This was also observed for ice slurry flowing through plate heat exchangers [8].

The study of Ma and Zhang is the only study specifically investigating TBAB in plate heat exhangers. Their findings can be compared with correlations not specifically determined for slurries. Generally speaking the pressure in the heat exchangers can be attributed to three mechanism.

- The pressure drop as a result of the friction.

- The difference in hydrostatic pressure at the inlet and the outlet of the component.

- The difference in the dynamic pressure caused by the difference in the velocity at the inlet and outlet.

The density of the water at the inlet and the outlet of the heat exchanger is almost the same since there is no phase change. The port diameter at the inlet and the outlet is also the same so due to the continuity the velocity at the inlet and the outlet is approximately the same. For the CHS there the density of the slurry increases with the crystal production although the difference of the density at the in and outlet is usually less then 1 %. So the change in the dynamic pressure can be neglected. The hydrostatic pressure is also neglected since it remains much smaller then the frictional pressure drop. The friction losses in the plate heat exchanger can be divided into the pressure drop in the ports and the pressure drop over the plate:

$$\Delta P = \Delta P_p + \Delta P_{pt} \tag{4.16}$$

Most friction factor correlations in the literature describe only the pressure drop over the plates. However certain friction factors in the literature also include the pressure drop in the ports. The friction factors which only include the friction over the plates are denoted by f_p while f denotes friction factor correlations which include the pressure drop in the ports. If the pressured drop in the ports is not included in the correlation then the following relation can be used [7]:

$$\Delta P_{pt} = 1.5\rho \frac{v_{pt}^2}{2} \tag{4.17}$$

The friction factor of the plates is usually described by an empirical correlation. Several different correlations are presented in table 4.3. These relations are selected since they are also valid for a low Reynolds numbers. However none of these correlations are developed for slurry flow so the applicability for TBAB CHS may be limited. Studies of slurries flowing in plate heat exchangers are very limited. Singh and Kachhwaha [61] proposed a theoretical model for the pressure drop of ice slurries but it did not provide any reasonable results. Bellas et al. [8] measured the pressure drop of ice mixture with mass fractions ranging from 0 to 20 wt% flowing through a plate heat exchanger. They used an small heat exchanger with a hydraulic diameter of 0.4 mm and a plate length of 311 mm. They did not provide any correlations for their results although a friction factor correlation could be obtained from their experimental data.

$$f = 46.62 Re^{-0.132} \tag{4.18}$$

The correlations in table 4.3 are used to predict the pressure drop of the actual plate heat exchanger used in the pilot plant. The corrugation angle of the heat exchanger is not specified however it is assumed to be 60° based on the horizontal axis. Figure 4.9 shows a comparison of the pressure drop for a TBAB solution (dotted lines) and a TBAB CHS with a volume fraction of 0.40 (solid lines).

Figure 4.9 shows that the correlations of Bellas at al. and Ma an Zhang predict the largest pressure drop. These correlations are the only correlations obtained for a slurry flow however this cannot explain the large difference in the pressure drop of the solution. Based on the figure 4.9 alone it is impossible to determine the most suitable correlation since the correlations are also heavily dependent on the geometry of the equipment. The most suitable correlation for the model must be determined using measurements of the actual systems. However the figure provides some insight in the relevance of the correlations.

- The corrugation angle and the port diameter of the heat exchanger used by Ma and Zhang is not known. This might explain why their correlations predicts a much higher pressure drop than many of the other correlations. The corrugation angle used for the study of Bellas et al. is also unknown. However the difference between these studies and the other studies might also be explained by the size of the equipment; the correlations of the other studies are obtained for industrial size equipment.

Table 4.3: On overview of the pressure drop correlations for plate heat exchangers with corrugation angle of 60°.

Author	Correlation	Regime
Ma and Zhang [42]	$f = \frac{51.002}{Re_{mod}^{0.3}}$	$60 \leq Re_{mod} \leq 1200$ $0.05 \leq \phi \leq 0.175$
Sinnott and Towler [62]	$f = 4.8 Re^{-0.3}$ $\Delta p_{pt} = 1.3 \rho \frac{v_{pt}^2}{2}$	
VDI heat atlas [67]	$f_0 = 64/Re$ $f_{1,0} = 597/Re + 3.85$	$Re < 2000$
	$f_0 = (1.8 ln(Re) - 1.5)^{-2}$ $f_{1,0} = 39/Re^{0.289}$	$Re \geq 2000$
	$\frac{1}{\sqrt{f_p}} = \frac{cos(\beta)}{\sqrt{0.18 tan(\beta) + 0.36 sin(\beta) + f_0/cos(\beta)}} + \frac{1 - cos(\beta)}{\sqrt{f_{1,0}}}$	
Focke et al. [25]	$f = 57.5/Re + 0.093$ $f = 0.8975/Re^{0.263}$	$120 < Re < 1000$ $1000 < Re < 42000$
Kumar et al. [37]	$f = 24.0/Re$ $f = 3.24/Re^{0.457}$ $f = 0.760/Re^{0.215}$	$Re < 40$ $40 \leq Re \leq 400$ $Re > 400$
Thonon et al. [65]	$26.34 Re^{-0.830}$ $0.572 Re^{-0.217}$	$Re \leq 550$ $Re > 550$
Bellas et al. [8]	$f = 46.62 Re^{-0.132}$	

- Bellas et al. [8] reported that the pressure drop increased from approximately 47 to 53 kPa when the ice slurry fraction increased from 0 to 20 wt%. Zhang et al. [42] found a pressure drop increase from approximately 30 to 45 kPa for a solid volume fraction of respectively 0 and 0.175. Based on these observations and figure 4.9 it can be concluded that the correlations from the VDI heat atlas does not work for slurries.

- Focke at al. and Thonon et al. predict a very large difference between the pressure drop of the slurry and the solution. This is because these correlations use the actual Reynolds number instead of the modified Reynolds number. As shown in figure 4.3, the difference between the actual and the modified Reynolds number can become quite significant for higher solid fractions. Since the actual Reynolds number does not describe this non-Newtonian behavior of the fluid it might be more suitable to use the modified Reynolds number instead.

4.5. Evaporation in plate heat exchangers

Two different boiling mechanisms can occur during the evaporation in plate heat exchangers: pool boiling and forced convection boiling. During pool boiling vapor bubbles are formed in a stationary liquid. In forced convection boiling the fluid is flowing over the heated surface due to external forces. There is no agreement about which of these two processes dominates in plate heat exchanger [22] although forced convection boiling is usually related to high mass fluxes and pool boiling is related to high heat fluxes. The boiling process can also be characterized using the excess temperature (the temperature difference between the surface and the saturation temperature). For different ranges of the excess temperature different boiling processes may occur. These processes, which are often described using the boiling curve, can be divided into four separate regimes. These regimes are for increasing excess temperature [48]:

- Natural convection boiling, this regime is encountered for an excess temperature ranging from about
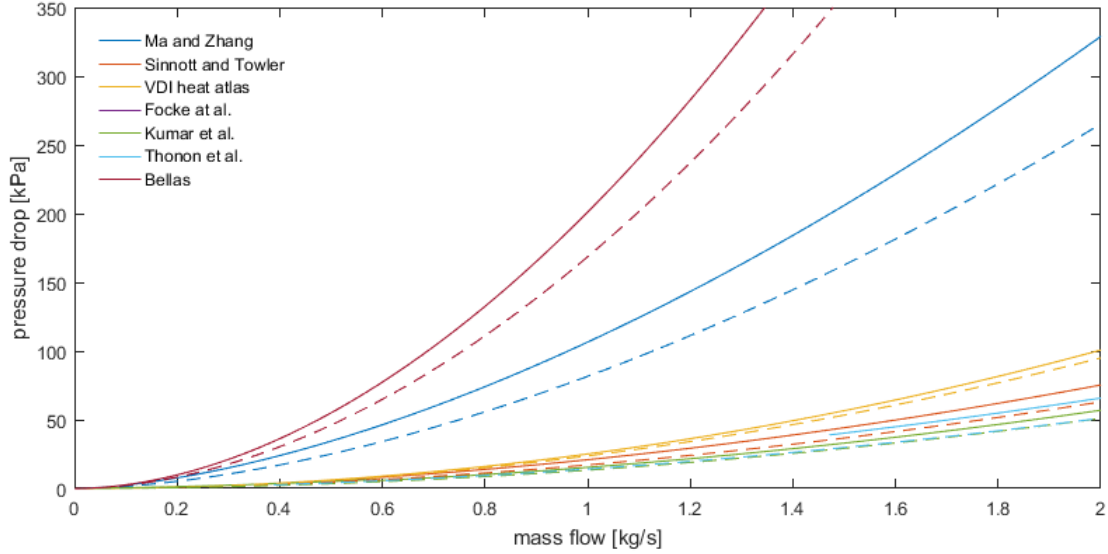
Figure 4.9: Comparison between the different correlations for the pressure drop in plate heat exchangers. The dotted lines represent the TBAB solution and the solid lines the TBAB CHS with a solid fraction ϕ_c of 0.40.

to 2 till 6 K. The heat transfer is dominated by natural convection and therefore this boiling regime is avoided in evaporators due to the low heat transfer.

- Nucleate boiling, in this regime the heat transfer is accelerated by the bubble formation in the liquid. This regime is characterized by high heat transfer.

- Transitional boiling, in this boiling regime the vapor starts to form a blanket on the heated surface. The vapor layer has a low thermal conductivity and obstructs the liquid from reaching the heated surface. Therefore this boiling regime is also undesirable because of its low heat transfer.

- Film boiling, in this regime the surface is covered with a stable vapor film. Nevertheless the heat transfer starts to increase again due to the effects of radiation.

In the pilot plant in Twello nucleate boiling is expected to be the dominant mechanism. The temperature difference is too low for film boiling and the other boiling regimes are avoided because of their low heat transfer. Donowski and Kandlikar compared several theoretical and empirical correlations used to describe evaporating in chevron plate heat exchangers [19]. They concluded that the correlation of Yan and Lin [72] provided an accurate representation of the their experimental data in combination with a good theoretical background. Other correlations describing nucleate boiling in plate heat exchangers include the correlations reported by Cooper [41], Huang et al. [29] and Amalfi et al.[2]. An overview of these correlations is presented in table 4.4. Palmer et al. [55] developed two separate equations for different refrigerants. They noted that the requirement of two separate equation could be due to the use of different lubricants.

The heat transfer in evaporators is usually described using a number of dimensionless properties. These include the equivalent mass flux defined as:

$$G_{eq} = G\left((1 - X_m) + X_m\left(\frac{\rho_L}{\rho_G}\right)^{0.5}\right) \tag{4.19}$$

The equivalent Reynolds number:

$$Re_{eq} = \frac{G_{eq}d_h}{\mu_L} \tag{4.20}$$

Equivalent boiling number:

$$Bo_{eq} = \frac{\dot{Q}_w/A}{G_{eq}\Delta h_{LG}} \tag{4.21}$$

The Nusselt number is related to the convective heat transfer coefficient using the properties of the liquid phase:

$$\alpha = \frac{Nu\lambda_L}{d_h} \tag{4.22}$$

Table 4.4: Overview of correlations for the Nusselt number for evaporation in plate heat exchangers.

Author	Correlation
Palmer at al. [55] (R22, R290 and R290/R600a)	$Nu = 2.7Re_L^{0.55}Pr_L^{0.55}$
Palmer at al. [55] (R32/R152a)	$Nu = Nu_L^{0.42}Fr^{0.0088} - log_{10}(p/p_{cr})^{1.5}Co^{1.5}M^{1.5}$
	with: $Nu_L = 0.16Re_L^{0.89}Pr_L^{0.4}$
	and $Fr = \frac{G^2}{g\rho^2 d_h}$ and $Co = \left(\frac{\rho_G}{\rho_L}\right)^{0.5}\left(\frac{1-X}{X}\right)^{0.8}$
Cooper [41]	$\alpha = 55\left(\frac{p}{p_{cr}}\right)^{(0.12-0.2\log_{10} Rp)}\left(-\log_{10}\left(\frac{p}{p_{cr}}\right)\right)^{-0.55}(\dot{Q}_w/A)^{0.67}M^{-0.5}$
Amalfi et al.[2]	if $Bd < 4$: $Nu = 982\left(\frac{\beta}{70°}\right)^{1.101}\left(\frac{G^2 d_h}{\rho_m\sigma}\right)^{0.135}\left(\frac{\rho_L}{\rho_G}\right)^{-0.224}Bo^{0.320}$
	else: $Nu = 18.495\left(\frac{\beta}{70°}\right)^{0.248}\left(\frac{X_m Gd_h}{\mu_G}\right)^{0.135}\left(\frac{Gd_h}{\mu_L}\right)^{0.351}\left(\frac{\rho_L}{\rho_G}\right)^{0.223}Bd^{0.235}Bo^{0.198}$
	with: $Bd = \frac{g(\rho_L-\rho_G)d_h^2}{\sigma}$
Huang et al. [29]	$Nu = 1.87 \times 10^{-3}\left(\frac{\dot{Q}_w/A}{\lambda_L T_{sat}}\right)^{0.56}\left(\frac{\Delta h_{LG}d_o\rho_L^2 Cp,L^2}{\lambda_L^2}\right)Pr_L^{0.33}$
	with: $d_o = 0.0146 \times 35°\left(\frac{2\sigma}{g(\rho_L-\rho_G)}\right)^{0.5}$
Han et al. [27]	$\alpha = Ge1Re_{eq}^{Ge2}Bo_{eq}^{0.3}Pr^{0.4}$
	with: $Ge1 = 2.81\left(\frac{b}{d_h}\right)^{-0.041}\left(\frac{pi}{2} - \frac{\beta}{180}\pi\right)^{-2.83}$
	and $Ge2 = 0.746\left(\frac{b}{d_h}\right)^{-0.082}\left(\frac{\pi}{2} - \frac{\beta}{180}\pi\right)^{0.61}$
Yan and Lin [72]	$Nu = 19.26Re_{eq}Pr_L^{1/3}Re^{-0.5}Bo_{eq}^{0.3}$

The pressure drop during the evaporation has also been investigated. The frictional pressure drop increases with the vapor fraction [22]. The vapor has a much higher specific volume so the velocity and turbulence of the flow is much higher for the vapor phase than for the liquid phase. Furthermore it has been observed that the heat flux has no significant influence on the pressure drop while the pressure drop of R134a could be reduced by increasing the condensation pressure [72]. The pressure drop during the evaporation is usually expressed using a friction factor:

$$\Delta p_f = f\frac{L_p}{d_h}\frac{G^2}{2\rho_m} \tag{4.23}$$

Several correlations for the friction factor are included in table 4.5. These correlations are only for the frictional pressure drop; the pressure drop in the port and due to acceleration are not included in these correlations.

4.6. CONCLUSION

in this chapter several correlations for the pressure drop and the heat transfer of TBAB are discussed. These correlations commonly use the modified Reynolds number to account for the non-Newtonian behavior of the

Table 4.5: Overview of the friction factor correlations for evaporation in plate heat exchangers.

Author	Correlation
Amalfi et al.[2]	$f = 4 \times 15.698 C \left(\frac{G^2 d_h}{\rho_m \sigma} \right)^{-0.475} \left(\frac{(\rho_L - \rho_G) g d_h^2}{\sigma} \right)^{0.255} \left(\frac{\rho_L}{\rho_G} \right)^{-0.571}$
	with: $C = 2.125 \left(\frac{\beta}{70°} \right)^{9.993} + 0.955$
Han et al. [27]	$f = Ge3 Re_{eq}^{Ge4}$
	with: $Ge3 = 64.710 \left(\frac{b}{d_h} \right)^{-5.27} \left(\frac{\pi}{2} - \frac{\beta}{180} \pi \right)^{-3.03}$
	and $Ge4 = -1.314 \left(\frac{b}{d_h} \right)^{-0.62} \left(\frac{\pi}{2} - \frac{\beta}{180} \pi \right)^{-0.47}$
Huang et al. [29]	$f = \frac{3.81 \times 10^4 F_{r,f}}{Re_{tp}^{0.9} (\rho_L / \rho_G)^{0.16}}$
	with: $Re_{tp} = \frac{GDh}{\mu}$ and $F_{r,f} = 0.183 \left(\frac{\beta}{30°} \right)^2 - 0.275 \frac{\beta}{30°} + 1.10$
Yan and Lin [72]	$f = 4 \times 6.947 \times 10^5 Re_{eq}^{1.109} Re^{-0.5}$ for $Re_{eq} < 6000$
	$f = 4 \times 31.21 Re_{eq}^{0.04557} Re^{-0.5}$ for $Re_{eq} \geq 6000$

TBAB CHS. The modified Reynolds number can be defined using the flow behavior index (equation 4.5) and the fluid consistency index (equation 4.13). A correction factor for the fluid consistency has been proposed in order to describe the influence of the initial mass fractions.

The pressure drop of TBAB CHS in tubes is best described by the friction factor correlation of Wenji et al. [69]. However, increasing the solid mass fraction often leads to re-laminarization of the fluid. None of the correlations provided and accurate estimation of the critical Reynolds number at which the re-laminarization occurs.

The heat transfer of melting TBAB CHS in tubes has also been measured by several authors. The proposed correlations only provide an accurate estimation of the Nusselt number for low velocities. At high Reynolds number the solid mass fractions is observed to have a positive effect on the Nusselt number however this is not accurately described by any of the correlations.

The evaporation in plate heat exchangers can be described by a number of different correlations. These suitability of these correlations should still be determined using the experimental data of the system.

THE MODEL OF THE TBAB AIR CONDITIONING SYSTEM

A model of a TBAB air conditioning system has already been developed by Zak [74]. This model has been used as a starting point for a new and improved model of the system. In this chapter the modeling approach of each individual component is presented. In this chapter the equations and correlations used to model each components are discussed.

5.1. AIR COOLER

The air cooler is placed at the utilization side of the system. It consists out of a number of finned tubes through which the CHS flows. When there is a cooling load air from the room is blown over the tubes and cooled down by melting the CHS. The dimensions of the tubes are shown in table 5.1. A further overview of the properties of the air cooler as specified by the manufacturer can be found in appendix B. The air cooler

Table 5.1: The parameters of the TBAB side of the air cooler.

Property	Value	Unit
Number of tubes	180	[-]
Number of circuits	15	[-]
Tube heat transfer area length	0.6	[m]
Outer diameter of the tubes	10.12	[mm]
Tube wall thickness	0.4	[mm]
Internal area	3.16	[mm]
External area	31.2	[mm]

makes use of tubes with rectangular fins attached to it. The tubes are made out of copper while the fins are made out of aluminum. The main purpose of the fins is to increase the heat transfer area. The properties of these fins are given in table 5.2.

Table 5.2: The parameters of fins of the air cooler.

Property	Value	Unit
Fin height	25	[mm]
Fin width	25	[mm]
Fin spacing	4.2	[mm]
Fin thickness	0.25	[mm]

TBAB CHS SIDE

In the air cooler the TBAB CHS will melt inside the tubes. The heat transfer of melting TBAB and the friction factor have already been discussed in chapter 4. However as shown in figure 5.1 the air cooler consists out

Figure 5.1: The pilot system in Twello before the insulation was installed. In the top the air cooler can be seen. It is connected the other components with the grey tubes. Pleas notice the sensors implemented in the system. These sensor are not necessarily placed at the in- or outlet of the components.

Figure 5.2: The pilot system in Twello before the insulation was installed. The white vessel is the storage tank which is connected with the grey tubes to the other components. The airducts is shown in the background; it has a number of bends which are include in the pressure drop calculations. The black sensors measure the gauge pressure; notice how some sensors are placed much further from the ground than others.
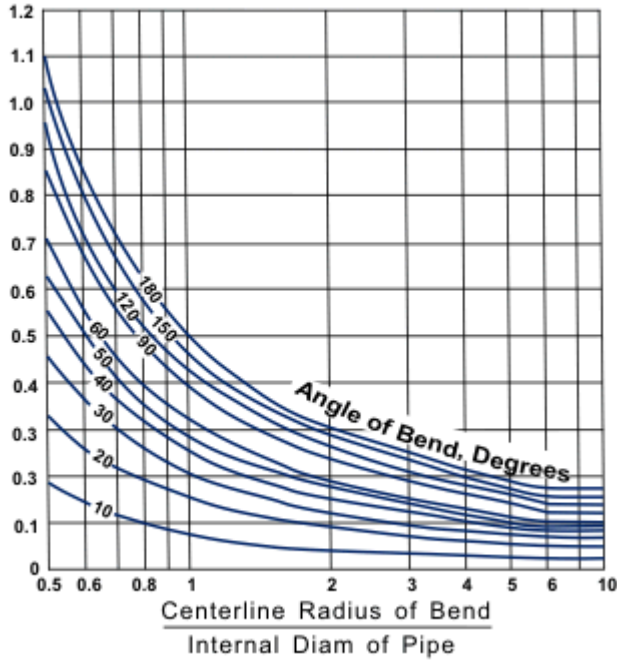
Figure 5.3: The bend loss coefficent[6].

of several tube rows connected with each other with 180° U-bends. Each circuit includes eleven of these U-bends and therefore the pressure drop at the CHS side of the air cooler is dominated by the pressure drop in these bends. Babcock and Wilcox [6] provide a correlation which can be used to estimate the pressure drop in these bends. This relation uses a bend loss coefficient which can be determined using figure 5.3. For this specific application the bend loss coefficient is determined to be 0.28. The pressure drop in a single U-bend can be expressed as:

$$\Delta p = \tfrac{1}{2} f \rho_{sl} v^2 \tfrac{\pi d_b}{2} + \tfrac{1}{2} \zeta_b \rho_{sl} v^2 \tag{5.1}$$

AIR SIDE
The fins will result in an increased heat transfer area in the heat exchanger. However due to temperature gradient in the fins and in the air the heat transfer does not proportionally increase with the heat transfer area. The influence of the fins on the heat transfer is described by the fin efficiency:

$$\eta_{fin} = \frac{\tanh\left(\chi \frac{d_o}{2} \sqrt{\frac{2\alpha}{\lambda_{fin}\delta_{fin}}}\right)}{\chi \frac{d_o}{2} \sqrt{\frac{2\alpha}{\lambda_{fin}\delta_{fin}}}} \tag{5.2}$$

With:

$$\chi = \left(\frac{d_o}{d_i} - 1\right)\left(1 + 0.35 ln\left(\frac{d_o}{d_i}\right)\right) \tag{5.3}$$

The fin efficiency is used to calculate a virtual convective heat transfer coefficient that will be used when calculating the overall heat transfer coefficient.

$$\alpha_v = \alpha_o \left[\frac{A_{tube}}{A} + \eta_{fin}\frac{A_{fin}}{A}\right] = \alpha_o \left[1 - (1 - \eta_{fin})\frac{A_{fin}}{A}\right] \tag{5.4}$$

Finally, the overall heat transfer coefficient can be expressed as:

$$\frac{1}{U_o} = \frac{1}{\alpha_v} + \frac{A}{A_i}\left(\frac{1}{\alpha_i} + \frac{d_o - d_i}{2\lambda_{wall}}\right) \tag{5.5}$$

The above equation is for the overall heat transfer coefficient based on the outer surface. This equation can be rewritten for the internal area of the tubes:

$$\frac{1}{U_i} = \frac{1}{U_o \frac{A_i}{A}} = \frac{1}{\alpha_i} + \frac{d_o - d_i}{2\lambda_{wall}} + \frac{1}{\alpha_v}\frac{A_i}{A} \tag{5.6}$$

Table 5.3: The parameters of AC-70X-30M heat exchanger [1].

Property	Value	Unit
Height	0.526	[m]
Width	0.111	[m]
Number of plates	30	[-]
Plate length	0.466	[m]
Plate width	0.100	[m]
Plate thickness	0.3	[mm]
Average distance between the plates	2.0	[mm]
Hydraulic diameter	3.3	[mm]
Port diameter	18	[mm]
Surface enhancement factor	1.22	[-]
Heat transfer area	1.71	[m^2]

Using the definition of the virtual heat transfer coefficient this can be further rewritten as:

$$\frac{1}{U_i} = \frac{1}{\alpha_i} + \frac{d_o - d_i}{2\lambda_{wall}} + \frac{1}{\alpha_0} / \left[\eta_{fin} \frac{A_{fin}}{A_i} + \frac{A_{tube}}{A_i} \right] \tag{5.7}$$

The air is blown over the tubes by a fan. The power consumption of the fan can be related to the pressure drop of the air flow. The fan efficiency is estimated to be 55 % while the mechanical efficiency is assumed to be 95 %. The air also passes through a channel with a number of sharp bends. The pressure drop in this channel is also included when calculating the power consumption of the fan.

$$\dot{W} = \frac{\dot{V}\Delta P}{\eta_{fan}\eta_{mech}} \tag{5.8}$$

5.2. GENERATOR

The TBAB crystals are produced when the TBAB solution is cooled down. This process occurs in the generator. The pilot plant uses a plate heat exchanger of type AC-70X-30M produced by Alfa-Laval. The properties of heat exchanger are shown in table 5.3. The hydraulic diameter given in the table is only valid if there is no crystal layer present. Otherwise the hydraulic diameter can be expressed as:

$$d_h \approx \frac{2(b - 2\delta_c)}{\Phi} \tag{5.9}$$

The heat transfer and pressure drop correlations used for the TBAB side of the heat exchanger have already been discussed in chapter 4. However several other correlations are required in order to describe the crystallization process.

CRYSTAL GROWTH

The crystal growth model is very similar to the model developed by Zak [74]. The supersaturation of the solution is the driving force of the crystallization process. An analogy with heat transfer has been made in which the subcooling corresponds to the temperature difference and the crystal production is the analogy for the heat flow.

$$\dot{m}_{c,prod} = k\rho_c A(w_{int} - w_{sat}) \tag{5.10}$$

The mass transfer coefficient is a function of the Schmidt and Sherwood number. The Schmidt number is defined as the viscous diffusion rate divided by the molecular diffusion rate.

$$Sc = \frac{\mu}{\rho D} \tag{5.11}$$

Another dimensionless number that is used is the Sherwood number. This is defined as the convective mass transfer rate divided by the diffusion rate. For this situation the characteristic length scale can be defined as the thickness of the crystal layer.

$$Sh = \frac{k}{D/\delta_c} \tag{5.12}$$

The Sherwood number can be expressed as a function of the Reynolds and Schmidt number. In the previous studies the following correlation for the Sherwood number has been used:

$$Sh = 0.2875 Re^{0.78} Sc^{1/3} \tag{5.13}$$

Other correlation for the Sherwood number can be found by using analogy with the fouling. For plate heat exchangers a relation based on the three region model of Von-Karman is proposed and validated by Li et al. [40].

$$Sh = (f/2) Sc Re + (f/2)^{0.5} \times (5(Sc-1) + 5 ln((5Sc+1)/6)) \tag{5.14}$$

These equations are implemented using a volume control technique. The crystallization process will be driven by the temperature difference of the volume element and the corresponding equilibrium phase change temperature. The volume fraction of the crystals can be expressed as a function of the crystal production rate:

$$\phi_c^{n+1} = \phi_c^n + \frac{\dot{m}_{c,prod}}{\rho_c \dot{V}} \tag{5.15}$$

The enthalpy of the next volume element is found using an energy balance:

$$h^{n+1} = h^n + \frac{\dot{Q}}{\dot{m}_{sl}} \tag{5.16}$$

The temperature and the TBAB fraction of the of an element are a function of the enthalpy and the crystal volume fraction:

$$T^{n+1}, w_{TBAB}^{n+1} = f\left(h^{n+1}, \phi^{n+1}\right) \tag{5.17}$$

CRYSTAL LAYER

Zak [74] has developed a model to estimate the steady state thickness of the crystal layer. For this model the assumption has been made that the energy loss due to friction is equal to the removal work of the crystal layer. However in reality the friction losses in the plate heat exchanger can be attributed to two phenomena:

- The friction of the fluid with the surface of the plate heat exchangers.

- The energy losses due to disruptions within the flow. The disruption can be caused by among other things bends in the channel, mixing of the flows and vortices within the flow.

Arsenyeva et al. [3, 4] have studied and modeled the flow in plate heat exchangers. One of their goals was to describe the formation of a fouling layer. Similar to the crystal layer the removal rate of the fouling layer is related to the friction at the walls. They defined a factor ψ which describes the share of the friction losses which can be contributed to the friction with the wall. They found this this factor can be obtained by a relation proposed by Kapustenko et al. [33]:

$$\psi = \left(\frac{Re}{a}\right)^{-0.15 sin(\beta)} \text{ if } Re > a \tag{5.18}$$

$$\psi = 1 \text{ if } Re \leq a \tag{5.19}$$

With:

$$a = 380/\left(tan(\beta)\right)^{1.75} \tag{5.20}$$

The equations are solved for the flow regime used in the installation in Twello. The results show that the factor ψ is always 1 regardless of the inclination angle β. This supports the assumption that the friction losses are equal the the removal forces. This mean that he crystal layer can be predicted by using the following equation:

$$\dot{V}\Delta p = \dot{W}_{rem} \tag{5.21}$$

The removal work of TBAB crystals can be related to the scrapping force in scrapped heat exchanger. Daitoku and Utaka measured the scrapping force needed to remove TBAB crystals from a crystal layer [15]. They reported that the structure of the initially formed crystal layer differs from the structure of the crystal layer
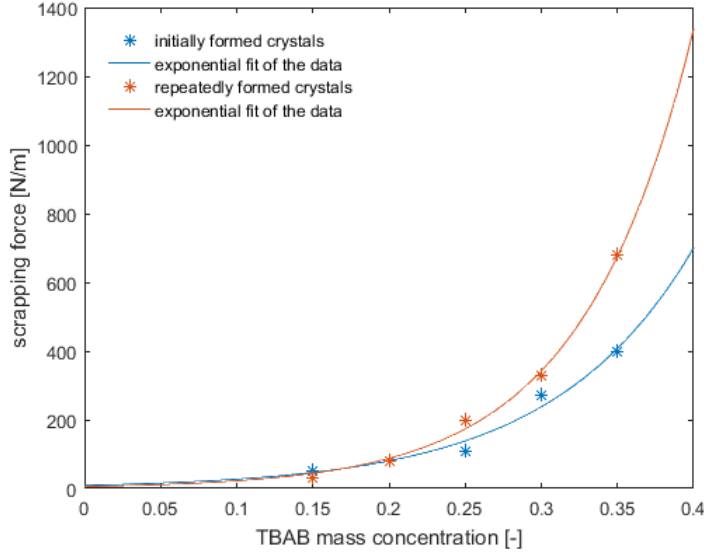
Figure 5.4: The scrapping force of initially and repeatedly formed TBAB hydrates on a brass surface [14].

formed after several removals. Furthermore they discovered that the initial mass fraction has a very large impact on the required removal force. The results of their experiments with a brass surface are shown in 5.4.

The scrapping force is also dependent on the thickness of the crystal layer. For this research this effect is neglected since the influence of the crystal layer thickness is much smaller then the influence of the initial mass fractions. For another material, PTFE, the removal force was independent on thickness of the crystal layer [15]. However, this material also has a much lower removal force due to its very smooth surface. Therefore, the experiments obtained for a brass surface expected to more representative for the actual heat exchanger. As shown in figure 5.4 the experimental data can be fitted to an exponential correlation.

$$\text{Initially formed: } F_{scrap} = 9.286 e^{10.81 w_{TBAB}} \tag{5.22}$$

$$\text{Repeatedly formed: } F_{scrap} = 5.761 e^{13.62 w_{TBAB}} \tag{5.23}$$

The removal force is used to determine the removal work. It is assumed that the produced crystals have on average the same length as the thickness of the crystal layer. Therefore the removal time (the average time it takes before a crystal is removed from the surface) can be determined using the crystal growth rate:

$$t_{rem} = \frac{\delta_c}{\dot{m}_{c,prod}/(\rho_c A)} \tag{5.24}$$

Finally the removal work can be determined using the scrapping force and the removal time of the crystals.

$$\dot{W}_{rem} = \frac{F_{scrap} A}{t_{rem}} \tag{5.25}$$

COMPLETE MODEL

The model describes both the slurry and the refrigerant side of the plate heat exchanger using control volumes. On each side the temperature profile is calculated and on the slurry side the change of the crystal concentration and the crystal layer thickness is determined. The results of a typical simulation are shown in figure 5.5:

- The result in figure 5.5 show that the model predicts an equilibrium between the crystal production and the removal of the crystal. The result is an almost constant thickness of the crystal layer.

- In the superheating zone the heat fluxes are much smaller. As a result the crystal growth rate is much smaller in this zone and the subcooling remains too low to have a maximum crystal production.

- The temperature of the refrigerant in the superheating zone has been calculated with the outlet pressure while the inlet pressure is used for the evaporation zone. The result is a small discontinuity in the refrigerant temperature profile.
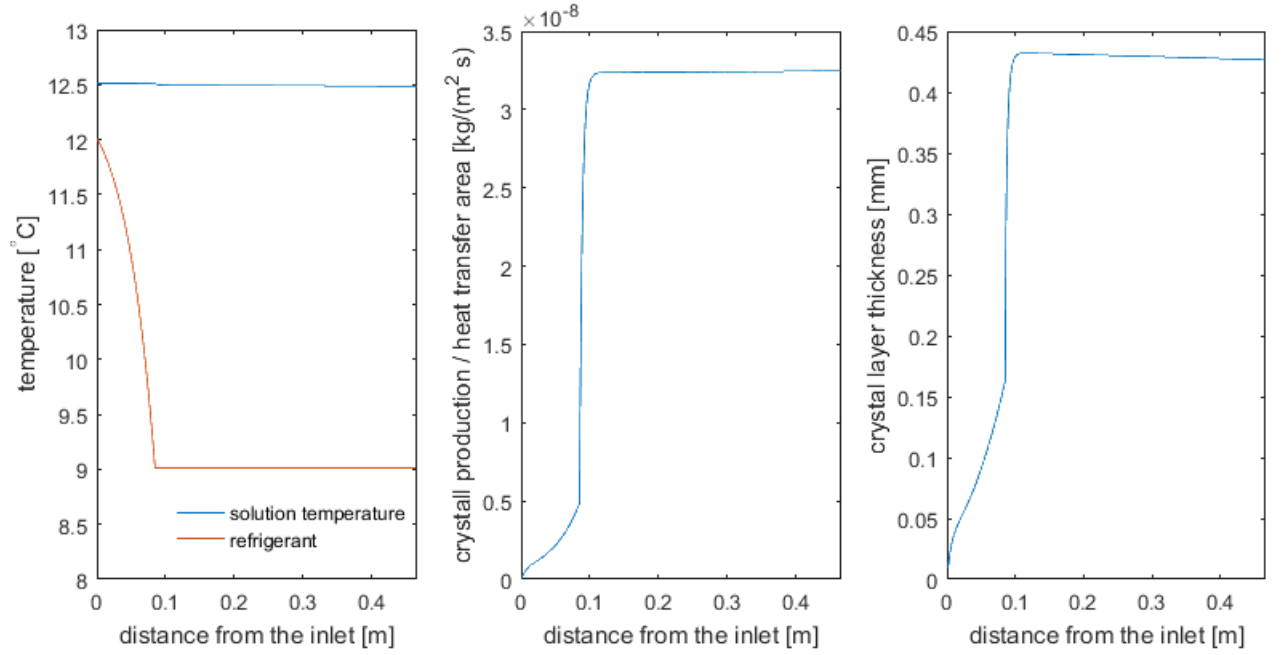
Figure 5.5: A typical result of a simulation of the generator for a mass flow of 0.40 kg/s and a ϕ_{in} of 0.20. The horizontal axis is the distance from the inlet of the CHS (the top) of the plate heat exchanger.

5.3. PUMPS

As shown in figure 5.2 the pilot plant utilizes two different T MAG-M peripheral pumps to pump the CHS through the system. The smallest pump, a T MAG-M2 pump, is used for the air-cooler side while the generator side uses the larger T MAG-M4 pump. The effects of potential energy on the required pressure is neglected so the relative pressure at the outlet of the pump is the same as the frictional pressure drop in the corresponding heat exchanger and the connecting pipes. The enthalpy of the CHS at the outlet of the pump can be expressed as function of the pressure drop:

$$h_{out} = h_{in} + \frac{\dot{W}}{\dot{m}} = h_{in} + \frac{\Delta P \dot{V}}{\dot{m}} \tag{5.26}$$

The pumps are frequency controlled so a desired pressure drop or mass flow can be met by controlling the rotational speed of the pump. The relation between the pressure drop and the flow rate can be obtained with the pump characteristic. The pump characteristic of the two pumps are provided by the manufacturer and can be found in appendix C. These pumps characteristics however do not include the performance of the pump at other rotational velocities.

The pump characteristic at lower frequencies can be obtained using the affinity laws. The affinity laws are based on the Buckingham π theorem for dimensional analysis. The main requirement when using these affinity laws is that the pumps are dynamically similar. This condition will be met since the geometry of the pump does not change. For a constant impeller diameter the affinity laws provides a relation of the flow rate based on the rotational speed and the conditions at a reference state. In this case the reference state is the pump operating at its nominal rotational speed. According the the affinity laws the ratio of the volumetric flow is proportional to the rotational speed:

$$\dot{V} = \dot{V}_{ref} \left(\frac{N}{N_{ref}} \right) \tag{5.27}$$

The head of the pump can be expressed as:

$$H = H_{ref} \left(\frac{N}{N_{ref}} \right)^2 \tag{5.28}$$

And the power can be expressed as:

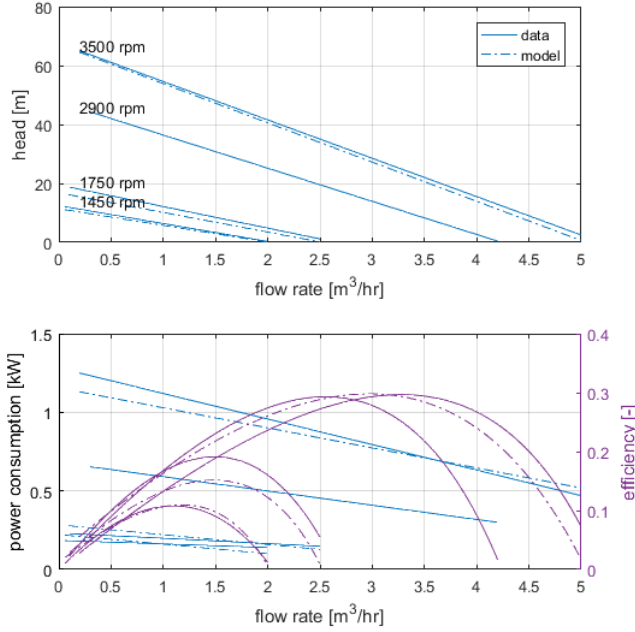$$P = P_{ref} \left(\frac{N}{N_{ref}} \right)^3 \tag{5.29}$$

Figure 5.6: A comparison between the model and the pump characteristic of the manufacturer.

The efficiency of the pump is equal to:

$$\eta = \frac{\dot{V}H}{P} \tag{5.30}$$

The affinity laws assume that the efficiency of the pump is not affected by the change in rotational speed. This assumption is not valid for this type of pumps. Van Putten and Colonna [66] described a different method to construct a pump characteristic. They assumed a parabolic pressure head curve and they used a dimensionless analysis to predict the head of the pump at different rotational speeds. This method is applied to the linear head curve given by the manufacturer. In this situation the equations for the flow rate and the head reduce to equation 5.27 and equation 5.28. However they also proposed a more accurate relation for the efficiency curve:

$$\eta = \eta_d \left[1 - \left(1 - \frac{\dot{V}}{\dot{V}_d} \frac{N}{N_d} \right)^2 \right] \tag{5.31}$$

The efficiency can also be used to determine the power consumption of the compressor:

$$P = \frac{H\dot{V}}{\eta} \tag{5.32}$$

The method Van Putten and Colonna has been validated using an older version of the pump characteristic of the T MAG-M2 pump. This version of the pump characteristic also includes the performance at other rotational velocities. A comparison between the data and the model is shown in figure 5.6. As shown in the figure the head of the pump is accurately predicted by the model for a rotational speed of 1450 and 3500 rpm. The deviation at 1750 rpm cannot be explained by the model but it is also unlikely that is would be accurately predicted by another model. The deviation in the efficiency is also the largest for a rotational speed of 2900 rpm however this is partly due to the difference in the predicted head of the pump. However the efficiency is only used to predict the power consumption of the pump and the power consumption is reasonably well predicted by the model. The same model has also been used to construct the pump characteristic of the actual pumps in the system. These pump characteristic can be found in appendix C.

5.4. COMPRESSOR
The pilot plant uses a Bitzer LH44E/2FES-3Y condensing unit. This unit includes a 2FES-3Y-40S compressor. The properties of this compressor are shown in table 5.4.

Table 5.4: The properties of a 2FES-3Y-40S compressor [9].

Property	Value	Unit
Number of cylinders (nr)	2	[-]
Bore (B)	46	[mm]
Stroke (l)	33	[mm]

The power consumption of the compressor is described by the volumetric and isentropic efficiency. Both the volumetric and isentropic efficiencies are a function of the pressure ratio and the inlet temperature. The volumetric and isentropic efficiency are obtained from a reference model published by the manufacturer [9]. The data of this model is analyzed according to the method described by Shi [57].
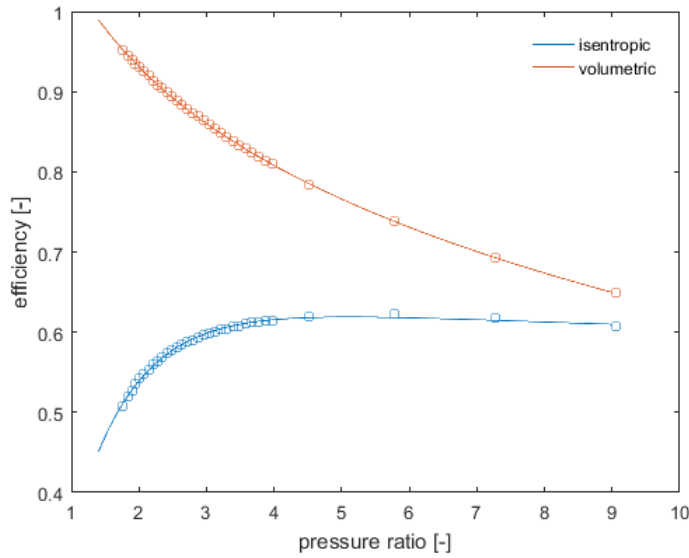

Figure 5.7: The volumetric and isentropic efficiency of the compressor for an evaporating temperature of 273.15 K and a superheating of 5 K. The squares indicate the data point points obtained from the reference model of the manufacturer.

Figure 5.7 shows the isentropic and volumetric efficiency of the compressor based on the data obtained from the reference model. It is assumed that the isentropic and volumetric efficiency are only a function of the pressure ratio. Therefore the influence of the suction pressure or the superheating at the inlet of the compressor is neglected. During normal operation the inlet conditions be almost constant so this will not have large impact on the overall performance of the unit. Meanwhile the pressure ratio varies over time since it is dependent on the outside temperature.

The volume flow of the compressor can directly be determined if the rotational speed and the pressure ratio of the compressor is known:

$$\dot{V} = \eta_{vol}\left(nr\pi\frac{B^2}{4}lN\right) \tag{5.33}$$

The enthalpy at the outlet of the compressor can be calculated using the isentropic efficiency:

$$h_{out} = \frac{h_{out,s}-h_{in}}{\eta_s} + h_{in} \tag{5.34}$$

The electric power consumption can be determined with the mechanical efficiency of the compressor:

$$\eta_{mech} = \frac{\dot{m}_r(h_{out}-h_{in})}{P_{elec}} \tag{5.35}$$

The mechanical efficiency is estimated as 0.9670 based on the data obtained from model of manufacturer. The pressure ratio has only a very small influence on the mechanical efficiency so therefore it can that the mechanical efficiency remains constant.

Table 5.5: The properties of a LH44E/2FES-3Y condensing unit [10] at full capacity.

Property	Value	Unit
Air flow rate	2000	[m^3/hr]
Number of fans	1	[-]
Power consumption of the fan	155	[W]

5.5. CONDENSER

As mentioned earlier the system uses a LH44E/2FES-3Y condensing unit. Bitzer also provides a reference model for this condensing unit [10]. This model specifies among other things the energetic performance of the unit. Other specification obtained from this model are included in table 5.5.

The manufacturer does not specify the dimension of the equipment such as the number of tubes, the tube length or the tube diameter. Therefore it is almost impossible to make an accurate theoretical description of the heat transfer in the equipment. However, the thermal properties included in the model provided by the manufacturer can be used to find an expression for the overall heat transfer coefficient. The reference model is used to determine the heat transfer rate under varying operating conditions. These results are analyzed and the overall heat transfer coefficient for each situation. Based on these results the following correlation for the overall heat transfer coefficient is found:

$$UA = -13.14 \left(\frac{P_{cond}}{P_{evap}} \right)^2 + 146.5 \left(\frac{P_{cond}}{P_{evap}} \right) + 324.8 \tag{5.36}$$

This relation has been obtained by relating the logarithmic mean temperature difference to the capacity of the condenser. The logarithmic temperature difference has been determined using the condensation temperature and the temperature of the air entering and leaving the condenser. It is valid for the complete range of refrigerant mass flow encountered within the condensation unit. It is a function of the pressure ratio since in this way it accounts for the higher superheating encountered for higher pressure ratios.

In the model the capacity of the compressor can be directly related to the power consumption of the compressor and the capacity of the generator. The only unknown is the desired condensation temperature. The condensation temperature must be high enough to facilitate the desired heat transfer.Since the overall heat transfer coefficient is known, the number of transfer units can be used to determine this temperature.

5.6. STORAGE TANK

The pilot plant uses a 300 liter storage tank in order to store the produced CHS before it is utilized. The crystals have a higher density than the solution, so the crystals settle at the bottom of the tank. A model has been developed in order to describe the settling of the crystals in the tank. This model is inspired by the model of Flick et al. [24] and Douzet et al. [21]. However, unlike the other models it neglects the diffusion since this is a very slow process and it includes the possibility to describe the presence of superheated solution. A detailed description of the extended storage model can be found in appendix D.

Simulations are performed with this extended model in order to gain some insight into the performance of the model. Furthermore, the model has been used to gain some insight into the phenomena occurring in the storage tank. Based on the simulation result the following observations are made:

- The mass flows entering and leaving the tank will pose a limit on the time step. Mass flows in the range of 0.5 to 0.7 kg/s are expected to be encountered in the system. This means that time step should be reduced to somewhere between 1 and 10 seconds in order to maintain a good accuracy.

- At least six to eight volume elements are required in order to provide an accurate description of the crystal distribution. However, the simulations described in appendix D show that the accuracy can be significantly improved if the number of control volumes is increased from 8 to 20. However, this will also limit the time step.

- The dynamic effects described in the storage tank are mainly important during the start up of the system. When the system is off the crystals accumulate in the bottom of the tank resulting in a very dense slurry with a high mass fraction. Due to the high crystal concentration this slurry is very difficult to transport and might increase the danger of blockages. However, these effects are very dynamic and cannot be described by the model without using a very small time step. Furthermore, these dynamic effects are also very dependent on the thermal mass of the systems and this is neglected anyways.

Table 5.6: The parameters of the storage model

Property	Value	Unit
Height tank	0.7	[m]
Diameter tank	0.9	[m]
Thickness insulation	13	[mm]
Thermal conductivity	0.033	[W/(m K)]

• The settling of the crystals in the storage tank is dependent on the size of the crystals. However the actual size and shape of the crystals is not known. This makes it very difficult to accurately predict actual settling of the crystals. These parameters are therefore estimated based on earlier research, however it is not possible to validate these assumptions.

Based on these observations is is concluded that it is better to not use the extended model. Although, the extended model provides some valuable insight in the behavior of the tank it is not practical to integrate it in the model of the system. It will slow down the calculations and make the modeling method of other components much more complicated. Furthermore, this model will provide much more detail than necessary. Therefore, a lumped model will be used instead. Table 5.6 includes some of the parameters of the actual storage tank. The tank is insulated with 13 mm thick Armaflex foam with a thermal conductivity of 0.033 W/(m K).

5.7. CONCLUSION
This chapter provides an overview of the relations and equations used in the model. For each component the modeling approach is presented. The models of the components are implemented into Matlab. Furthermore, the correlations of the fluid properties are also included in the model. All these equations and correlations are solved iteratively for each time step.

6

VALIDATION OF THE MODEL

The model described in chapter 5 has been validated using experimental data obtained from the pilot system located in Twello. The measurements are used to select the most suitable correlations and to determine the strengths and weaknesses of the model. So far, the system has only been in operation using water instead of the TBAB solution. Therefore the model has been slightly modified in such a way that the properties of the fluid are obtained with Fluidprop rather than the correlations described in chapter 3. The available experimental data is limited to the measurements executed at 4 and 5 October 2016. An overview of the sensors and their accuracy can be found in appendix E. Unfortunately some of the experimental data (including the power measurements) did not provide a reasonable result. Therefore the validation can still be improved by redoing some of the measurements.

6.1. AIR COOLER
The water and air temperatures at the inlet and outlet of the air cooler are shown in figure 6.1. From this data and the water flow rate it is easy to determine the capacity of the air cooler. However the experimental data of the air flow is inconclusive since:

- As shown in figure 6.1 the air outlet temperature approaches (and is sometimes even lower than) the water inlet temperature. Since the heat exchanger is placed in co current position the air should always be warmer than the water outlet temperature, so this must be the result of inaccurate measurements. Both sensors measuring the water temperature are in agreement with each other so its probably due to the measurements. It could be that the sensor is not properly calibrated or that the measurements are affected by the temperature of the duct.

- The air mass flow rate has been estimated using an energy balance. This balance does not include the effects of the condensation of the water since the humidity of the air is not known. Furthermore the amount of condensation is difficult to predict since it dependent on the local air temperature and the temperature of the surface of the tubes and the fins.

- It is assumed that the air at the inlet of the air cooler is at the same temperature as the room. This assumption is incorrect and an additional temperature sensor will be placed in order to determine the actual temperature. This assumptions has a consequence that the calculated air mass flow rate varies between the 0.3 and 0.6 kg/s. However the fan in the air duct is not speed controlled so a more constant air flow rate is expected.

The air mass flow is used to estimate the capacity of the air cooler using several different correlations. For these calculations the flow rate as well as the inlet temperature of the air and the water are used as input. The result of these calculations is shown in figure 6.2. The overall heat transfer coefficient presented in this figure is determined using the internal tube area as heat transfer area.

The capacity of the air cooler is always very well predicted by the correlations. This is because the capacity is limited by the flow rates and not by the heat transfer mechanism. Between 20:00 and 21:00 hour the measured overall heat transfer exceeds the prediction of all three correlations. However as shown in figure 6.1 at
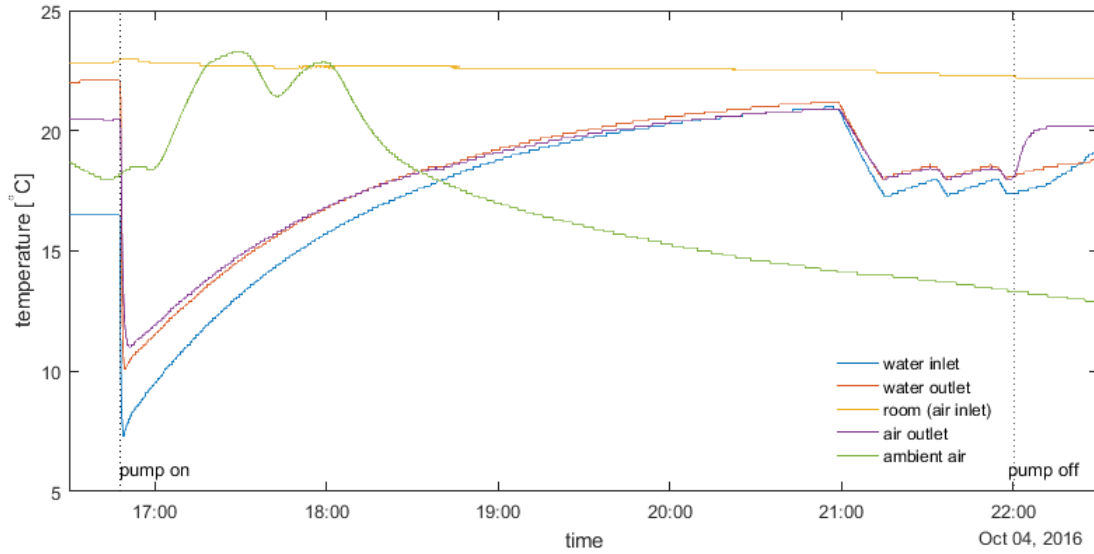
Figure 6.1: The measured temperature of the water entering and leaving the air cooler as well as the temperature of the air.
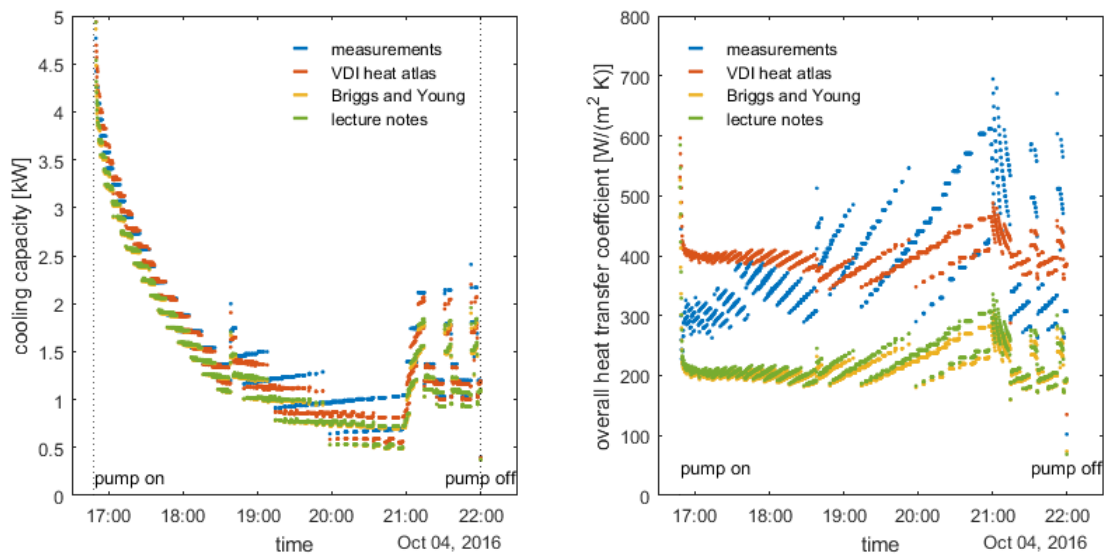

Figure 6.2: Capacity and the overall heat transfer coeffcient of the air cooler. The experimetal data are compared with the correlations of Briggs and Young [11], VDI heat atlas [67] and the correlation fromt he course refrigeration technology and applications [30]. The overall heat transfer coefficient is calculated using the internal are of the tubes.

the same time the temperature difference between the air outlet and the water flow is unreasonable small so the experimental data may not provide an accurate estimation.

The relation between the air and the water flow and the overall heat transfer coefficient is shown in figure 6.3. Just as expected the water flow has a positive effect on the heat transfer although the trend is slightly troubled due to the influence of the air flow rate. The results obtained for a high air mass flow rates (> 0.5 kg/s) are mostly obtained between 20:00 and 21:00 hour. As explained earlier these measurements most likely do not provide the most accurate results. Based on this figure it seems that the VDI heat atlas [67] provides the most accurate result. However the actual air inlet temperature should still be measured so that a better prediction can be made.
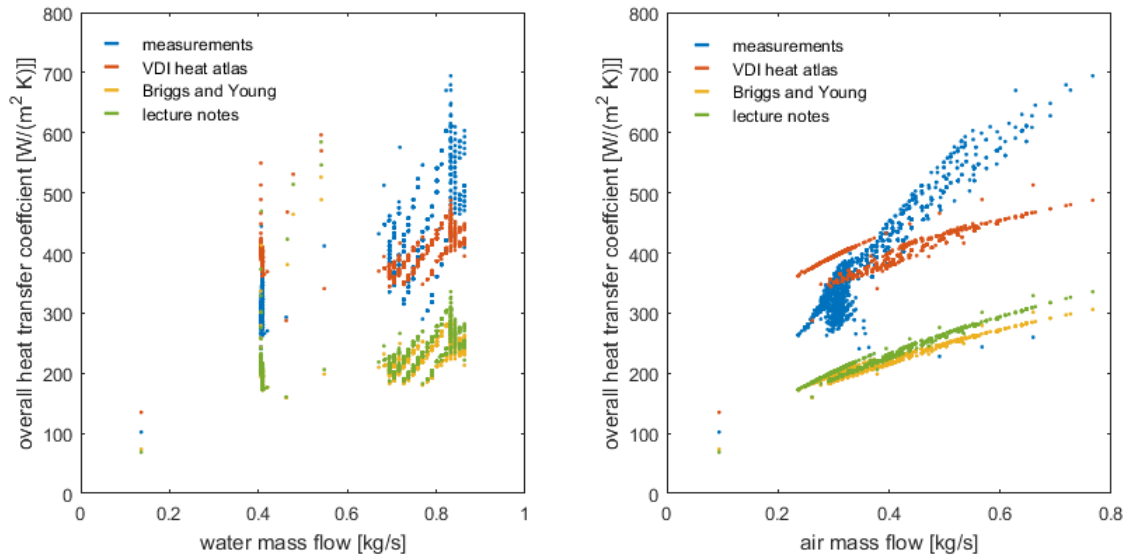
Figure 6.3: Overall heat transfer of the air cooler plotted against the water mass flow rate on the left and the air flow rate on the right.

6.2. Generator

The generator consists out of a plate heat exchanger in which the refrigerant is evaporated. The temperature and the pressure of both the water and the refrigerant are measured at the inlet and at the outlet of the generator. Therefore the capacity of the generator can be easily estimated using an energy balance of the flows.

$$\dot{Q} = \dot{m}\Delta h \tag{6.1}$$

This energy balance is solved for both the refrigerant and the water side of the system. However as shown in figure 6.4 the heat flow resulting from these energy balances are not necessarily the same. This is probably the result of the following phenomena:

- The temperature of the plate heat exchanger is initially at a much higher temperature then the refrigerant. Therefore a part of the energy transferred from the refrigerant is absorbed by the thermal mass of the generator and therefore not transferred to the water side. The same phenomenon happens just after the moment that the pump is switched on.

- The heat transfer in the generator side is calculated using the assumption that enthalpy measured at the outlet of the condenser is the same as the enthalpy at the inlet of the generator. This is only true for a complete adiabatic process. However in the pipes some losses are expected to occur due to heat transfer to the environment.

Based on these observations it is concluded that the experimental data on the water side provides a more accurate estimation of the heat transfer. Therefore, this capacity will be used when validating the heat transfer coefficients in the plate heat exchanger.

The superheating of the refrigerant is controlled by a valve. This valve regulates the refrigerant flow rate so that the desired superheating of 3 K is reached. However, as shown in the graph on the left in figure 6.5, the actual superheating varies between the 6 and 9 K. The valve however is always completely open as shown in at the right side of figure 6.5. This means that the valve cannot let enough refrigerant pass in order to maintain the desired superheating.

The valve can be replaced by another valve which would allow higher mass flows. However, this might not be sufficient since the refrigerant flow is under these operation conditions still limited to approximately 0.045 kg/s by to the compressor [9]. Ideally this should be solved by regulating the evaporation pressure although this would require an additional controller. A higher evaporation pressure reduces the temperature difference in the evaporator and therefore the capacity. At smaller capacities the control works fine since smaller refrigerant flows are required. Controlling the evaporation pressure is also beneficial since it can also be used the prevent too quick crystallization in the TBAB system.
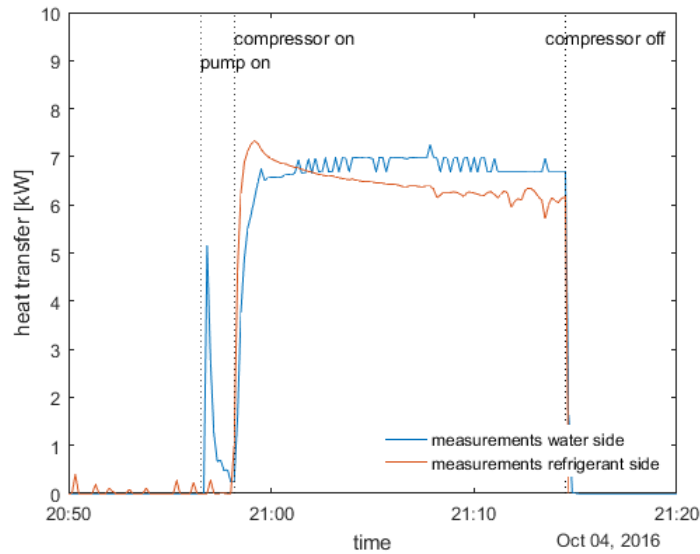
Figure 6.4: The heat transfer in the generator estimated using the experimental data of the water flow (blue) and the experimental data of the refrigerant flow (red).
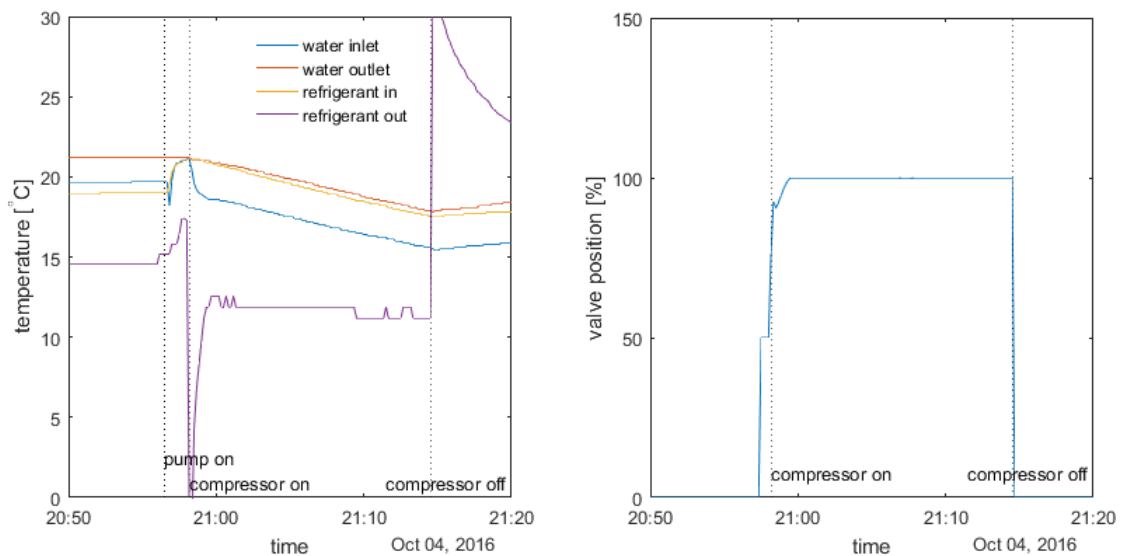

Figure 6.5: Left; the temperature at the inlet and the outlet of the generator; right the position of the valve that regulates the refrigerant flow rate.

HEAT TRANSFER CORRELATIONS

The refrigerant is first evaporated and then superheated within the generator. Therefore it is possible to divide the heat exchanger into two seperature zones; the evaporating zone and the superheating zone. For each zone the logarithmic mean temperature difference and the heat transfer can easily be calculated using the saturation conditions of the fluid. A correlation for a single phase heat transfer is sufficient for the water side and for the superheating zone. Using such a correlation it is possible to estimate the evaporation convective heat transfer coefficient from the measurements. Two equations for the single phase heat transfer have been selected; one which provides a low and one which provides a high estimation of the Nusselt number. The first equations is that of Thonon et al. [65]. This equation is developed for a range of different plate heat exchangers and different refrigerants. For a chevron angle of 60 ° they proposed the following correlation:

$$Nu = 0.2267 Re^{0.687} Pr^{1/3}$$

(6.2)

The second correlation is the result of a comprehensive study to different plate heat exchangers of Yang et al. [73]:

$$Nu = \left(-1.342 \times 10^{-4}\beta^2 + 1.808 \times 10^{-2}\beta - 0.0075\right)$$
$$Re^{-7.956 \times 10^{-5}\beta^2 + 9.687 \times 10^{-3}\beta + 0.3155}Re^{\Phi/\beta}Re^{\gamma/\Phi}Pr^{1/3} \tag{6.3}$$

In this equation is Φ the surface enlargement factor, β the chevron angle and γ the corrugation profile aspect ratio which is assumed to be 0.6 for this specific plate heat exchanger. In this study the hydraulic diameter has been defined as $2b$ and it makes use of the projected area instead of the actual heat transfer area. However this equation can be modified in order to be used with the hydraulic diameter and heat transfer as defined earlier. In that case the correlation should be multiplied with a correction factor:

$$\text{correction} = \Phi^{2 - \left(-7.956 \times 10^{-5}\beta^2 + 9.687 \times 10^{-3}\beta + 0.3155 + \Phi/\beta + \gamma/\Phi\right)} \tag{6.4}$$

For this specific heat exchanger these expression can be simplified to:

$$Nu = 0.788Re^{0.637}Pr^{1/3} \tag{6.5}$$

The different correlations have been used to determine the convective heat transfer coefficient from the measurements. A comparison between the correlations and measurements is shown in figure 6.6. The correlation of Cooper [41] seems to provide the best results in this specific situation, however this correlation does not have any dependence of the refrigerant flow rate. Furthermore, this correlation requires an estiamtion of the a roughness of the plate without having any good data to validate this assumption. The correlation of Amalfi et al. [2] also provides a reasonable result without having these problems. The only other correlation that gives an even better result is the extrapolated relation of Palmer et al. [55]. This correlation however is extrapolated far outside its application boundaries and it is intended for different refrigerants with a different lubrication so this equation cannot really be used.
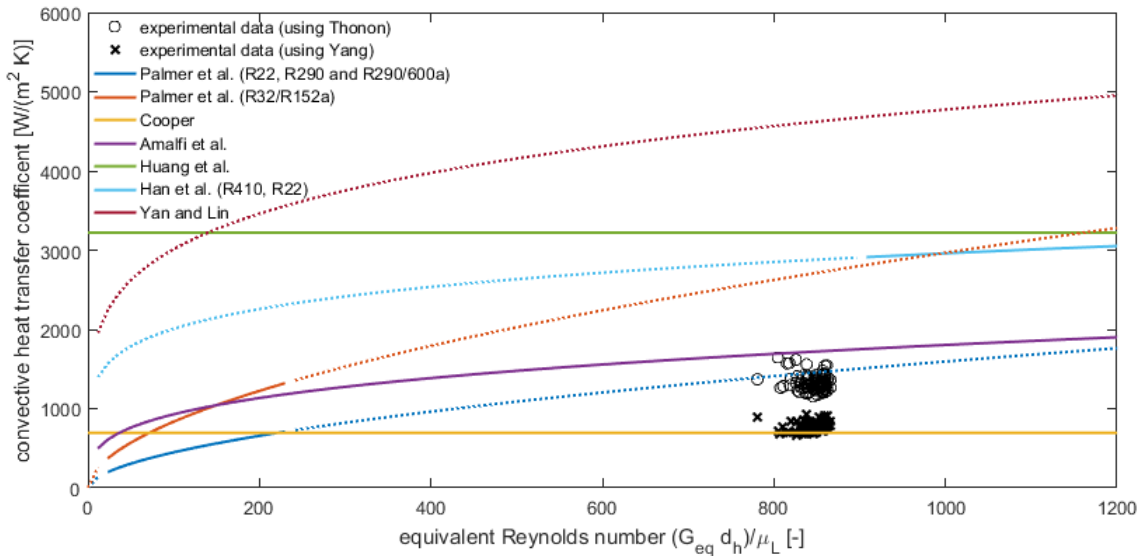

Figure 6.6: Comparison between the experimental convective heat transfer coefficient and several Nusselt number correlations for evaporation within a plate heat exchanger [2, 27, 29, 41, 55, 72]. The dotted lines represent the extrapolation of the correlations outside of their given domains. The equivalent Reynolds number is defined using equation 4.19.

The correlation of Thonon and the correlation of Amalfi et al. are selected and implemented in the model as described in chapter 5. The model calculates the temperature as function of the position along the plates. A comparison between the results of the model and the experimental data is presented in table 6.1. The model overestimate the heat transfer but the error seems to be less then 15 % under these conditions.

PRESSURE DROP CORRELATIONS

The pressure drop in the generator is also included in the model. The pressure drop on the refrigerant side has been measured as shown in figure 6.7. This pressure drop is calculated using several different correlations.

Table 6.1: Validation of the generator model.

time	fluid	$\dot{m}$ [kg/s]	T_{in} [°C]	T_{out} [°C]	$\dot{Q}_{data}$ [kW]	$\dot{Q}_{model}$ [kW]
21:10:00	R134a	0.05	11.2	18.5	7.0	7.64
	water	0.7	18.8	16.4		
21:14:00	R134a	0.04	11.1	17.6	6.7	7.44
	water	0.7	18.0	15.7		
21:35:00	R134a	0.04	11.9	17.8	7.5	7.88
	water	0.7	18.0	15.8		

For these calculations the pressure drop in the superheating zone is neglected and average properties have been used. For this study the generator total pressure drop is defined as:

$$\Delta p = \Delta p_f + \Delta p_{pt} + \Delta p_a \tag{6.6}$$

If the study does not define the pressure drop then some common correlations can be used [29]. These correlation define the pressure drop in the ports as:

$$\Delta p_{pt} = 0.75 \left(\frac{G_{pt,in}^2}{2\rho_L} + \frac{G_{pt,out}^2}{2\rho_G} \right) \tag{6.7}$$

And the pressure due to acceleration is equal to:

$$\Delta p_a = G^2 (X_{out} - X_{in}) \left(1/\rho_G - 1/\rho_L \right) \tag{6.8}$$

A comparison between the correlations and the measurements is shown in figure 6.7. From the figure it is clear that the precision of the measurements is too low in order make an accurate validation of the correlations. The measured pressure drop is usually 0.1 bar even when there is no or a very small flow rate. So there is probably a constant error in the measurements; this can be the result a difference in the static pressure. At higher flow rates the pressure drop is varying between the 0.1 and 0.2 bar. Considering the constant error the actual pressure drop in the generator is somewhere in the range 0 to 0.1 bar depending on the flow rate. This means that the correlation of either Amalfi et al. [2] or Huang et al. [29] should be used. These correlation do give a lower estimation of the pressure drop. This is no surprise since the calculations neglect the pressure drop in the tubes and the superheating zone. For this model the correlation of Amalfi et al. is preferred since the same study is already selected to predict the Nusselt number.
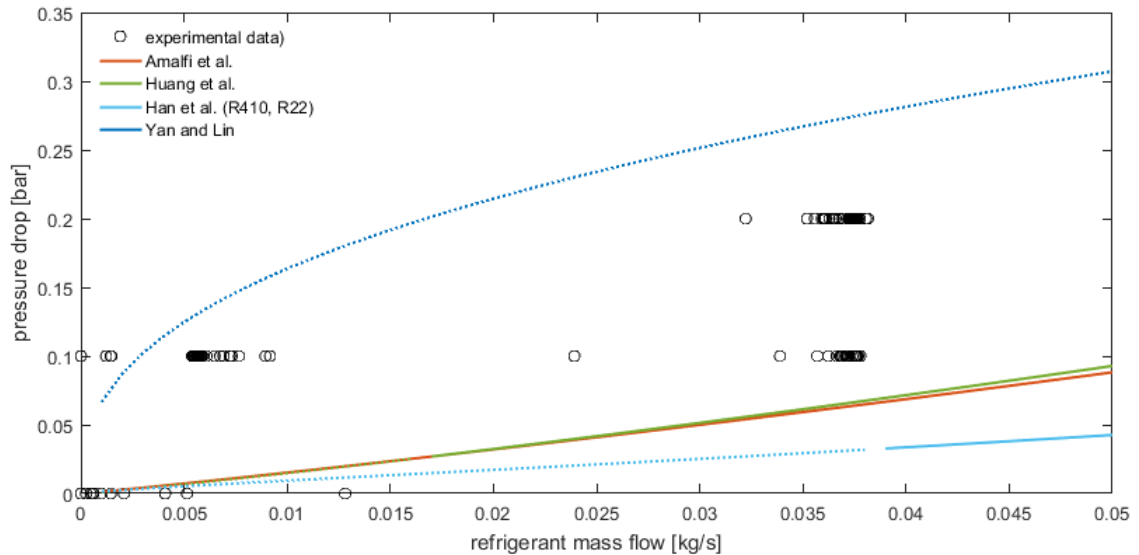

Figure 6.7: Comparison between the measured pressure drop and several pressure drop correlation for evaporation within a plate heat exchanger [2, 27, 29, 72]. The dotted lines represent the extrapolation of the correlations outside of their given domains.

6.3. COMPRESSOR

The power consumption of the compressor has been measured although the experimental data does not provide a reasonable result. Therefore the power consumption has been estimated using an energy balance:

$$P = \frac{\dot{m}\Delta h}{\eta_{mech}}$$ (6.9)

In this equation is the mechanical efficiency (η_m which is equal to 0.9670) used to correct for the energy losses not related to the flow such as the energy loss of the electric motor. The estimated power consumption is compared with the model of the compressor in figure 6.8. During the first two minutes the measurements estimate a negative power consumption. This is off course incorrect and this can be attributed to the thermal mass of the system. After a few minutes the measured power consumption is almost stable but it is still almost twice as small as the modeled power consumption. This is because the actual power consumption cannot be accurately estimated using equation 6.9. The temperatures are not measured directly at the inlet and the outlet of the compressor. As a result energy has been transferred to the environment resulting in an under estimation of the power consumption.
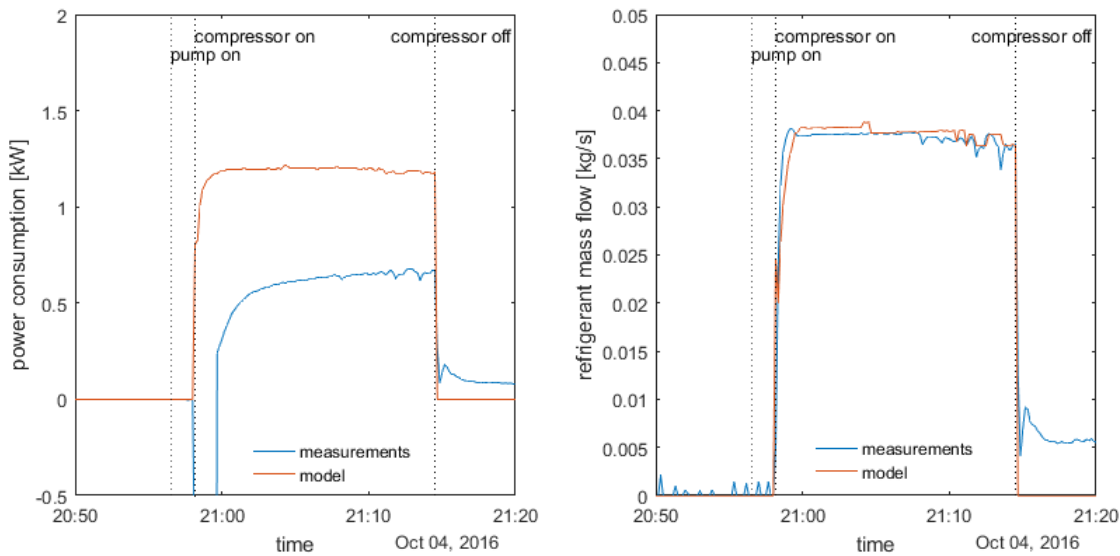

Figure 6.8: Left: comparisons between the measured and modeled power consumption compressor; right: comparison between the measured and modeled refrigerant mass flow rate.

Based on the experimental data there is no reason to believe that the model provides an inaccurate result. The compressor model is in good agreement with the model of Bitzer [9] and the differences between the model and experimental data can be attributed to energy flows and losses within the actual system. However the model be should reevaluated as soon as better experimental data are available. A comparison between the measured and modeled refrigerant flow rate is also presented in figure 6.8. The deviation between the flows are within the accuracy of the sensors. Therefore it can be concluded that the volumetric efficiency has been well predicted by the model under these conditions.

6.4. CONDENSER

In the condenser the superheated refrigerant is completely condensed. Ideally the pressure ratio in the condenser should be controlled based an the capacity and the ambient air temperature. The difference in the condensation temperature and the ambient air must be sufficient to facilitate the desired heat transfer. In figure 6.9 a comparison between the modeled and experimental condensation pressure is presented. In the first situation the modeled and measured condensation pressure are close to each other. The actual system seems to operate at a constant condensation pressure while the model is much more dependent on fluctuations of the ambient air temperature. In the second situation the ambient temperature is about 2 K lower. Nevertheless the experimental data shows that system continues to operate at the same condensation pressure. This is probably due to the control parameters. This means that the control strategy should still be modified in order to fully profit from the lower ambient air temperature.
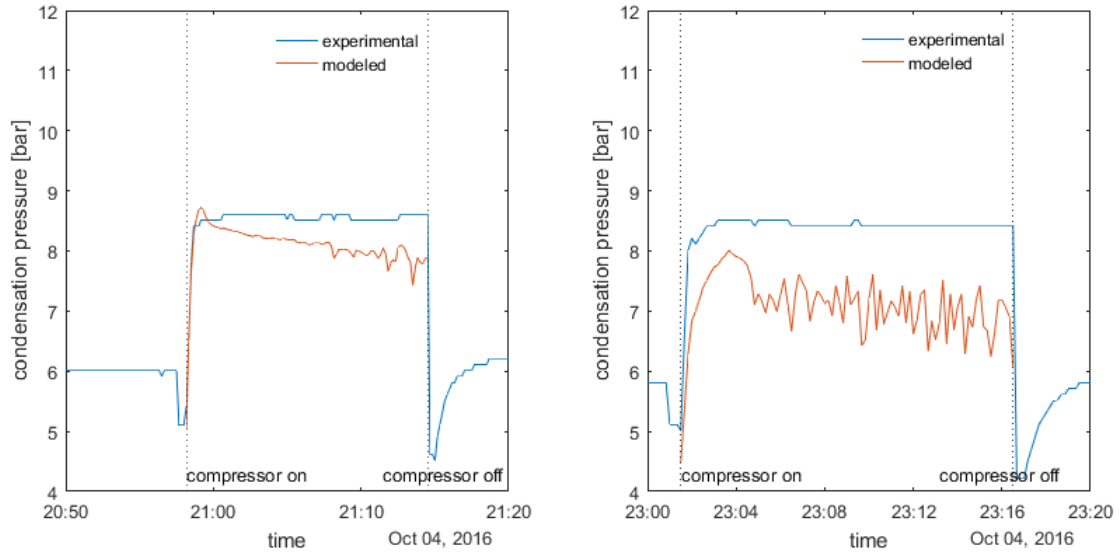
Figure 6.9: Condensation pressure (at the outlet of the condenser) according to the experimental data and the measurements. The outside temperature in the first situation is 14 °C and in the second situation 12 °C.

The observed pressure at the in- and outlet of the condenser is shown in figure 6.10. In the model the pressure drop in the condenser is neglected since too little data is available to make an accurate prediction of this pressure drop. However the measurements find an almost constant pressure drop of approximately 0.8 bar. It is unknown whether this pressure drop is the same under other operation conditions. Based on dimensionless analysis we known that the pressure drop scales quadratically with the mass flow rate. So therefore the following relation for the pressure drop could be obtained from the measurements:

$$\Delta p = 7.122 \times 10^4 \left(\frac{m_r}{0.0361} \right)^2 \tag{6.10}$$
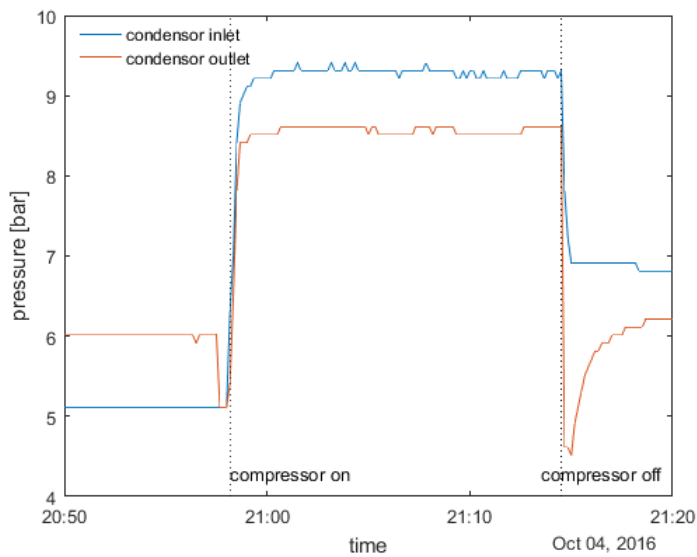

Figure 6.10: Pressure at the inlet and the outlet of the condenser.

6.5. PUMP

The pumps in the system are modeled using the pump characteristic. As mentioned earlier the power consumption is not accurately measured in the system. The experimental data always measure a pressure drop of 0.1 or 0.2 bar. These measurements are probably incorrect, so it is impossible to validate the pump characteristic using the experimental data. Nevertheless the model can still be used to calculate the flow rate and the pressure drop for a given pump frequency. The results for the air cooler side of the system are shown in table 6.2. The mass flow is accurately predicted by the model, while it is immediately clear that the either the pump characteristic or the pressure drop measurements are incorrect.

Table 6.2: A comparison of the performance of the air cooler pump.

time	frequency [%]	Δp data [bar]	Δp model [bar]	$\dot{m}$ data [kg/s]	$\dot{m}$ model [kg/s]
17:35:00	0.40	0.1	0.15	0.41	0.41
19:30:00	0.72	0.1	0.42	0.75	0.71
20:00:00	0.75	0.1	0.45	0.78	0.78
20:30:00	0.77	0.1	0.47	0.80	0.81

The result for the generating side of the system are presented in table 6.3. The correlation of Ma and Zhang [42] is selected to describe the friction factor in the plate heat exchanger. This correlation seems to provide the best result compared with the modeled pump characteristic. Furthermore, it has as advantage that it has been developed to describe TBAB CHS. Still the mass flow is overestimated by the model; this is most likely due to an underestimation of the pressure drop. However it also possible that this is due to deviations of the modeled pump characteristic. Therefore it is important to assess the performance of the sensor in order to see if the deviation is indeed the result of inaccurate measurements and not due to the pump characteristic.

Table 6.3: A comparison of the performance of the generator pump.

time	frequency [%]	Δp data [bar]	Δp model [bar]	$\dot{m}$ data [kg/s]	$\dot{m}$ model [kg/s]
21:00:00	0.59	0.2	0.81	0.68	0.83
23:00:20	0.41	0.1	0.42	0.46	0.57
23:01:00	0.50	0.1	0.60	0.57	0.70
23:15:00	0.60	0.2	0.85	0.69	0.84

6.6. CONCLUSION

The model of the air conditioning system has been validated with experimental data of the pilot system in Twello operating with water instead of a TBAB solution. Each component is validated separately:

- The experimental data of the air cooler are unsufficent to make and accurate validation of the correlation. This will be solved by installing an additional temperature sensor. For the model however it seems that the capacity of the air cooler is well described by the model using the correlation of the VDI heat atlas [67].

- The pressure drop and heat transfer in the generator have been compared with several correlations. It is concluded that the correlation of Amalfi et al. [2] provides an accurate estimation of the evaporation side when it is combined with the correlation of Thonon et al. [65] for the single phase flow. During the measurements it was also observed that the super heating was much too high. This should be solved by changing the valve or adding a control for the evaporation pressure.

- The compressor model accurately predicts the refrigerant mass flow. The power consumption of the compressor was estimated using the measured enthalpy. However, the model predicts a much larger power consumption than the measurements. This differences can be attributed to the thermal mass of the system and to energy losses to the environment.

- The measured condensation pressure is almost constant while the model predicts a lower condensation pressure for lower ambient temperatures or capacities. This might indicate that the system might not be optimally controlled. For the pressure drop in the condenser a correlation is proposed based the experimental data.

- Both pumps have been validated using the frequency of the pump as an input. The model and the pump characteristics indicate that the pressure drop measurements are incorrect. On the air cooler side of the system the pressure drop and mass flow rate seem to be accurately described by the model. On the generator side the pressure drop is most likely slightly underestimated although it is not possible to rule out the possibility that it is due to deviations in the modeled pump characteristic.

7

OPTIMIZATION AND EVALUATION OF THE TBAB SYSTEM

The model presented in the previous chapters will be used to evaluate the performance of the system. However, the performance of such a system is heavily dependent on the chosen control parameters. In this chapter the optimization of these parameters is presented. Keep in mind that the model has not yet been validated for TBAB system so the optimal mass flows might not necessarily be the same for the actual system.

7.1. OPTIMIZATION OF THE FLOW RATE IN THE AIR COOLER

In this system the pumps are frequency controlled so the the flow rate in the air cooler can be controlled in order to meet the optimal operating conditions. The optimal operating conditions are a trade off. On the one hand a high velocity is preferred since it will result in a higher overall heat transfer and capacity of the air cooler, however on the other hand, it will also lead to a higher pressure drop. Therefore, several simulations are performed in which the mass flow rate of the slurry is varied. For these simulations the air at the inlet of the air cooler is kept at a constant temperature of 23 °C while the air mass flow was kept constant at 0.4 kg/s.
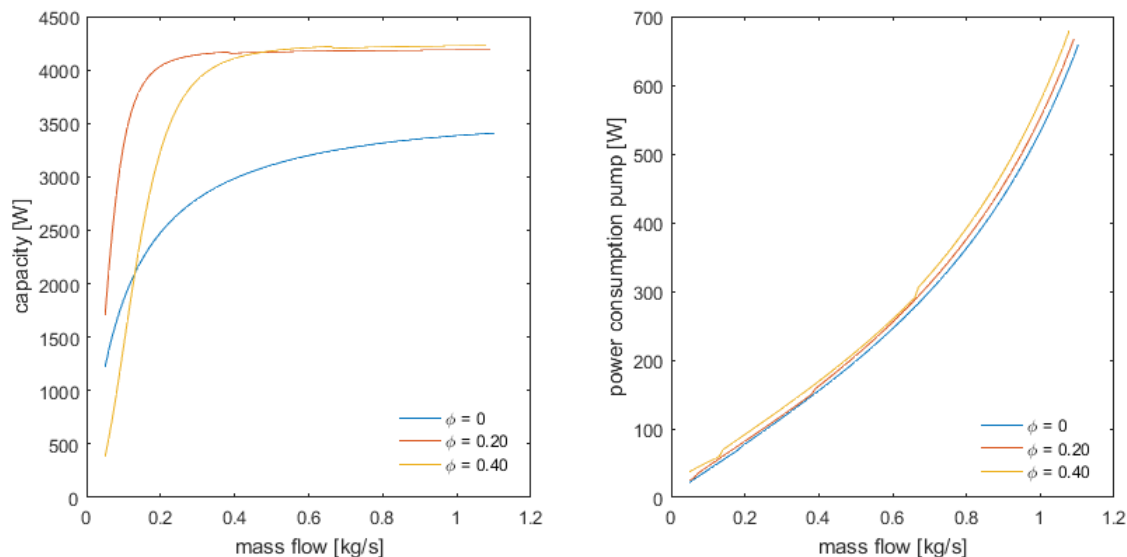
Figure 7.1: The cooling in the air cooler and the power consumption of the pump for a constant mass flow of the air of 0.4 kg/s. The TBAB solution at the inlet is at the crystallization temperature except for the solution at $\phi_c = 0$; this solution is superheated by 1 K.

The result of the simulations is shown in figure 7.1. The capacity of the air cooler increases with the mass flow rate. This is due to the enhanced convection due to the higher velocity. For a slurry with a solid fraction of

0.20 and 0.40 it is observed that at a certain point increasing mass flow will not increase the capacity anymore. At this point the capacity of the air cooler it is purely limited by the temperature difference between the slurry and the air. This means that the capacity of the air cooler will mainly depend on the temperature difference between the air and the slurry. The slurry usually has an almost constant temperature profile, so the capacity can best be controlled by regulating the air flow rate.

Figure 7.1 shows that the power consumption of the pump is mainly dependent on the flow rate and not so much on the solid fraction. Still crystal mass fractions above the 40 wt% should be avoided since they are associated with a sudden increase in the pressure drop [80]. The presented result are used to determine the optimal mass flow rate of the solution. Ideally the capacity of the air cooler should be as large as possible while the power consumption is minimized. It is assumed that the fan is not used for ventilation so in other words the fan is only in operation when there is a cooling demand. When there is a cooling demand the air cooler extract a certain amount of energy from the air in a given period of time. At the same time the system consumes energy so it is desired to maximize the ratio between these energy flows:

$$\text{ratio} = \frac{E_{cooling}}{P_{consumption}\Delta t} = \frac{\dot{Q}_{cooling}\Delta t}{(P_{pump}+P_{fan})\Delta t} = \frac{\dot{Q}_{cooling}}{P_{pump}+P_{fan}} \tag{7.1}$$

According to the simulations the power consumption of the fan is only about 34 W due to the low pressure drop in air ducts. However, the pressure drop in the air ducts might be much higher due to for example filters or bends that are not included in the model. The ratio between the energy flows has been determined using the same operation conditions as before. The result is shown in figure 7.2. Every curve has a clear optimum which is dependent on the solid fraction. The curves also include a small discontinuities; this is due to the transitions from laminar to turbulent flow.
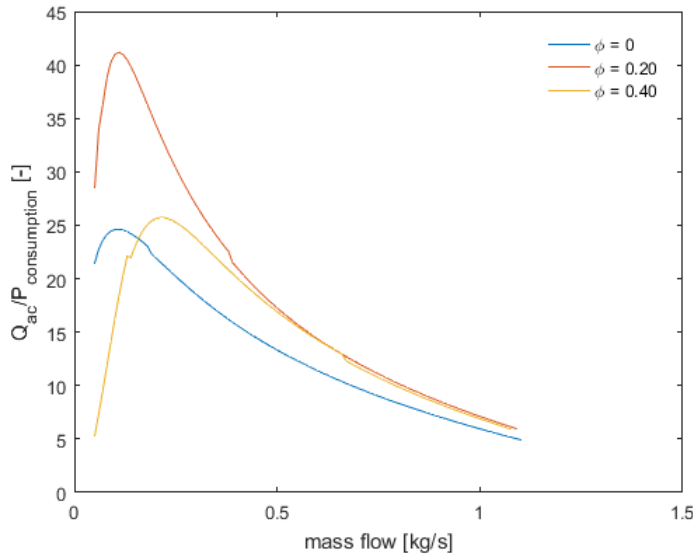

Figure 7.2: Ratio between the cooling capacity and the power consumption of the pump and the air fan for a constant air mass flow rate of 0.4 kg/s. The TBAB solution at the inlet is at the crystallization temperature except for the solution at $\phi_c = 0$; this solution is superheated by 1 K.

The influence of the air mass flow rate has also been investigated. Table 7.1 provides an overview of the optimum mass flow for a number of different operation conditions. It is clear that the optimum flow rate and the capacity of the air cooler increases with the air flow rate. Interestingly, the ratio between the power consumption and the capacity of the air cooler seems to be lower for a solid fraction of 0.40. This could be explained by a reduction in the convective heat transfer of the slurry. This might be the result of re-laminarization; the Reynolds number of the slurry is lower for a solid fraction of 0.40 than for a solid fraction of 0.20.

7.2. Optimization of the flow rate in the generator

The mass flow in the generator side is also optimized in order to minimize to power consumption of the system. In this case the flow rate of the slurry is varied while the suction pressure is maintained at 3.8 bar. The

Table 7.1: The optimum mass flow in the air cooler for certain operation conditions. The TBAB solution at the inlet of the air cooler is at the crystallization temperature except for the solution at $\phi_c = 0$; this solution is superheated by 1 K.

ϕ_{in} [-]	m_{air} [kg/s]	$\dot{m}_{opt}$ [kg/s]	capacity [W]	ratio [-]
	0.10	0.05	620.4	27.5
0	0.30	0.06	1230	30.0
	0.50	0.16	2601	14.6
	0.10	0.05	895.2	34.1
0.20	0.30	0.09	2580	44.6
	0.50	0.14	4490	24.0
	0.10	0.12	935.6	12.7
0.40	0.20	0.18	2525	12.4
	0.30	0.25	4307	6.88

ambient air temperature is varied between the 10 and 30 °C. The results of these simulations are presented in figure 7.3. The first graph shows that the capacity of the generator increases with the flow rate. As a result the refrigerant mass flow is also higher resulting in a higher power consumption of the condensing unit (which consist out of the compressor and the condenser). Unsurprisingly the ambient air temperature has a considerable influence on the power consumption of the condensing unit while having very little influence on the capacity of the generator.
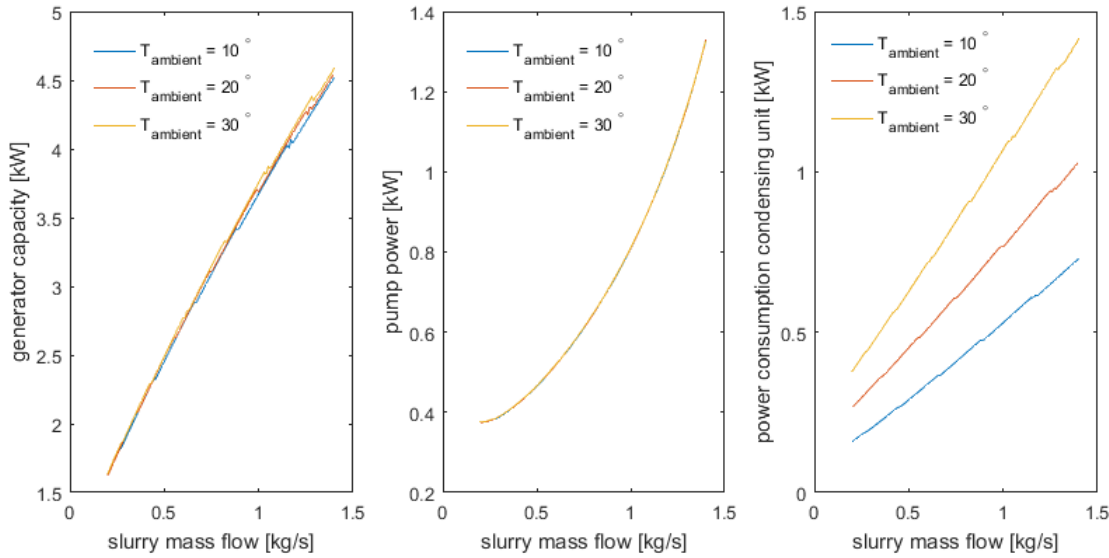

Figure 7.3: The capacity of the generator, the power consumption of the pump and the power consumption of the condensing unit for a constant compressor suction pressure of 3.8 bar.

The power consumption of the pump also increases with the flow rate. The power consumption is minimal for a mass flow rate of about 0.2 kg/s. However, this does not mean that low flow rates are preferable. On the contrary, due to the pump characteristic the low flow rates are associated with a very low pump efficiency. For these simulation the efficiency of the pump varies from 1.5 % (at 0.1 kg/s) to 24 % (at 1.4 kg/s).

The power consumption of the pump and the capacity of the generator are used to determine the optimum mass flow of the slurry. The solution is first heated up in the pump before it enters the generator where it is cooled down. So the total amount of cold produced in the system can be expressed as:

$$\dot{Q}_{cold} = \dot{Q}_{gen} - P_{pump} \qquad (7.2)$$

The power consumption should be minimized so the following ratio should be maximized:

$$\text{ratio} = \frac{\dot{Q}_{gen} - P_{pump}}{P_{pump} + P_{comp} + P_{fan}} \qquad (7.3)$$

This ratio is plotted against the mass flow in figure 7.4. The optimum mass flow is about 0.4 kg/s with a ratio ranging from 1.7 to 2.6 depending on the ambient air temperature. However the ambient air temperature seems to have almost no influence on the optimal mass flow rate.
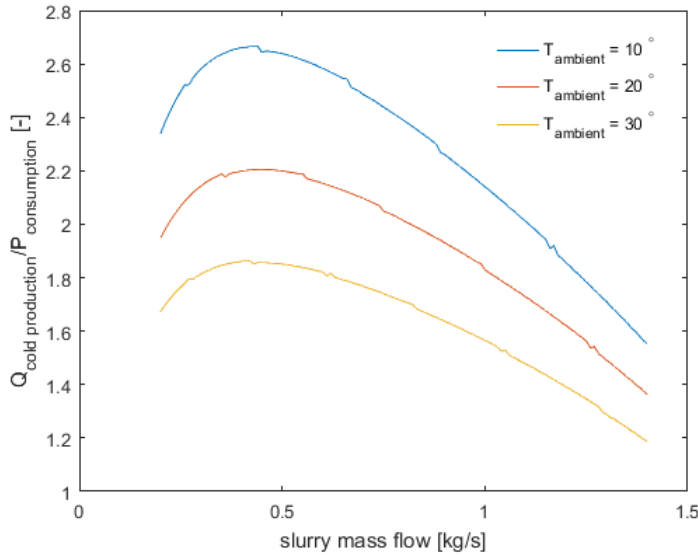

Figure 7.4: The ratio between the produced cold and the power consumption. The result are for an constant inlet crystal volume fraction of 0.20 and an evaporation pressure of 3.8 bar. The influence of the ambient air temperature is also shown although this temperature has little influence on the optimal slurry mass flow rate.

The influence of the temperature difference in the generator is also investigated. Therefore, the temperature difference between the refrigerant (at the inlet of the generator) and the slurry (also at the inlet of the generator) is controlled at 4 and 5 K. Lower evaporation temperature are not considered since the evaporation pressure cannot be reduced too much. A too low wall temperature in the heat exchanger will result in a very rapid crystallization resulting in blockages [80]. The result of the simulations is shown in table 7.2. The ratio between the cold production and the power consumption is never larger than 3.9. However this result is obtained for a TBAB solution of approximately 13.5 °C and an ambient temperature of 10 °C. Under these conditions a much higher ratio should be expected. The ratio is mainly so low due to the low pump efficiency. However, the pumps in the actual should still be replaced by a more efficient one. Furthermore, it should be noted just as with the air cooler there is a trade off between the efficiency and the capacity of the system. The capacity of the generator is not always sufficient for the optimum mass flow rate. In that case, the flow rates should be determined based on the required capacity of the equipment.

THE PRESSURE DROP AT THE GENERATOR SIDE OF THE SYSTEM

As shown in the previous section the pressure drop at the generator side of the system is quite large due to the required removal forces in the crystal layer. This loss mechanism should be further investigated in order to determine possibilities to optimize the system. Therefore, the model has been used to determine the pressure drop in the generator and the tubes for different solid fractions. These results are shown in figure 7.5. The figure shows that the pressure drop in the tubes increased just as expected with the solid fraction. This is no surprise since the slurry has a much higher viscosity then the solution. In the generator however the pressure drop is much more dependent on the initial TBAB fraction and less dependent on the crystal fraction. This because the required scrapping force is much higher for higher TBAB mass fractions as described by Daitoku and Utaka [14, 15] and as shown in figure 5.4. This model has still to be validated however based on these results the following can be concluded.

- The total pressure drop at the generation side of the system is in the range of 0.1 to 0.6 bar higher compared to the water system. This is mainly due to the increased pressure drop within the generator.

- The pressure drop in the generator can be lowered by using a lower initial TBAB fraction. This is because the pressure drop in the generator is mainly dependent on the required scrapping force. The influence of the solid fraction on this scrapping force is unknown and should therefore still be investigated.

Table 7.2: The optimum mass flow in the generator under certain operation conditions. The pump characteristic is used to determine the pump efficiency resulting in high power consumption.

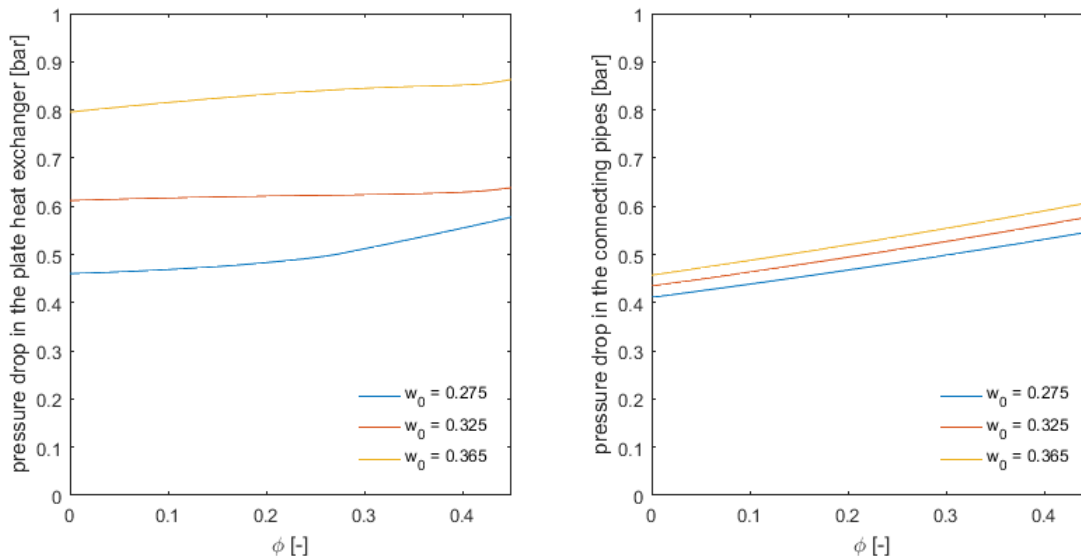| ϕ_{in} [-]	$\Delta T_{max,evap}$ [K]	T_{amb}[$°C$]	$\dot{m}_{opt}$ [kg/s]	ratio [-]
	4	10	0.31	3.90
		30	0.35	2.49
0		10	0.32	3.75
	5	30	0.38	2.40
	4	10	0.28	3.05
		30	0.39	2.07
0.20		10	0.41	3.20
	5	30	0.30	2.15
	4	10	0.35	3.24
		30	0.36	2.15
0.40		10	0.25	3.28
	5	30	0.34	2.18

Figure 7.5: Pressure drop of TBAB slurry in the generator (left hand side) and the tubes connecting the generator with the other components (right hand side). These results are obtained for three different initial mass fractions and a mass flow rate of 1 kg/s.

- The crystal fraction seems to have a negative effect on the pressure drop in the pipes. Therefore high solid fractions should be avoided if a large slurry distribution network is used.

7.3. CONCLUSION

The model of the TBAB is optimized in order to minimize the power consumption of the system. The optimal mass flow is determined to be in the range of 0.05-0.25 and 0.31-0.41 kg/s for respectively the utilization and generation side of the system. However, since the model has not yet been validated for the actual TBAB system the accuracy of these estimation is still unknown. Nevertheless, the same optimization method can be easily repeated when the model has been validated. The optimization shows that the performance of the system is limited by the high power consumption of the pumps. This is because the current system still use peripheral pump with a low efficiency. These pumps should, in the end, be replaced by more efficient ones.

The pressure drop in the generation side is one of the major losses during the cold production in the system. If the power consumption of the pump remains too high then it may be possible to reduce the pressure

drop in the generator by using a lower initial TBAB mass fractions. The pressure drop in the tubes can be limited by avoiding high solid fractions.

8

RESULTS

The model described in chapter 5 is used to evaluate the thermal and economic performance of both the water and the TBAB system. In this chapter the method and the results of the simulations are discussed. In the first section the cooling load used for this simulation is presented whereas in the next section the parameters for the simulations are discussed. Finally, the results of the simulations are presented.

8.1. COOLING LOAD

The cooling load of the installation in Twello has not yet been measured for a longer period of time. Therefore, simple model of a building has been developed. The aim of this model is to find a reasonable estimation of the indoor air temperature and of the cooling load during a year. The model does not describe the actual building in Twello. Writing an accurate model for the building in Twello would be more elaborate than necessary. Besides, too many variables like the exact dimensions and the occupancy of the room during a year are unknown. Therefore the model used in this study describes a fictional 100 m^2 office space with two external walls and a glass facade.

The office space is modeled using a control volume method. The building is divided into seven volume elements each with their own temperature and thermal mass. One volume element represent the air inside the building and another element represent the windows. The other elements make up the thermal mass of the wall and the floor. For each volume element an energy balance is made:

$$\sum \dot{Q} = mC_p \frac{dT}{dt} \tag{8.1}$$

The heat flow in the energy balance is the sum of the heat transfer through convection, conduction and due to mass transfer. For every time step of 300 seconds, the heat balances are solved and the temperature of each volume element is determined. The term on the right hand side represent the thermal mass of the volume element. This term is neglected for the volume element that represents the windows.

The model is used to simulate the room during one year. The solar radiation and the outside air temperature are obtained from the reference year described in NEN 5060 [50]. The solar radiation is averaged over the different surface orientations (north, east, south and west). The ventilation rate is assumed to be 36 m^3/(person hr) while the infiltration is assumed to be 0.4 ACH (air change per hour).

The result of the simulation is shown in figure 8.1. The total cooling load equals 28.1 MJ/m^2 and there are 662 hours with a cooling demand. This result is compared with the findings of a report by ECN [56]. In this report the heating and cooling load of different buildings has been investigated. Furthrmoe, it is investiagted how the cooling load is affected by parameters such as the thermal mass of the building, the insulation, the desired indoor air temperature and the control mechanism. For an office building the authors report a yearly cooling load ranging from 60.9 to 24.2 MJ/m^2 while the hours with cooling are ranging from 466 to 958. This is in good agreement with the cooling profile estimated by the model.

8.2. PARAMETERS

As explained in chapter ?? the pumps are not yet optimized for the system. Therefore, in the simulation a higher pump efficiency will be used in order to make the result more representative. The capacity of the
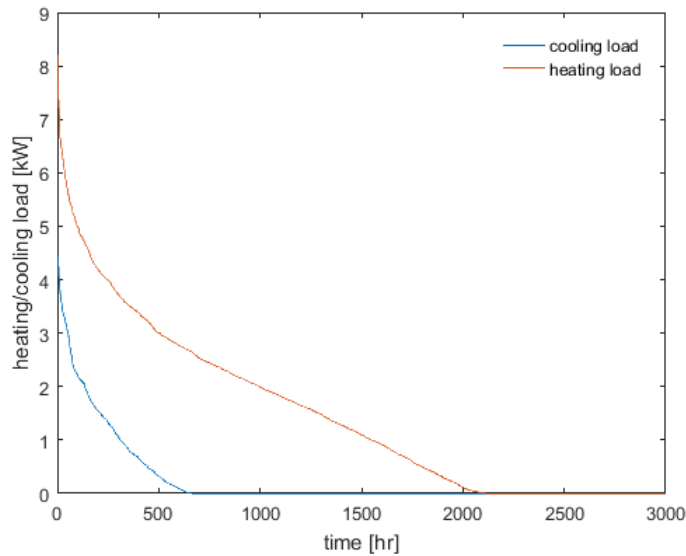
Figure 8.1: The heating and cooling load of the building. The total cooling load is 2.81 GJ (780.9 kWh) and there is a cooling load present during 662 hours in the year.

generator is usually smaller for the TBAB system than for the water system. Therefore the compressor will not operate at full capacity. As a result the fan in the condenser should also be controlled. This also means that the optimization presented in chapter **??** is not valid anymore. The mass flow can no longer be optimized using the same method since this will lead to unreasonable small capacities. Therefore the flow rate of the water in the generator is selected in such a way that the the generator will operate at a capacity of 3.5 kW. The other parameters used for the simulations are summarized in table 8.1.

Table 8.1: The parameters used for the simulations.

	Water system	TBAB system
η_{pump} [-]	0.60	0.60
T_{evap} [°C]	$T_{stor} - 4$	$T_{stor} - 4$
$\dot{m}_{generator}$ [kg/s]	0.40	0.40
$\dot{m}_{aircooler}$ [kg/s]	0.05-0.50*	0.15
$\dot{m}_{air}$ [kg/s]	0.05-0.50**	0.05-0.50*
start generation	$T_{stor} \geq 7°C$ or t = 23.00 hour	$\phi_{tank} = 0.05$ or t = 23.00 hour
stop generation	$T_{stor} \leq 6°C$	$\phi_{tank} \geq 0.10$ (day) $\phi_{tank} \geq 0.40$ (night)

* controlled to reach the desired cooling load
** controlled to reach an air outlet temperature of 16 °C

8.3. Results

The simulations are performed for both the water system and the TBAB system. The result clearly illustrates the working principle of both systems. The power consumption and the delivered cooling load during three consecutive days are plotted in figure 8.2 (water system) and figure 8.3 (TBAB system). The first graph shows the system operating with water as distribution fluid. The generation side of the system only starts if there is

a cooling load present, so it operates usually during the day. This means that it operates with higher ambient air temperatures than the TBAB system. The capacity of the generator and the air cooler are usually not the same. Fluctuations between these capacities are compensated by the storage. That is also why the cooling can continue for some time while the compressor is off.
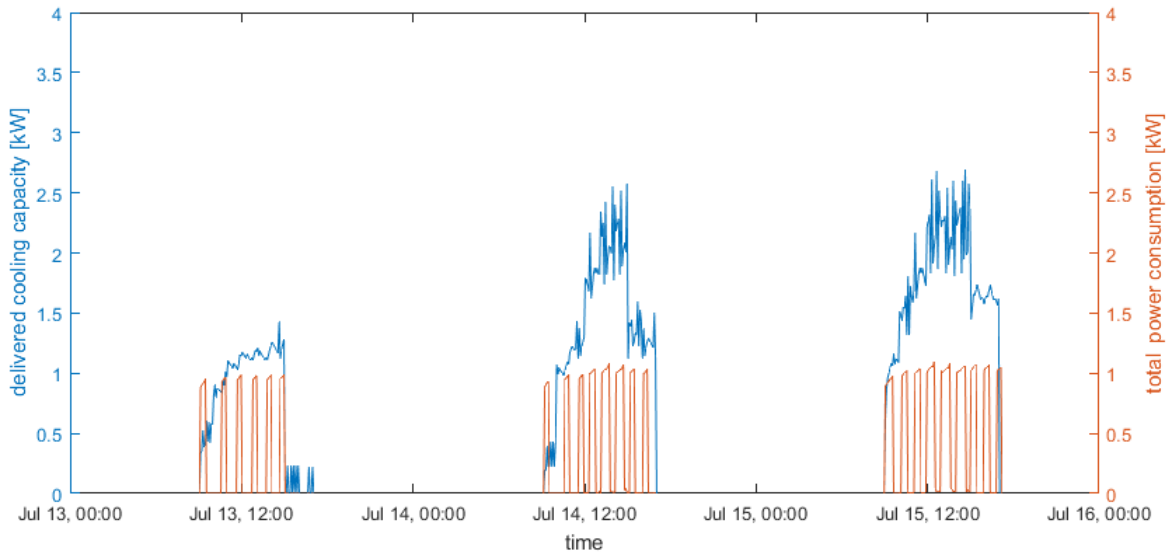

Figure 8.2: The delivered cooling load and the electric power consumption of the water air conditioning system.

Figure 8.3 shows the operation of the TBAB system. At 23:00 the generation of the crystals is initiated until a 40 % volume fraction is reached. The crystals are utilized during the day or slowly melt because of the heat transfer with the environment. At 23:00 the compressor is switched on again and the hydrates will be replenished. The figure shows that the power consumption at the utilization side is almost negligible compared to the power consumption of the generation side. The simulation also shows that the stored crystals are often insufficient to completely fulfill the cooling demand. Therefore, during certain days the hydrates are also produced (although less efficiently) during the day.
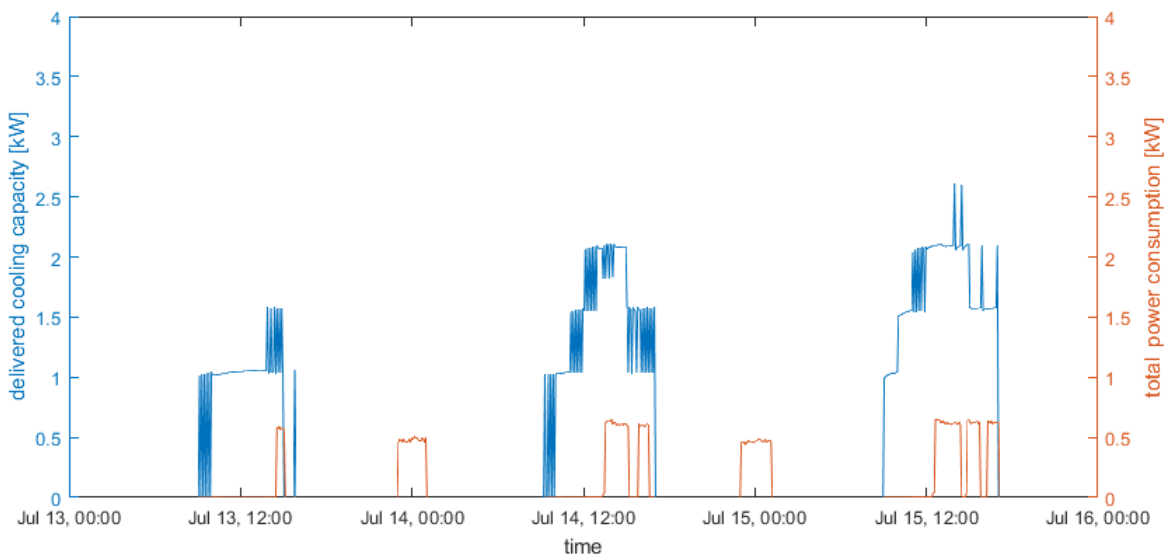

Figure 8.3: The delivered cooling load and the electric power consumption of the TBAB air conditioning system.

8.4. POWER CONSUMPTION

The simulations also provide an insight in the power consumption of the separate components. Table 8.2 provides an overview of the power consumption for both the TBAB and the water system under the same operating conditions. As shown in the table the compressor is the main power consumer in the water system; it accounts for 86.2 % of the total electric consumption. In the TBAB system the power consumption of the compressor is reduced by 30.5 % mainly due to the higher evaporation temperature. However the overall reduction in the power consumption is limited mainly due to the increased power consumption of the generation side pump. For this system the COP is defined as:

$$COP = \frac{\dot{Q}_{cool}}{\sum P_{elec}} \tag{8.2}$$

The simulations predict a 24.8 % reduction in the overall electric consumption. This corresponds to an increase in the COP from 2.96 to 4.00. However, this result is also very dependent on the determined cooling load and the control parameters. Changing the cooling load, the flow rates, the evaporation temperature or the setpoints for the storage will all have a quite large impact on the overall performance of the system.

Table 8.2: The electric power consumption of the individual components of the system during the cooling period (from May till October).

	Water system	TBAB system	Reduction [%]
Compressor [kWh]	238	166	30.5
Generator pump [kWh]	4.40	13.4	-204
Air cooler pump [kWh]	0.51	0.36	29.7
Condenser fan [kWh]	27.5	20.4	25.8
Air cooler fan [kWh]	5.65	8.26	-46.0
Total electricity consumption [kWh]	277	208	24.7
COP [-]	2.96	4.00	

8.5. INITIAL TBAB FRACTION

As shown in figure 3.1 the initial TBAB concentration will determine the phase change temperature of the solution. For this specific system a TBAB concentration of 36.5 wt% has been selected in order to ensure an as high as possible crystallization temperature. However such a high TBAB concentration also has some distinct disadvantages:

- It is well known that the TBAB crystals adhere more strongly to a surface for higher TBAB mass concentrations [14]. This will result in a larger pressure drop in the generator.

- The pressure drop of TBAB solution flowing through pipes or ducts slightly increases with the TBAB mass fraction.

- The investments cost increases with the TBAB fraction.

- It might increase the risk of blockages.

The influence of the initial TBAB concentration has also been simulated. The minimum TBAB concentration used for the simulations is 27.5 wt%; for lower TBAB concentrations the models is not valid anymore since mainly type B hydrates will be produced. The simulations are only done for the month of July. The COP in the month of July is higher than the average COP of the cooling period. This is because July has on average a much higher cooling load. This is the result of the Dutch weather; the cooling period spans a long period in time in which days with a very high cooling load alternate with periods without any cooling load. However, at the same time a high solid fraction in the storage tank is maintained regardless of the weather. The stored crystals will slowly melt due to the heat exchange with the environment. These losses add up and result in a significant reduction in the energy consumption.

As shown in figure 8.4 the simulations indicate that the pumping power increases with the initial TBAB concentration. However, the pumping power is only a very small part of the total power consumption. So the the savings achieved by reducing the pumping power are insufficient to compensate for the increase in the compressor power. This confirms that the best way to maximize the COP is to maximize the evaporation temperature. However the economics should be further analyzed to also determine the economic optimum.
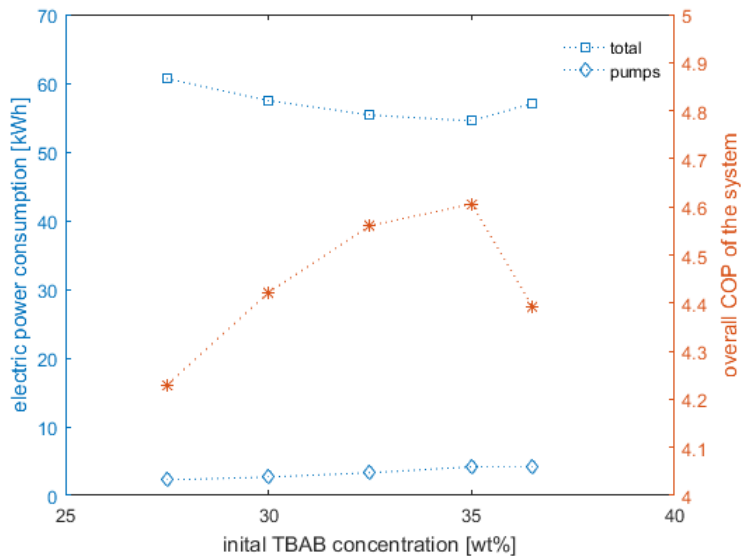
Figure 8.4: A comparison of the performance of the system of several different initial TBAB concentrations.

It is not known why the model predicts a much lower COP for an initial TBAB concentration of 36.5 wt%. The phase change temperature is the highest for an initial TBAB concentration of 36.5 wt% so the best energetic performance is expected. The simulations however show a sudden reduction in the efficiency for this TBAB concentration. One explanation is that this might due to the correlations used for the properties of the TBAB CHS. For example the viscosity of the solution is described by the Vogel-Tamman Fulche model as shown in figure 3.3. This model predicts a very rapid increase in the viscosity above the 30-35 wt% concentrations. This will result in a lower Reynolds and a lower convective heat transfer

8.6. STORAGE

The difference in the enthalpy between the slurry with a volume fraction of 0 and 0.40 is about 98 kJ/kg for an initial TBAB concentration of 36.5 wt%. So a 300 L storage tank could theoretically store 29400 kJ (8.2 kWh) of produced cold. For certain days this cooling capacity is sufficient while other days require a higher higher cooling capacity. The size of the storage tank should be further optimized based on the cooling load. However, an analysis of the result indicated that the losses due to heat transfer with the environment balance with the energy gained from using the storage. The COP of the system varies from 4.33 to 4.46 for a storage tank of respectively 150 and 500 liters. Since the gains are so small it is best to minimize the size of the storage tank in order to save on the investment costs.

The simulations are performed for a system in which the storage tank is placed inside the building. The storage tank is well insulated. However, there is always a temperature difference of about 7-10 K between the stored TBAB suspension and the room temperature. This results in a small energy loss to the environment; this energy loss is on average about 37 W. Over the summer a total of 135 kW/h of stored cold energy is lost. A better performance can be reached if the storage tank is placed outside. However, in that situation it is important that the tank does not adsorb too much direct solar radiation. This situation is also modeled. It is assumed that the storage tank is placed in outside, but it does not adsorb any solar radiation. In that case the heat flow to the environment is on average about 21 W, and the total electricity consumption reduces from 208 kWh to 195 kWh.

Another thing to consider is that the condensing unit is designed to operate at an evaporation temperature of around 2-5 °C and an ambient air temperature of about 20-35 °C. However, the TBAB system operates at an evaporation temperature of about 8.5 °C while the ambient air temperature reduces to about 10-20 °C during the nights. The condensation temperature is directly related to the ambient air temperature so it will also be reduced. The low condensation and high evaporation temperature mean that the generator operates at low pressure ratios. Figure 8.5 shows the ambient air temperature and the pressure ratio of the compressor for the TBAB system. This pressure ratio is also used to estimate the isentropic efficiency as shown in figure 5.7. During the night the pressure ratio is often less then 2, so the isentropic efficiency will be around 15-20
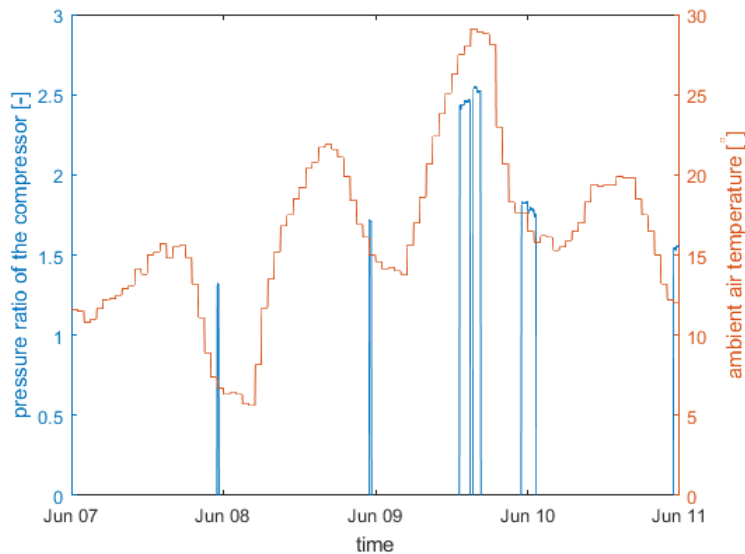
Figure 8.5: The pressure ratio in the compressor as predicted by the model at different ambient air temperature.

% lower than during the day.

As explained earlier the model predicts a lower isentropic efficiency of the compressor during the night. Nevertheless the COP of the cold production still increases for lower ambient air temperature. The time at which the nighttime generation of the crystals is initialized can be further optimized. Now the system switches on at 23.00 since this corresponds to the lower electricity tariff in the Netherlands. However, when it switches on at a later time then the COP can be even further increased. For example if only the month of July is considered than the COP can be increased from 4.39 to 4.53 if the setpoint is changed from 23.00 hr to 2.00 hr.

8.7. CONCLUSION

In this chapter the result of the simulations are presented. The cooling load needed for the simulations is calculated with the help of a simple dynamic model. This model described a fictional 100 m^2 room in an office building and uses Dutch climate data to calculate the cooling requirements.

The simulations show that overall COP of the system increased from 2.96 to 4.00 if TBAB instead of water is used as distribution fluid. This corresponds to a reduction in the energy consumption of 24.7 %. This was mainly due to a 30.5 % reduction in the compressor power. At the same time the power consumption of the generation side pump increased by 204 % due to the formation of the crystal layer in the generator. The simulations confirmed that the pumping power could be reduced by lowering the initial TBAB concentration. However, this also meant lowering the crystallization temperature which result in a higher compressor power. The best performance is obtained for a initial TBAB concentration of 35 wt%.

9

DISCUSSION

The results in chapter 8 show that using TBAB can reduce the energy consumption of the system. This result however is dependent on a number of different factors. In this chapter these factors are presented and discussed.

9.1. CAPACITY OF THE EQUIPMENT

The geometry of the equipment in the system should be selected based on the chosen distribution fluid. The capacity of the generator is much larger for water than for the TBAB CHS. This is mainly due to the crystal adhesion in the TBAB system. The crystals form a dense layer that provide additional resistance to the heat transfer. This can be illustrated by the overall heat transfer coefficient in the evaporation zone of the heat exchanger. According to the model, this heat transfer coefficient is about 950 W/(m² K) for the water system and about 460-500 W/(m² K) for the TBAB system. This means that under these conditions the capacity of the generator reduces from about 3.7 to 2.8 kW. Luckily, the cooling capacity of the TBAB systems remained sufficient due to the storage tank and the fact that the crystal layer would melt as soon as the solution became superheated.

Replacing the water by the TBAB solution also affects the required capacity of the other components. The cooling capacity of the produced TBAB slurry is much larger then that of water, so generally speaking the flow rates in the system can be reduced. However, the cooling capacity of the TBAB slurry is dependent on the crystal fraction. At the beginning of the cooling process the crystal solid fraction is close to 40 %. However, the solid fraction reduces as crystal are utilized. This also means that the cooling capacity of the slurry reduces over time. So, unless a more complicated storage technique is applied, the TBAB system must also be able to deal with higher flow rates. This means that the capacity of the pumps can not be reduced in the TBAB system. The capacity of the generator side pump may even be increased due to the higher pressure drop in the generator.

The capacity of the air cooler should be selected based on the peak cooling load. As explained in section 6.1 is the convective heat transfer at the water side much higher than that of the air side. This means that the capacity of the air cooler is mainly dependent on the air side heat transfer. However, the convective heat transfer coefficient at the slurry side does reduces due to the lower flow rates and the re-laminarization. So the capacity of the air cooler will be lower in the TBAB system, although this might be solved by selecting an air cooler with a smaller flow passage for the TBAB system.

CONDENSING UNIT

The capacity of the condensing unit should be selected to match the capacity of the generator. However, in the actual system this is not necessarily the case. While the capacity of the condensing unit is appropriate for the water system it is overdimensioned for the TBAB system. As a result the compressor will operate at 30 to 60 % of the maximum rotational speed if the TBAB solution is used. This is not only due to the low capacity of the generator but also due to the reduced pressure ratio in the refrigerant cycle.

In reality it might not be possible to operate the compressor at such low rotational speeds. If it is possible to operate the condenser at partial load then one problem that may arise is the high power consumption of the condenser fan. The simulations show that may accounts for as much as 23.4 % of the total power con-

sumption of the system. Therefore, the model assumes that the fan is controlled based on the rotational speed of the compressor. In that situation the power consumption of the fan reduces with 62.8 % from 54.9 kWh in the uncontrolled situation to 20.4 kWh in the controlled situation. So adding a control for the condenser fan will significantly reduce the power consumption of the system.

The relative high power consumption of the condenser fan is also the result of the fluctuations in the capacity of the compressor. These fluctuations are the result of the high difference between the condensation pressure during the night and during the day. This difference will always be there regardless of the selected compressor. Therefore, it might still be beneficial to actively control the condenser fan even if a different compressor is selected.

9.2. FLOW RATES

Many authors have noted that the higher cooling capacity of the TBAB slurry can be used to reduce the flow rates in the system [45, 52, 75]. This would be beneficial since it would also reduce the power consumption of the pumps. However, these studies usually refer to systems which include a large distribution network. In these systems the TBAB CHS is centrally produced and stored. During the day, when there is a coolind demand, the TBAB slurry is distributed over a numbers of air coolers located throughout the building. These kind of systems are associated with high pumping requirements. For example Ogoshi and Takao [52] compared the performance of water and the TBAB solution in a large scale (around 1055 kW) air conditioning system. With water as a distribution fluid the pumps accounted for 41 % of the total electricity consumption of the system. They managed to reduce the pumping power by 68 % by replacing the water by a TBAB solution.

The situation investigated by Ogoshi and Takao is quite different from the situation in the pilot system in Twello. In the pilot plant, the pumps consume very little power while the condensing unit accounts for the majority of the power consumption. The utilization side pump only accounts for less then 1 % of the total power consumption. Still, the model predicts a 29.7 % decrease in the utilization side pumping power for the TBAB system. The flow rates can even be further optimized although in this specific system the options are limited:

- The system should be able to operate with very low TBAB CHS mass flows in order to fully profit from the increased cooling capacity. For example if the stored TBAB CHS has a solid fraction of 0.40 % then a 3.5 kW cooling capacity could be reached by using a slurry flow rate of 0.016 kg/s. In that case the velocity of the slurry in the air cooler becomes so low that the convective heat transfer inside the tubes will limit the overall capacity.

- The flow rates can only be minimized if the mixing of the superheated solution and the CHS is avoided. Otherwise the crystal fraction of the slurry reduces over time, resulting in a lower cooling capacity of the slurry. One way to work around this problems is by using multiple storage. For example, in the study of Ma et al. two separate storage tanks were used, one for the produced CHS and on for the TBAB solution [45]. High crystals fractions can also be maintained in single storage system. This is a shown by Douzet et al. [21]. They maintained solid fractions of 40 to 50 wt% during the cooling process by making use of the setting of the crystals.

The power consumption of the generation side pump increases with about 204 % for the TBAB system. This increase in the pumping power is much smaller than expected based on the result of Zak [74]. Zak reported an increase in the total pump power consumption from 10.4 kWh to 210.2 and 837.8 kWh for differently controlled TBAB systems. One reason for this difference is that this study used a different approach to determine the required scrapping force. Another difference is that during this study the the generator mass flow was maintained at 0.4 kg/s. The drawback of using such a low flow rate is that it also limits the capacity of the generator. Maybe this could be solved by reducing the evaporation temperature or be decreasing the superheating. These options should be further investigated with the validated model.

9.3. ECONOMIC CONSIDERATIONS

The TBAB solution will not only reduce the energy consumption of the system, but it also offers the possibility to profit from lower energy tariffs. In the Netherlands two tariffs for electricity are used; one tariff is used for the period between 7:00 till 23:00 and another tariff is used during the nights, weekends and national holidays. The price of the electricity has been determined based on actual electricity prices from energy suppliers. A

price of €0.19010/kWh can be used for the peak tariff while a price of €0.17900/kWh can be used for the off-peak tariff [23]. The difference between these two tariffs is only about 10 %, this is less than in for example Japan.

The effect of these two tariffs on the energy savings can be further investigated using the results presented in section 8.4. The energy consumption of the system reduced by 24.8 %. At the same time the price of the consumed electricity reduced by 26.0 % from €51.70/year to €38.24/year. So the electricity costs reduced by about 5 % more than the energy consumption. The observed cost saving is much smaller compared to case studies from Japan [52]. This is however a direct result of different electricity tariffs.

During this research several aspects were encountered which require a detailed economic assessment. These aspects are summarized below:

- A TBAB system requires a higher capacity generator. Furthermore, depending on the systems and the control mechanism, it also requires different pumps. So the costs of the equipment will be higher compared to a conventional water systems. However, some saving in the piping cost may be achieved if the flow rates can be reduced.

- The price of the TBAB varies depending on the quantity and the purity. The TBAB used in the pilot system in Twello was purchased for €10.00/kg. The system requires about 120 kg of TBAB so this will also account for a considerably increase in the investments costs.

- The initial TBAB concentration and the size storage tank should also be further evaluated. The best energetic performance is reached by using a 35 wt% TBAB solution. However, reducing the initial TBAB concentration might be an attractive method to reduce the investments costs. This trade off between efficiency and investments costs should also be further analyzed.

9.4. Comfort

The comfort of a building is dependent on a number of different factors including the temperature, humidity, temperature gradients, air velocity and lighting. These factors can be individually controlled however for simplicity's sake the model only takes the air temperature into account. The other parameters are also important although they are less relevant for the performance of the air conditioning system. In the model the inside air temperature is kept at a maximum of 23 °C. Actual air conditioning systems sometimes allow for higher inside air temperatures as a way to limit the required capacity and energy consumption of the system. Raising the indoor air temperature can be considered as very simple but effective method to save energy, however it will also affect the comfort of the building.

The allowable inside air temperature has a considerable effect on the performance of conventional system. Usually the distribution fluid is cooled down from 12 to 7 °C. However, if the inside air temperature is raised by for example 5 °C, then the water has only to be cooled down from 17 to 12 °C. In that situation the evaporation takes place at approximately the same temperature as in the TBAB system. The TBAB solution has still its storage tank and the larger cooling capacity as an advantage. However, for systems with a small distribution network these advantages may not be sufficient to warrant the additional investment costs. However the systems, installed by the JFE Engineering Corporation, usually produce type B hydrates at approximately 8 °C. So in these system the TBAB slurry is produced at roughly the same temeprature as the chilled water. Nevertheless, large energy savings are reported due to the reduction in pumping power [52, 75].

As mentioned earlier the humidity is not controlled in the actual system. The model offers an estimation of the condense production and the humidity at the outlet air cooler. However, the humidity is not controlled and an estimation for the humidity of the room is not included in the model. In larger buildings the air is usually controlled by a HVAC (heating ventilation and air conditioning) unit. These units do not only control the temperature of the room but also the ventilation and the humidity of the room. As shown in figure 9.1, a HVAC unit usually consist out of two separate heaters and a cooler. This is necessary to control the humidity of the room.

- The first heater heats up the air before it enters the humidifier. It increases the temperature of the air and therefore also the amount of water that can be dissolved in the air. During the humidification process the temperature of the air is reduced. Therefore a second heater is also included in the HVAC unit. The first heater is only used if there is a heating demand or if the air must be humidified. Therefore, this heater is rarely used during the summer.

- The cooler is intended to cool the air to its desired temperature. However, if the humidity of the cooled air is too high then the air must be further cooled down in order to condensate the excess water in the air. The temperature to which the air is cooled depends on temperature of the air cooler, the desired air temperature and the desired humidity. It can be determined using the Mollier diagram which is presented in appendix A.

- In the last heater the air is heated to the desired outlet temperature. During the heating process the humidity ratio (the ratio between mass of the water and the mass of the air) stays constant, while the relative humidity reduce due to increased solubility of the water in the air.
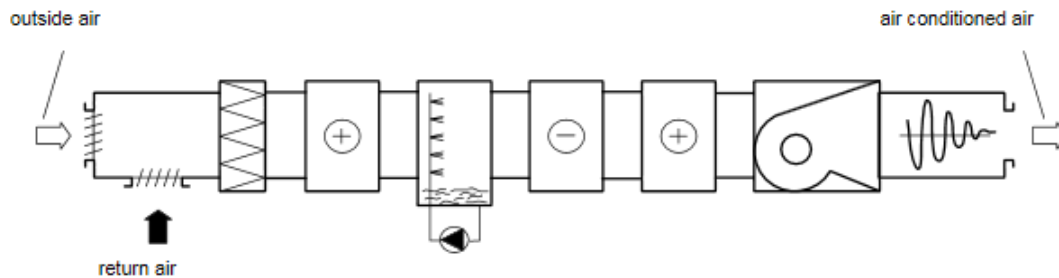

Figure 9.1: A schematic drawing of the components in a HVAC unit [54]. The air travels in consecutive order through a filter and/or additional heat exchangers, a heater, a humidifier, a cooler and another heater.

The (de)humidification of the air is not included in the model. In the dehumidifier chilled water has a advantage over the TBAB solution. The wall temperatures in the air cooler are lower when chilled water is used. Furthermore, chilled water offers the possibility to (locally) cool the air to below the 12.5 °C. This is not possible when a 36.5 wt% TBAB slurry is used. It should be further investigated if the TBAB solution will also suffice in a dehumidifier, although based on the Mollier diagram no problems are expected. Theoretically speaking, a HVAC unit utilizing a 12.5 °C TBAB slurry should be able to produce air with a relative humidity of well below 70 % and a temperature of 22 °C.

9.5. CONCLUSION

In this chapter several topics related to the performance of the systems are discussed:

- The capacity of the equipment should be different for the TBAB and water system. For the TBAB system a higher capacity generator and/or a lower capacity condensing unit should be installed. In the actual system the condensing unit may be overdimensioned for the TBAB system. In the model this is solved by operating the compressor at partial load. Further research is required in order to determine the feasibility of this solution.

- In the literature the energy reduction is TBAB air conditioning systems are often associated with a reduction in the flow rates and therefore a reduction in the pumping power. However, the system in Twello does not include a large distribution network, so the utilization side pumping cost are almost negligible. Instead, the power savings due to the higher evaporation temperature and lower condensation temperature. For larger system both energy saving methods may be combined.

- The desired indoor air temperature will also determine the suitability of using TBAB. For now a maximum air temperature of 23 °C is assumed. If higher indoor air temperatures are allowed then the efficiency of the water system will increase, while the performance of the TBAB system will remain more or less the same. The model also does not include the (de)humidifaction of the air, although based on the Mollier diagram no problems are expected when a 36.5 wt% TBAB solution is used in a dehumidifier.

10

CONCLUSION

In this study the performance of TBAB as secondary refrigerant in air conditioning applications is investigated. This is done by modeling the performance of the system using both water and a 36.5 wt% TBAB solution as secondary refrigerant. The geometry of the equipment is kept the same as that of the pilot system in Twello.

10.1. MODELING APPROACH

The system is modeled using a steady state approach. Just as in earlier research the thickness of the crystal layer in the generator is modeled by using an analogy with scrapped surface heat exchanger. Therefore the model relies on the following assumptions:

- The produced crystal will not create any blockages in the system.

- The friction losses of the CHS in the generator are equal to the scrapping work.

- The required removal work can be related to experimentally determined scrapping force.

The other components are modeled with the help of empirical correlations and data and reference models provided by the manufacturers of the equipment. The system could only be validated using water as secondary refrigerant since experimental data for the TBAB solution were not yet available.

The mass flows in this system can be optimized in order to minimize the energy consumption of the system. The optimal mass flow for the crystal production is determined to be about about 0.31-0.41 kg/s. However, higher mass flow are required in order to meet the desired capacity. Furthermore, the performance of the system is improved if:

- The peripheral pumps in the systems are replaced for more efficient pumps (with an assumed efficiency of 60 %).

- The rotational speed of the condenser fan is controlled in order to limit its power consumption. This necessary since the condensing unit usually operates at partial load.

- The condensation pressure is always controlled based on the ambient temperature.

10.2. ENERGETIC PERFORMANCE

The energetic performance of the system was modeled using both water and a 36.5 wt% TBAB solution as secondary refrigerant. The cooling load for the model is obtained using a small dynamic model of a fictional 100 m^2 room in a office building somewhere in the Netherlands. Only the period from May to October is simulated since these are the only months for which there is a cooling load present. In this period the overall COP of the water system is 2.96. The COP of the system increases to 4.0 if the secondary refrigerant is replaced by the TBAB solution. This correspond with an energy reduction of 24.8 %.

Of the individual components the compressor has by far the largest power consumption. In the water system it accounts for 86.2 % of the total energy consumption. The power consumption of the compressor

reduces with 30.5 % if the TBAB solution is used. This is the result of the higher evaporation temperature and the lower condensation temperature (due to the nighttime generation) in the TBAB system. However, when TBAB is used the pressure drop in the generator increases due to the adhesion of the crystals to the heat exchanger surface. This results in a 204 % increase in the generation side pumping power. However, even in this situation, the pumping power only accounted for 6.5 % of the total power consumption of the system.

Research has shown that the crystals adhere less strongly to the surface for lower TBAB concentration. Therefore, reducing the initial TBAB fraction will also reduce the friction losses in the generator. However, lowering the TBAB concentration also reduces crystallization temperature. This will result in a lower evaporation temperature and therefore a higher compressor power. The best performance is obtained by using a 35.0 wt% TBAB concentration.

One thing to consider is that the condensing unit was designed for higher capacity and pressure ratio than encountered in the TBAB system. Due to the high evaporation and low ambient air temperature the pressure ratio of the compressor reduces. This means that for the TBAB system the pressure ratio is often less than 2 during the nighttime operation. Under these conditions the model predicts an about 20 % lower isentropic efficiency than for the conventional system. Another thing to consider is that this system does not include a large distribution network. Therefore, it does not profit as much from the lower flow rates as many examples reported in the literature. This means that for system with a larger distribution network an even large energy saving might be achieved.

Finally, it should be noted that the results are obtained for a room maintained at maximum temperature of 23 °C. If higher indoor air temperatures are allowed then the performance of the water system will be considerably improved. At the same time the efficiency of the TBAB system will remain more or less the same.

10.3. HYPOTHESIS

The observations from this report are used to validate the hypothesis defined in chapter 1. The hypothesis proposed for this research was:

The energy consumption of the secondary loop air conditioning system installed in Twello can significantly be reduced if a TBAB hydrate slurry instead of water is used a secondary refrigerant.

The hypothesis was tested by modeling the performance of the system under certain conditions. The simulations predict a 24.8 % reduction in the electricity consumption if a 36.5 wt% TBAB solution is used. So the hypothesis is validated under the condition that assumptions presented in section 10.1 hold. These assumptions still have to be validated using newly obtained experimental data from the pilot system in Twello.

11

RECOMMENDATIONS

In this thesis several topics are encountered and discussed which require further studying. Some of these topics can at this moment not be further analyzed since the experimental data of the pilot plant is not yet available, while other topics might deserve a study on their own.

11.1. CONTINUATION OF THIS RESEARCH

At the moment the research to the TBAB air conditioning plant in Twello is continued by Sven Drommel. He will continue to improve the model and do the validation for the TBAB system. During the validation of the model, special attention should be paid to the performance of the generator:

- The mass transfer in the generator is described using the Sherwood number. The most appropriate correlation for the Sherwood number should still be selected with the help of the experimental data.

- The correlations which relate the crystal growth to the friction forces (as presented in section 5.2) are newly developed and therefore not yet validated with experimental data. This method should be validated with experimental data, and it should investigated whether this method also provides an accurate estimation of the crystal layer thickness.

- The model calculates the crystal growth using a correlation for the mass transfer rate. This correlation describes the crystal growth without taking the nucleation process into account. Therefore, the model might underestimate the subcooling in the generator. This effect will be the most prevalent if there are no crystals present within the flow. It should be investigated whether the subcooling is indeed underestimated by the model, and how this will affect the overall performance of the system.

11.2. POSSIBILITIES FOR IMPROVEMENT

The continuation of the research to the pilot plant will provide more insight in the performance of the actual system. In the report several recommendations for the development and optimization were already discussed. These recommendations are summarized below:

- A control of the evaporation pressure will be very useful in order to optimize the operating conditions of the generator. Furthermore, it could also be necessary in order to prevent a too rapid crystallization in the generator.

- The condensation pressure should reduce for lower ambient air temperatures. This could be achieved by controlling the rotational speed of the compressor.

- The capacity of equipment changes if a TBAB solution is used. The heat transfer in the generator reduces due to the formation of a crystal layer. Furthermore, the TBAB system makes use of a higher evaporation temperature and lower condensation temperature. This means that in the TBAB system the compressor usually operates at partial load. It should be investigated whether it is actually possible to efficiently operate the compressor under these conditions. If it is possible then the condenser fan must also be controlled in order to maintain a high efficiency.

- The system still makes use of peripheral pumps with a low efficiency. This is necessary in order to fully investigate the behavior of the system. However, these pumps should in the end be replaced by more efficient ones in order to reach a better efficiency.

11.3. SUGGESTIONS FOR FURTHER RESEARCH

There are also a number of topics which have been touched upon in this study but were not further examined. The topics can be the subject of or be included in future studies:

- An economic assessment should still be performed in order assess the financial implications of using TBAB slurry.

- The properties of the crystal layer should be further investigated. It is known that the crystal layer becomes more difficult to remove for a repeatedly scrapped surface [14, 20]. It is therefore important to further investigate the properties of the crystal layer and how these properties change over time.

- The control of the system should be further optimized in order to maximize the efficiency of the system. For now the mass flow rates are constant regardless of the solid fraction of the tank. However, the cooling capacity of the slurry increase with the solid fraction. This means that the flow rate of the slurry can be further minimized as a way of reducing the power consumption of the pumps.

- In this research the growth of the crystal layer is limited by the friction with the flow. However, the simulations show that this method of removing the crystals will lead to a high pressure drop in the generator. It is also possible to limit the thickness of the crystal layer by for example melting the crystal layer (by reversing the operation of the refrigerant cycle) or by using a scrapped surface heat exchanger. It should still be investigated whether these or other removal techniques can be used to improve the performance of the system.

- The TBAB system offers the possibility to temporarily store energy for air conditioning applications. This mean that the electricity consumption of the systems does not have to align with the cooling demand of the building. This property is very useful in smart grids. By managing the time at which the crystals are produced it possible to adjust the electricity consumption of the system in such a way that it better matches with the electricity supply in the grid.

- The TBAB powder used in the system it is slightly contaminated with silicon so it only has a purity of 97 %. TBAB of higher purity is available, however it is much more expensive and therefore not practical to use for this application. It should therefore be investigated how these contaminants affect the performance and/or the lifespan of the system.

- TBAB is just one of several phase change materials that are proposed and studied for air conditioning applications. For example trimethylolethane (TME) and tetrabutylammonium fluoride (TBAF) have also been suggested as alternative secondary refrigerant [75]. Another option is to use a CO_2 hydrate slurry, although due to the necessity of highly pressurized CO_2 it requires a more complicated system. Further research is required in order to compare the performance and opportunities of these different techniques.

BIBLIOGRAPHY

[1] AlfaLaval. Brazed plate heat exchangers, for the refrigeration industry, 2016.

[2] R. L. Amalfi, F. Vakili-Farahani, and J. R. Thome. Flow boiling and frictional pressure gradients in plate heat exchangers. Part 2: Comparison of literature methods to database and new prediction methods. *International Journal of Refrigeration*, 61:185–203, 2016.

[3] O. P. Arsenyeva, B. Crittenden, M. Yang, and P. O. Kapustenko. Accounting for the thermal resistance of cooling water fouling in plate heat exchangers. *Applied Thermal Engineering*, 61(1):53–59, 2013.

[4] O. P. Arsenyeva, L. L. Tovazhnyanskyy, P. O. Kapustenko, G. L. Khavin, A. P. Yuzbashyan, and P. Y. Arsenyev. Two types of welded plate heat exchangers for efficient heat recovery in industry. *Applied Thermal Engineering*, 2016.

[5] T. Asaoka, H. Kumano, and M. Serita. Measurement of latent heat of tetra-n-butylammonium bromide (TBAB) hydrate. *International Journal of Refrigeration*, 36(3):992–997, 2013.

[6] Babcock & Wilcox Company. *Steam, its generation and use.* Number v. 39. Babcock & Wilcox., 1978.

[7] R. Barzegarian, M. K. Moraveji, and A. Aloueyan. Experimental investigation on heat transfer characteristics and pressure drop of BPHE (brazed plate heat exchanger) using TiO 2–water nanofluid. *Experimental Thermal and Fluid Science*, 74:11–18, 2016.

[8] J. Bellas, I. Chaer, and S. Tassou. Heat transfer and pressure drop of ice slurries in plate heat exchangers. *Applied Thermal Engineering*, 22(7):721–732, 2002.

[9] Bitzer. Ecoline, 2016. https://www.bitzer.de/gb/en/products/Technologies/Reciprocating-Compressors/Semi-hermetic/For-standard-refrigerants/ECOLINE/.

[10] Bitzer. LHE series with ECOLINE compressors, 2016. https://www.bitzer.de/fi/en/products/Technologies/Condensing-Units/With-semi-hermetic-compressors/Air-cooled/LHE-series-with-ECOLINE-compressors//.

[11] D. E. Briggs and E. H. Young. Convection heat transfer and pressure drop of air flowing across triangular pitch banks of finned tubes. In *Chem. Eng. Prog. Symp. Ser*, volume 59, pages 1–10, 1963.

[12] P. Colonna, T. van der Stelt, and A. Guardone. FluidProp (Version 3.0): A program for the estimation of thermophysical properties of fluids. *Asimptote, Delft, The Netherlands, http://www. fluidprop. com*, 2012.

[13] S. Cox. Cooling a warming planet: A global air conditioning surge. YaleEnvironment360, 2012.

[14] T. Daitoku and Y. Utaka. Adhesion and detachment characteristics of a TBAB hydrate solid on a heat transfer surface (effect of concentration of TBAB solutions). *Heat Transfer—Asian Research*, 38(6):370–384, 2009.

[15] T. Daitoku and Y. Utaka. Separation characteristics of clathrate hydrates from a cooling plate for efficient cold energy storage. *Applied Energy*, 87(8):2682–2689, 2010.

[16] M. Darbouret, M. Cournil, and J.-M. Herri. Crystallisation and rheology of an hydrate slurry as secondary two-phase refrigerant for air-conditioning application. In *2nd Phase Change Material and Slurry Workshop & 6th IIR Ice Slurry Workshop, 25 juin 2005*, 2005.

[17] M. Darbouret, M. Cournil, and J.-M. Herri. Rheological study of TBAB hydrate slurries as secondary two-phase refrigerants. *International Journal of Refrigeration*, 28(5):663–671, 2005.

[18] L. Davis. Air conditioning and global energy demand. Energy Institue at Haas, 2015.

[19] V. D. Donowski and S. G. Kandlikar. Correlating evaporation heat transfer coefficient of refrigerant R134a in a plate heat exchanger. 2000.

[20] J. Douzet, P. Brantuas, and J.-M. Herri. Building of a life size testing unit for air conditionning by using TBAB hydrate slurry as a secondary two-phase refrigerant. In *7th International Conference on Gas Hydrates (ICGH 2011)*, page 440, 2011.

[21] J. Douzet, M. Kwaterski, A. Lallemand, F. Chauvy, D. Flick, and J.-M. Herri. Prototyping of a real size air-conditioning system using a tetra-n-butylammonium bromide semiclathrate hydrate slurry as secondary two-phase refrigerant–Experimental investigations and modelling. *International Journal of Refrigeration*, 36(6):1616–1631, 2013.

[22] R. Eldeeb, V. Aute, and R. Radermacher. A survey of correlations for heat transfer and pressure drop for evaporation and condensation in plate heat exchangers. *International Journal of Refrigeration*, 65:12–26, 2016.

[23] Energieleveranciers.nl. Energieprijzen vergelijken, 2017. https://www.energieleveranciers.nl obtained at 24 march.

[24] D. Flick, C. Doursat, and M. B. Lakhdar. Modelling and numerical simulation of ice slurry storage tank. *Computer Aided Chemical Engineering*, 24:1169–1174, 2007.

[25] W. Focke, J. Zachariades, and I. Olivier. The effect of the corrugation inclination angle on the thermohydraulic performance of plate heat exchangers. *International Journal of Heat and Mass Transfer*, 28(8):1469–1479, 1985.

[26] K. Fujiura, Y. Nakamoto, Y. Taguchi, R. Ohmura, and Y. Nagasaka. Thermal conductivity measurements of semiclathrate hydrates and aqueous solutions of tetrabutylammonium bromide (tbab) and tetrabutylammonium chloride (tbac) by the transient hot-wire using parylene-coated probe. *Fluid Phase Equilibria*, 413:129–136, 2016.

[27] D. H. Han, K. J. Lee, and Y. H. Kim. Experiments on the characteristics of evaporation of r410a in brazed plate heat exchangers with different geometric configurations. *Applied thermal engineering*, 23(10):1209–1225, 2003.

[28] J. Henley. World set to use more energy for cooling than heating. The Guardian, 2015.

[29] J. Huang, T. J. Sheer, and M. Bailey-McEwan. Heat transfer and pressure drop in plate heat exchanger refrigerant evaporators. *International journal of refrigeration*, 35(2):325–335, 2012.

[30] C. Infante Ferreira. Lecture notes Wb4427 Refrigeration Technology and Applications, 11 October 2016.

[31] M. Isaac and D. P. Van Vuuren. Modeling global residential sector energy demand for heating and air conditioning in the context of climate change. *Energy policy*, 37(2):507–521, 2009.

[32] JFE Engineering Corporation. Neo White® (clathrate hydrate slurry) thermal energy storage for air conditioning systems. http://www.jfe-eng.co.jp/en/products/energy/air_conditioning/air02.html.

[33] P. Kapustenko, O. Arsenyeva, and O. Dolgonosova. The heat and momentum transfers relation in channels of plate heat exchangers. *Chemical Engineering Transactions*, 25:357–362, 2011.

[34] H. Kumano, T. Hirata, and Y. Kobayashi. Flow and heat transfer characteristics of a tetra-n-butyl ammonium bromide hydrate slurry in the transition region. *International Journal of Refrigeration*, 35(8):2085–2092, 2012.

[35] H. Kumano, T. Hirata, and T. Kudoh. Experimental study on the flow and heat transfer characteristics of a tetra-n-butyl ammonium bromide hydrate slurry (first report: flow characteristics). *international journal of refrigeration*, 34(8):1953–1962, 2011.

[36] H. Kumano, T. Hirata, and T. Kudoh. Experimental study on the flow and heat transfer characteristics of a tetra-n-butyl ammonium bromide hydrate slurry (second report: heat transfer characteristics). *international journal of refrigeration*, 34(8):1963–1971, 2011.

[37] H. Kumar. The plate heat exchanger: construction and design. In *Institute of Chemical Engineering Symposium Series*, volume 86, pages 1275–1288, 1984.

[38] E. Lemmon, M. Huber, and M. McLinden. REFPROP: Reference fluid thermodynamic and transport properties. *NIST standard reference database*, 23(8.0), 2007.

[39] D. Li, D. Liang, H. Peng, and L. Wan. Thermal conductivities of methane–methylcyclohexane and tetra-butylammonium bromide clathrate hydrate. *Journal of Thermal Analysis and Calorimetry*, 123(2):1391–1397, 2016.

[40] W. Li, H. Li, G. Li, and S. Yao. Numerical and experimental analysis of composite fouling in corrugated plate heat exchangers. *International Journal of heat and mass transfer*, 63:351–360, 2013.

[41] G. Longo and A. Gasparella. Refrigerant R34a vaporisation heat transfer and pressure drop inside a small brazed plate heat exchanger. *International journal of refrigeration*, 30(5):821–830, 2007.

[42] Z. Ma and P. Zhang. Pressure drop and heat transfer characteristics of clathrate hydrate slurry in a plate heat exchanger. *international journal of refrigeration*, 34(3):796–806, 2011.

[43] Z. Ma and P. Zhang. Modeling the heat transfer characteristics of flow melting of phase change material slurries in the circular tubes. *International Journal of Heat and Mass Transfer*, 64:874–881, 2013.

[44] Z. Ma and P. Zhang. Pressure drop and heat transfer characteristics of tetra-n-butyl ammonium bromide clathrate hydrate slurry during flow melting and generating in a double-tube heat exchanger. *Experimental Thermal and Fluid Science*, 44:227–234, 2013.

[45] Z. Ma, P. Zhang, and R. Wang. Performance of a cold storage air-conditioning aystem using tetrabutylammonium bromide clathrate hydrate slurry. In *World Renewable Energy Congress-Sweden; 8-13 May; 2011; Linköping; Sweden*, number 057, pages 1118–1125. Linköping University Electronic Press, 2011.

[46] Z. Ma, P. Zhang, R. Wang, S. Furui, and G. Xi. Forced flow and convective melting heat transfer of clathrate hydrate slurry in tubes. *International Journal of Heat and Mass Transfer*, 53(19):3745–3757, 2010.

[47] A. Metzner and J. Reed. Flow of non-newtonian fluids—correlation of the laminar, transition, and turbulent-flow regions. *Aiche journal*, 1(4):434–440, 1955.

[48] A. Mills. *Heat Transfer*. Prentice Hall International Series in. Prentice Hall, 1999.

[49] National Center for Biotechnology Information. PubChem BioAssay Database. CID = 74236, 2016. https://pubchem.ncbi.nlm.nih.gov/compound/Tetrabutylammonium_bromide.

[50] Nederlands Normalisatie-Instituut (NNI). Nen 5060: 2008 hygrothermische eigenschappen van gebouwen–referentieklimaatgegevens, 2008.

[51] H. Ogoshi, E. Matsuyama, H. Miyamoto, T. Mizukami, N. Furumoto, and M. Sugiyama. Clathrate hydrate slurry, chs thermal energy storage system and its applications. In *International Symposium on Next-generation Air Conditioning and Refrigeration Technology, Tokyo, Japan*, 2010.

[52] H. Ogoshi and S. Takao. Air-conditioning system using clathrate hydrate slurry. *JFE Tech. Rep*, 3:1–5, 2004.

[53] H. Oyama, W. Shimada, T. Ebinuma, Y. Kamata, S. Takeya, T. Uchida, J. Nagao, and H. Narita. Phase diagram, latent heat, and specific heat of TBAB semiclathrate hydrate crystals. *Fluid Phase Equilibria*, 234(1):131–135, 2005.

[54] A. H. C. Paassen and L. Itard. Lecture notes Wb4426 Indoor Climate Fundamentals, 2016.

[55] S. C. Palmer, W. V. Payne, P. A. Domanski, et al. *Evaporation and condensation heat transfer performance of flammable refrigerants in a brazed plate heat exchanger*. Citeseer, 2000.

[56] J. Römer and M. Jong. Warmte- en koedevraagpatronen in de utiliteitsbouw. Technical report, ECN, 1999.

[57] L. Shi. Control model of a CO2 booster refrigeration system for supermarkets. Internship report, Mechanical Engineering, SPET, TU Delft, 2015.

[58] X. Shi and P. Zhang. A comparative study of different methods for the generation of tetra-n-butyl ammonium bromide clathrate hydrate slurry in a cold storage air-conditioning system. *Applied energy*, 112:1393–1402, 2013.

[59] X. Shi and P. Zhang. Cold storage by tetra-n-butyl ammonium bromide clathrate hydrate slurry generated with different storage approaches at 40 wt% initial aqueous solution concentration. *International Journal of Refrigeration*, 42:77–89, 2014.

[60] X. Shi and P. Zhang. Conjugated heat and mass transfer during flow melting of a phase change material slurry in pipes. *Energy*, 99:58–68, 2016.

[61] R. Singh and S. S. Kachhwaha. Heat transfer and pressure drop analysis of chilled water and ice slurry in a plate heat exchanger. *Journal of Thermal Science and Engineering Applications*, 8(1):011020, 2016.

[62] R. Sinnott and G. Towler. *Chemical engineering desig*. Butterworth-Heinemans, 2009.

[63] J. Tamasauskas, M. Poirier, R. Zmeureanu, and R. Sunyé. Modeling and optimization of a solar assisted heat pump using ice slurry as a latent storage material. *Solar Energy*, 86(11):3316–3325, 2012.

[64] D. G. Thomas. Transport characteristics of suspension: VIII. A note on the viscosity of Newtonian suspensions of uniform spherical particles. *Journal of Colloid Science*, 20(3):267–277, 1965.

[65] B. Thonon. Design method for plate evaporators and condensers. In *BHR Group Conference Series Publication*, volume 18, pages 37–50. Mechanical engineering publications limited, 1995.

[66] H. Van Putten and P. Colonna. Dynamic modeling of steam power cycles: Part II–Simulation of a small simple Rankine cycle system. *Applied Thermal Engineering*, 27(14):2566–2582, 2007.

[67] VDI-Gesellschaft Verfahrenstechnik und Chemieingenieurwesen. *VDI Heat Atlas*. Springer, Berlin, 2010.

[68] S. Wenji, X. Rui, H. Chong, H. Shihui, D. Kaijun, and F. Ziping. Experimental investigation on TBAB clathrate hydrate slurry flows in a horizontal tube: Forced convective heat transfer behaviors. *international journal of refrigeration*, 32(7):1801–1807, 2009.

[69] S. Wenji, R. Xiao, and Z. Feng. Experimental investigation on tetra-n-butyl-ammonium bromide clathrate hydrate slurry flows in a horizontal tube: Flow behavior and its rheological model. *HVAC&R Research*, 18(3):461–467, 2012.

[70] R. Xiao, S. He, C. Huang, and Z. Feng. Pressure-drop and energy-saving analysis of TBAB clathrate hydrate slurry as a and energy-saving analysis of TBAB clathrate hydrate slurry as a analysis of TBAB clathrate hydrate slurry as a of TBAB clathrate hydrate slurry as a clathrate hydrate slurry as a latent heat transportation media. 2007.

[71] R. Xiao, S. Wu, L. Tang, C. Huang, Z. Feng, et al. Experimental investigation of the pressure-drop of clathrate hydrate slurry (CHS) flow of tetrabutylammonium bromide (TBAB) in straight pipe. In *Proceedings of 10th International Conference on Thermal Energy Storage, NJ, USA*, pages 89–96, 2006.

[72] Y. Y. Yan and T. F. Lin. Evaporation heat transfer and pressure drop of refrigerant R134a in a plate heat exchanger. *Journal of Heat Transfer*, 121(1):118–127, 1999.

[73] J. Yang, A. Jacobi, and W. Liu. Heat transfer correlations for single-phase flow in plate heat exchangers based on experimental data. *Applied Thermal Engineering*, 113:1547–1557, 2017.

[74] H. Zak. Air-conditioning in office buildings performance-ratio between water and TBAB-hydrate slurry in AC-distribution systems applied to large office buildings. Msc thesis, Mechanical Engineering, SPET, TU Delft, 2014.

[75] P. Zhang and Z. Ma. An overview of fundamental studies and applications of phase change material slurries to secondary loop refrigeration and air conditioning systems. *Renewable and Sustainable Energy Reviews*, 16(7):5021–5058, 2012.

[76] P. Zhang, Z. Ma, Z. Bai, and J. Ye. Rheological and energy transport characteristics of a phase change material slurry. *Energy*, 106:63–72, 2016.

[77] P. Zhang, Z. Ma, X. Shi, and X. Xiao. Thermal conductivity measurements of a phase change material slurry under the influence of phase change. *International Journal of Thermal Sciences*, 78:56–64, 2014.

[78] P. Zhang, X. Shi, and Z. Ma. Solid fraction determination in cold storage by tetra-n-butyl ammonium bromide clathrate hydrate slurry. *international journal of refrigeration*, 36(3):809–819, 2013.

[79] P. Zhang and J. Ye. Experimental investigation of forced flow and heat transfer characteristics of phase change material slurries in mini-tubes. *International Journal of Heat and Mass Transfer*, 79:1002–1013, 2014.

[80] H. Zhou, C. Vasilescu, and C. Infante Ferreira. Heat transfer and flow characteristics during the formation of TBAB hydrate slurry in a coil heat exchanger. *International Journal of Refrigeration*, 64:130–142, 2016.

A

PROPERTIES OF HUMID AIR

The properties of humid air cannot directly be obtained from Fluidprop. However the properties of air and water can be used to calculate the properties of humid air. The water vapor fraction in air is usually expressed by the relative humidity. The definition of the relative humidity can be used to determine the partial pressure of the water vapor.

$$RH = \frac{P_{water}}{P_{water}^{sat}} \tag{A.1}$$

The partial pressure of the water vapor at saturation conditions is a function of the temperature of the air and can be calculated using Fluidprop. The humidity ratio of air is defined as the ratio of the mass of the water vapor divided by the mass of the dry air. It can also be expressed with the partial pressure of the water vapor.

$$\frac{m_{water}}{m_{air}} = 0.62198 \frac{P_{water}}{P_{air} - P_{water}} \tag{A.2}$$

In this equation 0.62198 is the ratio of the molar mass of water and air. The enthalpy of humid air can be expressed with the humidity ratio:

$$h = h_{air} + \frac{m_{water}}{m_{air}} h_{water} \tag{A.3}$$

The properties a humid air can also be shown graphically using in the Mollier diagram. This diagram is included in figure A.1. It provides an overview of the properties of humid air. The horizontal axis represent the humidity ratio of the air and the vertical axis is the temperature of the air. The curve started in the left bottom and going the the right top represent the saturation condition; the humid air at a relative humidity of 100%. This line can be used to determine the humidty ratio for a given air temperature. The diagram can also be used to determine the enthalpy for a given temperature and humidity and vice verse.
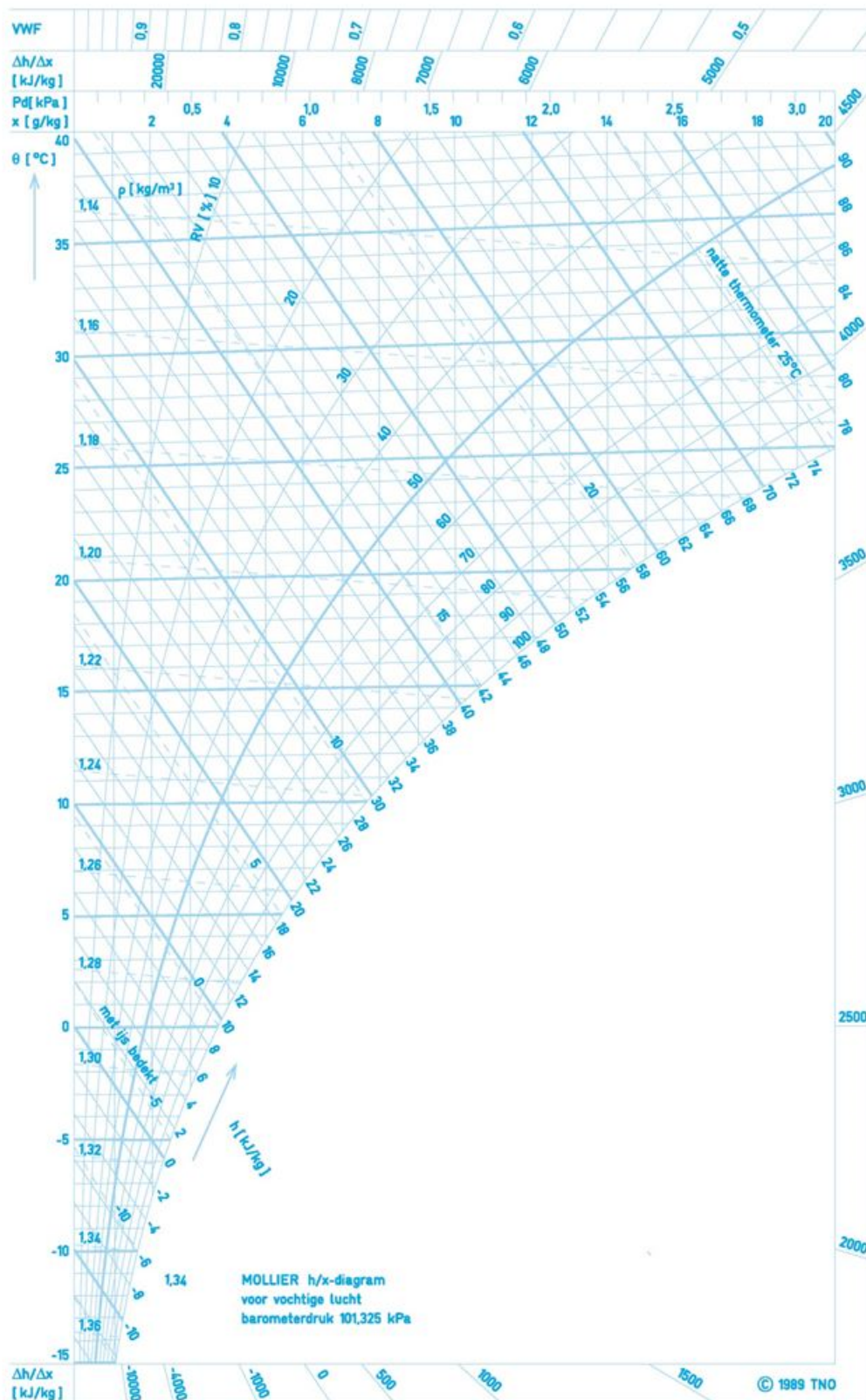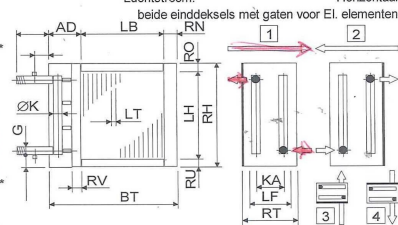
Figure A.1: The Mollier diagram.

B

THE SPECIFICATIONS OF THE AIR COOLER.

Koeler: 25/25/10-6R-30T-600A-4,2PA-15C-Cu/Al/Al

Vermogen totaal	kW	3,532	------ voelbaar:	3,288	
Oppervlak reserve	%	13,174	latent:	0,244	
Wisselaar oppervlak	m2	31,948	invries:	0,000	
Benodigd oppervlak	m2	28,229			
k-waarde vervuild	W/m2K	39,327	-------------- ffi:	0,000E+00	
dtm-kruis-tegenstroom	K	3,182	ffa:	0,000E+00	

Vochtige lucht

		in	uit	Definitie
Hoogte boven zeespiegel	m			0,000
Luchtdruk	hPa		1013,250	
Temperatuur	°C	20,000	13,500	20,000
Relatieve vochtigheid	%	65,000	96,114	65,000
Absolute vochtigheid	g/kg	9,454	9,259	
Dichtheid	kg/m3	1,197	1,224	
Enthalpie	kJ/kg	44,116	36,968	
Hoeveelheid	m3/h	1500,000	1466,289	1500,000
Massastroom droge lucht	kg/h	1778,777	1778,777	
Kondenshoeveelheid	kg/h		0,347	
Oppervlakte temperatuur	°C	15,418	12,354	
Aanstroom snelheid	m/s	0,926	0,905	
Drukverlies (droog 11 Pa)	Pa		11,608	

Water

		in	uit	gemiddeld
Temperatuur	°C	12,000	14,000	13,000
Dichtheid	kg/m3			999,449
Spec.warmte	kJ/kgK			4,191
Warmtegeleiding	W/mK			0,592
Dyn.viscositeit	Pas			1,198E-03
Hoeveelheid	m3/h			1,518
Snelheid	m/s			0,412
Drukverlies	kPa			4,251

Afmetingen, gewicht, materiaal

Pijpen totaal		aantal	180	WT-Pijpen:	glad	Cu
Pijpen blind		aantal	0		evenwijdig	
Interne ontluchting		aantal		Verzamelaar:		Cu
Interne aftap		aantal		Aansluiting:		Rg7
Pijprijen diep		aantal	6	Lamellen:	zig-zag	Al
Pijprijen hoog		aantal	30	Frame:	2,0 mm	Al
Pijpen per groep		aantal	12			
Groepen (NC)		aantal	15	Bescherming:		geen
Inhoud		l	9			---
Gewicht		kg	28	El. insteek elem.:		---
Aansluiting	G	---	1¼"	Luchtstroom:		Horizontaal
Frame hoogte	RH	mm	800	beide einddeksel met gaten voor El. elementen		
Frame breedte	BT	mm	735			
Frame diepte	RT	mm	190 *			
Lamel hoogte	LH	mm	750			
Lamel breedte	LB	mm	600			
Lamel diepte	LF	mm	150			
Frame flens boven	RO	mm	25			
Frame flens onder	RU	mm	25			
Frame flens voor	RV	mm	15			
Frame flens achter (~43mm)	RN	mm	35			
Verzamelaar maat	K	mm	35 *			
Verzamelaar afdekking	AD	mm	100			
Verzamelaar afst. diepte	KA	mm	128			
Lamel afstand	LT	mm	4,200	Levertijd:		7-8 weken na goedkeuring
Lamel dikte	LD	mm	0,250	Geldigheid:		12 weken
Pijpmaat	DA	mm	10,120	Condities:		netto, af fabriek, verpakt, excl. BTW
Pijpwand	S	mm	0,400	Betaling:		30 dagen netto
Pijpverdeling in de hoogte	S1	mm	25,000	**Prijs netto:** Geen el. ontdooiin	**EUR**	#WAARDE!
Pijpverdeling in de diepte	S2	mm	25,000			

C

THE PUMP CHARACTERISTIC

The pump characteristic provided by the manufacturer are shown in figure C.3 and figure C.3. The data from this two graphs has been used to construct the data the pump characteristic for different rotational velocities according to the method described in section 5.3. The result for the smallest pump is shown in figure C.1 and the result for the largest pump is shown in figurefig:M4.
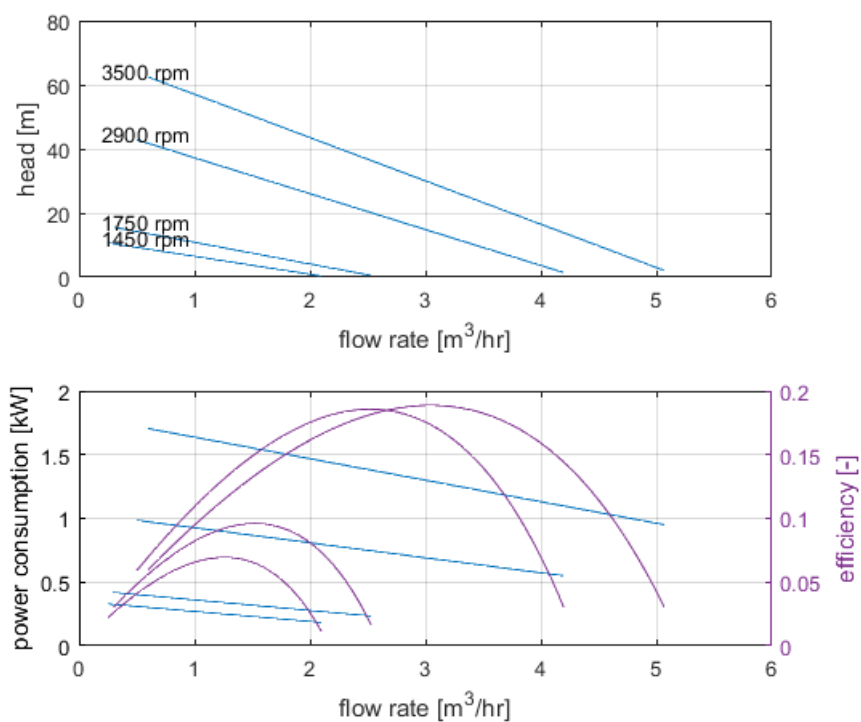
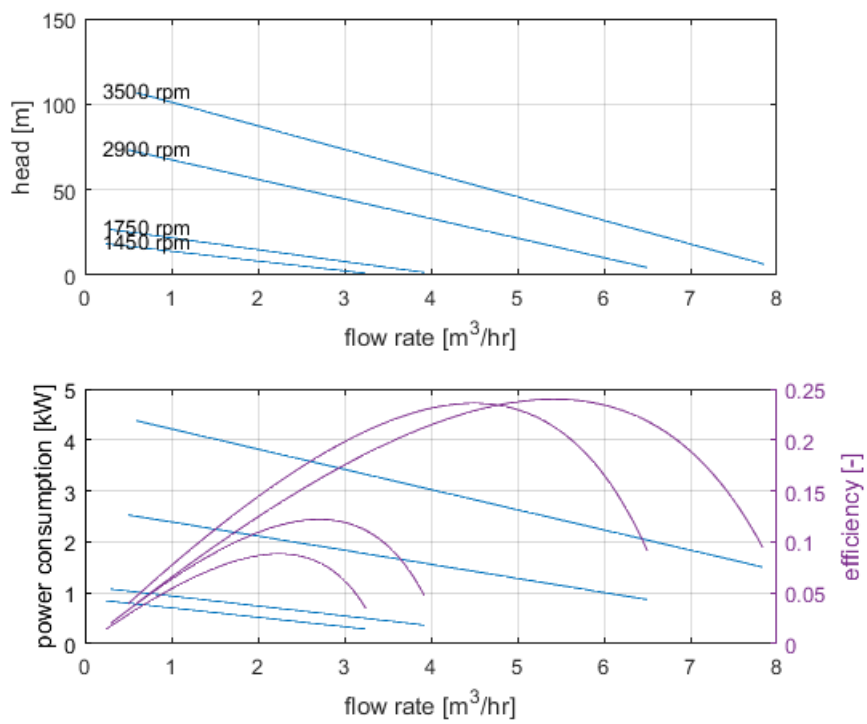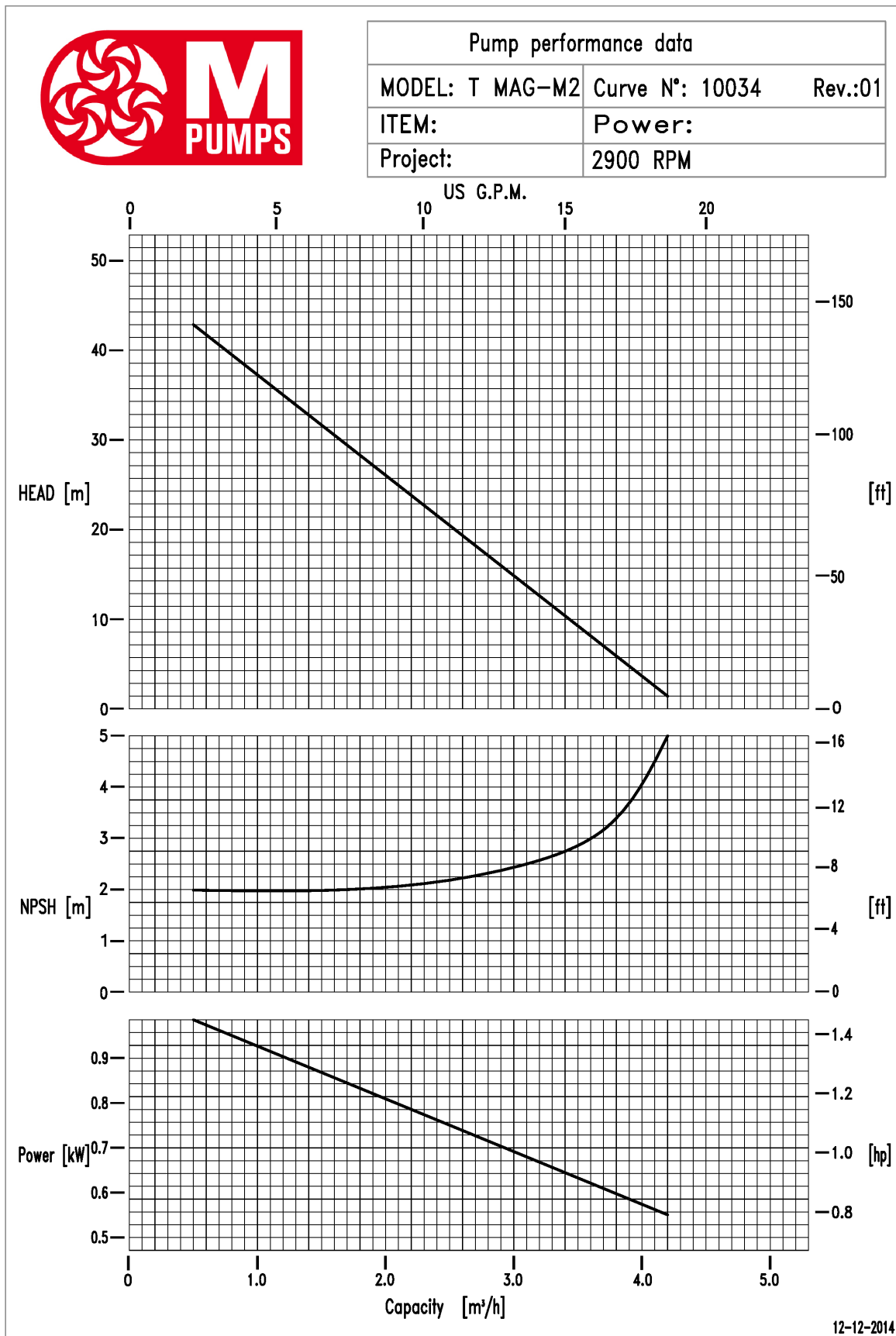

Figure C.1: The pump characteristic of the T MAG-M2 pump.

Figure C.2: The pump characteristic of the T MAG-M4 pump.

Figure C.3: The pump characteristic of the T MAG-M2 pump as published by manufacturer.
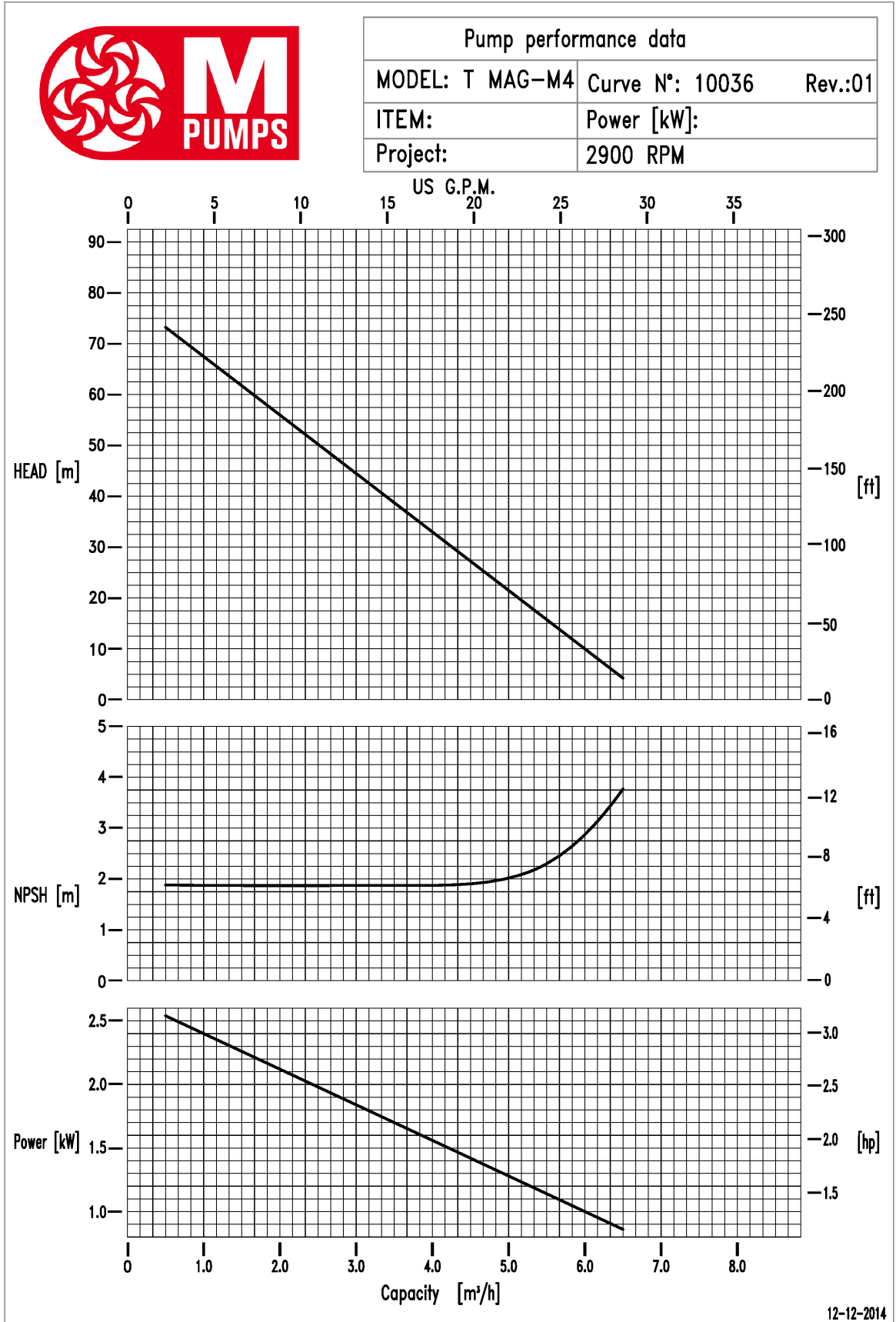
Figure C.4: The pump characteristic of the T MAG-M4 pump as published by manufacturer.

D

EXTENDED STORAGE MODEL

An extended storage model has been developed in order to describe the distribution of the crystals throughout the storage tank. This model has many similarites to the model of Flick et al. [24] and Douzet et al. [21] however the model is modified in order to also describe the inflow and presence of superheated solution. The model divides the tank into a number of volume elements each with a constant volume V and a height dx. The model uses the following assumptions:

- All the properties of the fluid are constant in a volume element.

- The volume elements are at equilibrium temperature as long as the solid mass fractions is higher then 0.

- The diffusion of the crystals is neglected.

- The crystal are assumed to be spherical with always the same diameter.

The velocity of the crystals V_c and the velocity of the solution V_{sol} is calculated with the entering mass flow, thevolume fraction of the crystals and the settling velocity. The settling velocity of the crystals is defined as the difference between the velocity of the crystals and the velocity of the fluid. It is determined with the modfied Stokes law as derived by Flick et al. [24]. The maximum volume fraction is assumed to be 0.65 based on observations of Darbouret et al. [17].

$$v_{set} = g \frac{(\rho_c - \rho_{sol})d_c^2}{18\mu_{sol}} \left(1 - \frac{\phi_c}{\phi_{c,max}}\right) \tag{D.1}$$

BALANCE EQUATIONS
For every element in the tank an energy balance and a species balances are solved. Each volume element of the tank can also be represented by two different elements: one for the crystals and one for the solution. The relation between these elements is given by the volume fraction of the crystals.

$$m_c = V\rho_c\phi_c \tag{D.2}$$

$$m_{sol} = V\rho_{sol}(1 - \phi_c) \tag{D.3}$$

$$\tag{D.4}$$

In a similar fashion the velocity of the crystals and the solution can be rewritten as mass flows. These mass flows are used to solve the balance equations. Two distinct situations are distinguished: the solution is or becomes superheated or the solution is at the equilibrium temperature. For each situation a different set of equations is solved by iteration.

THE SOLUTION IS AT THE EQUILIBRIUM TEMPERATURE
The solution is only at its phase equilibrium temperature if there are crystals present. The crystal mass fractions is calculated be solving the energy balance:

$$-\Delta h_{melt}\frac{m_c^{t+\Delta t} - m_c^t}{\Delta t} + C_{p,sol}\frac{m_{sol}^{t+\Delta t}T^{t+\Delta t} - m_{sol}^t T^t}{\Delta t} + \dot{Q}_{out} - \dot{Q}_{in} = 0 \tag{D.5}$$

The heat flows are the sum of all the heat flows entering or leaving the volume element. This include the heat flow as a result of conduction through the fluid, conduction through the insulation material and the heat flow resulting from the mass flows. The TBAB mass concentration is found using a species balance:

$$\frac{m_c^{t+\Delta T} w_{TBAB,c} - m_c^t w_{TBAB,c}^t}{\Delta t} + \frac{m_{sol}^{t+\Delta T} w_{TBAB}^{t+\Delta t} - m_{sol}^t w_{TBAB}^t}{\Delta t} + [\dot{m}_c w_{TBAB,c}]_{in}^{out} + [\dot{m}_{sol} w_{TBAB}]_{in}^{out} = 0 \qquad (D.6)$$

Finally the TBAB mass concentration can be used to determine the temperature of the solution. The solution is at phase change temperature:

$$T^{t+\Delta T} = T_e \qquad (D.7)$$

THE SOLUTION IS SUPERHEATED

The solution can only become superheated if there following condition must met:

$$\phi_c^{t+\Delta T} = 0 \qquad (D.8)$$

The concentration of TBAB is determined using a species balance:

$$\frac{m_c^{t+\Delta T} w_{TBAB,c} - m_c^t w_{TBAB,c}^t}{\Delta t} + \frac{m_{sol}^{t+\Delta T} w_{TBAB}^{t+\Delta t} - m_{sol}^t w_{TBAB}^t}{\Delta t} + [\dot{m}_c w_{TBAB,c}]_{in}^{out} + [\dot{m}_{sol} w_{TBAB}]_{in}^{out} = 0 \qquad (D.9)$$

Finally the temperature can be determined using an energy balance:

$$-\Delta h_{melt} \frac{-m_c^t}{\Delta t} + C_{p,sol} \frac{m_{sol}^{t+\Delta t} T^{t+\Delta t} - m_{sol}^t T^t}{\Delta t} + \dot{Q}_{out} - \dot{Q}_{in} = 0 \qquad (D.10)$$

SIMULATIONS

The performance of the model has been investigated by modeling several different situation. Each simulations starts with a storage tank with an initial TBAB concentration $w_{TBAB,0}$ of 0.365 and a crystal volume fraction ϕ_c of 0.40. The simulations were performed for three different situations:

- Situation 1: there is no inflow in the storage tank, so the main phenomenon occurring in the storage tanks is the settling of the crystals.

- Situation 2: an super heated mass flow of 0.01 kg/s and a temperature of 15 °C flows into the top the tank.

- Situation 3: an mass flow of 0.5 kg/s and a temperature of 15 °C has been applied to the inlet. The mass flow is in the same range as the actual mass flows encountered in the system.

The simulation result for situation 1 are presented in figure D.1. The figure shows that the model provides and description of the settling of the crystals. The settling process slows down when the solid volume fraction comes closer to the maximal solid fraction. It also hows that a layer with almost now crystal will be formed at the top of the storage tanks and that this layer will slowly extends downwards.

If the the crystal size is reduced from 100 μm to 50 μm then it takes more then 3 hours before a solid fraction of 0.55 is reached at the bottom of the tank. That means that the settling process will be more then three times slower. The actual size and shape of the produced crystals is unknown. Therefore it is very difficult to use the model to predict the settling of the crystals. The large dependence on the crystal diameter can easily be explained by equation D.1. The settling force scales with the volume of the crystals while the settling resistance scales with the area of the crystals.

The results of the simulations for situation 2 are shown in figure D.2. In this situation there are two distinctive layers formed. The layer of the superheated solution will be formed on top of a layer of the original solution. There also is a region in which the two layers have been mixed. The smooth transition between the two layers with a different mass fractions is mainly due to additional diffusion created by the control volume elements. As shwon in the figure reducing the size of the volume elements results in a much more sudden transition; this is just as expected since the diffusion of the crystals is neglected. It also means that the size of the control volume elements should be reduced in order to improve the accuracy of the model. However this also means that the time step should be reduced, resulting in a much larger calculation time.

As mentioned earlier the models predicts only a small boundary layer between the two models. This is also observed in the model of Douzet et al. [21] in which the discussion is included. This result is mainly due to the fact that flow in the radial direction are neglected. Therefore the mixing fluid is underestimated.
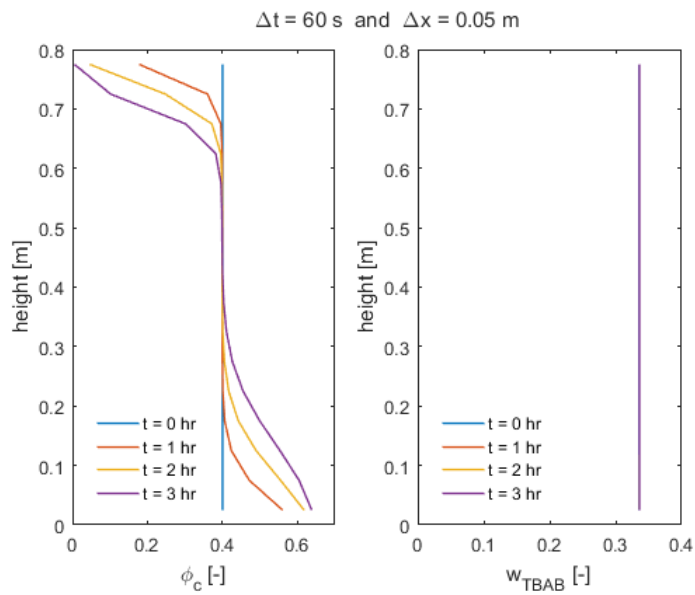
Figure D.1: The vertical distribution of ϕ_c and w_{TBAB} as predicted by the storage model for an entering mass flow of 0 kg/s (situation 1).
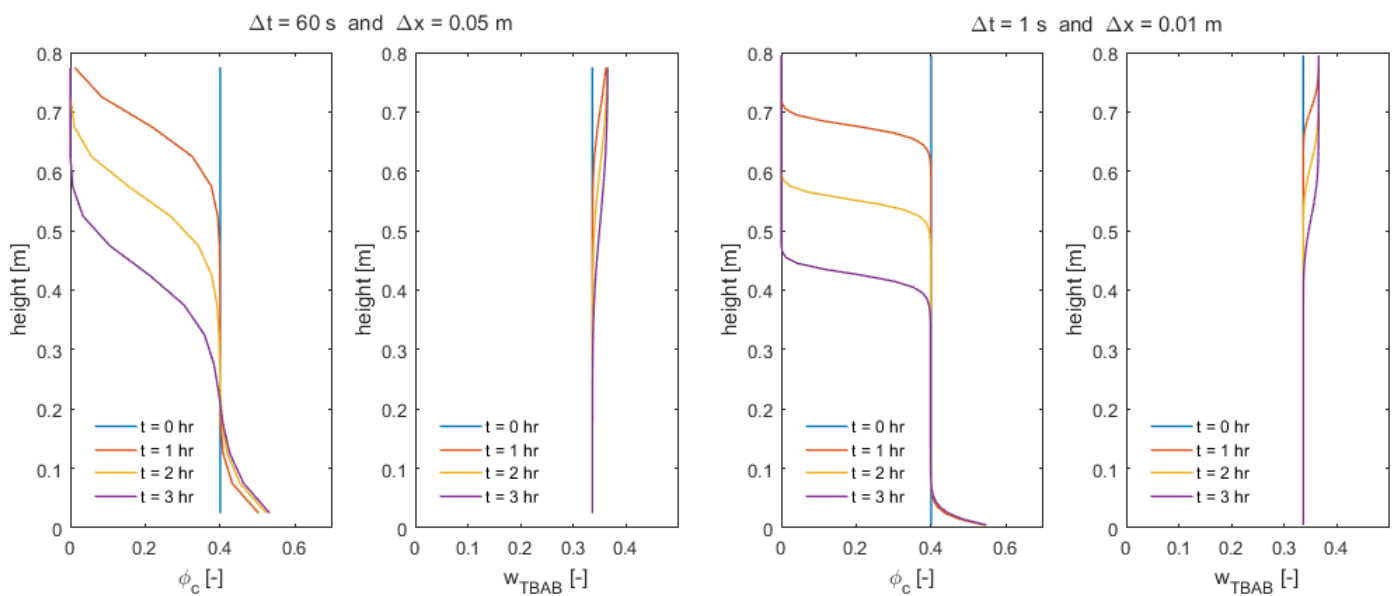

Figure D.2: The vertical distribution of ϕ_c and w_{TBAB} as predicted by the storage model for an entering mass of 0.01 kg/s (situation 2).

Figure D.3 show the results of the simulation done for situation 3. The results for a simulation time of 1, 2 and 3 hours are exactly the same. It takes 10 minutes to completely fill the storage tank if a mass flow of 0.5 kg/s is applied. In reality the entering mass flow will be dependent on the leaving mass flow and some delay. This delay however is not included in the model of the system. The model of the system uses a time step of one hour. It is possible to use a different time step for the calculations for the storage tank. However figure D.3 shows that this storage model will not improve the accuracy for a time step of on hour due to the large mass flows encountered in the system. This means that the dynamic effects happen at a much smaller time scale then the time step of one hour. This means that even if the dynamic effects are described by the storage tank that these dynamic effects will be neglected in the models of the other components.
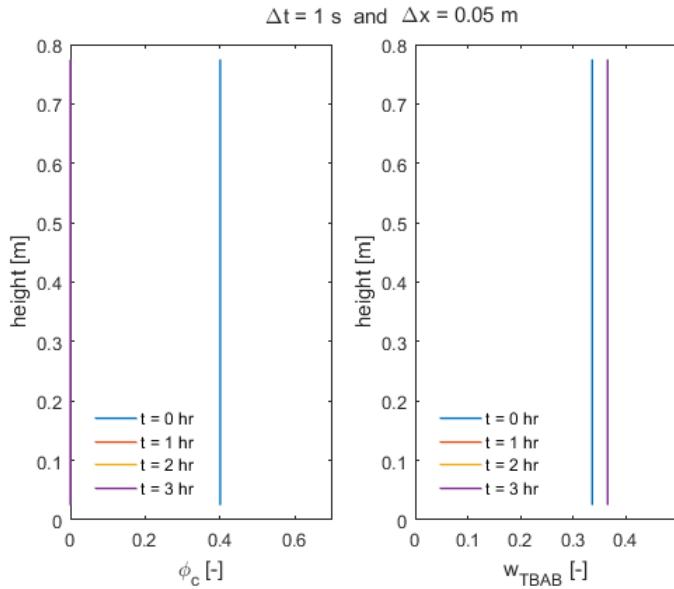

Figure D.3: The vertical distribution of ϕ_c and w_{TBAB} as predicted by the storage model for an entering mass of 0.5 kg/s (situation 3).

E

THE DATA COLLECTION IN THE SYSTEM

The experimental data is collected from the pilot plant in Twello. The system include a number of sensor each collecting a data point once every 10 seconds. Unfortunately the power sensors are not working properly and no consistent relation correlation between the measured value and the expected power consumption could be found.

An overview of all the sensors within the system is given in table E.1 and figure E.1. The accuracy of the sensors is when known presented in the third column of table E.1. The heat flows in the systems are determined using an energy balance:

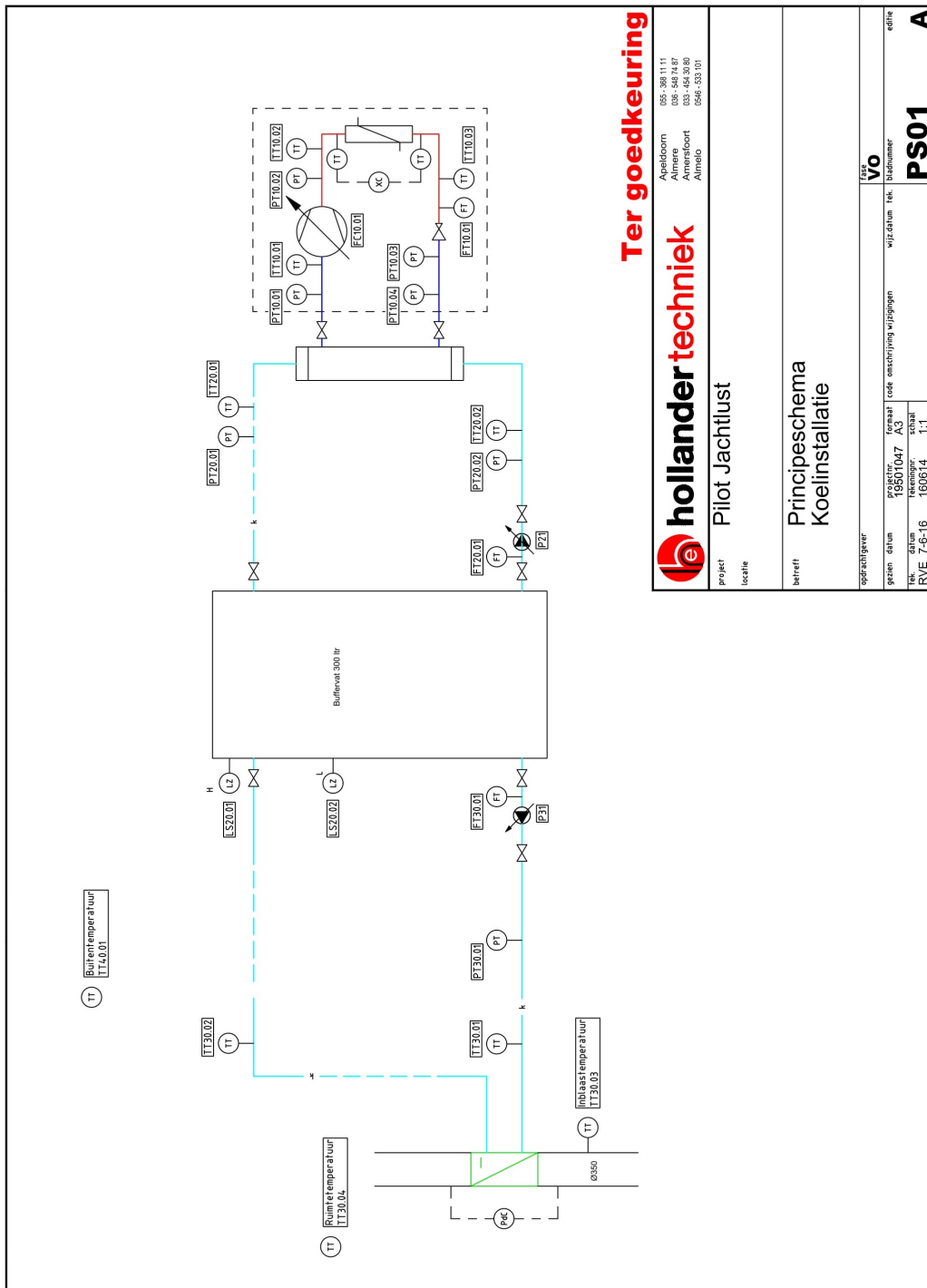$$\dot{Q} = \dot{m}\Delta h \tag{E.1}$$

These equations only offer a rough estimate of the power consumption since they do not include the energy transfer to the surrounding and the equipment. The thermal mass of the system often leads to a delay in the temperature measurement. The precision of the experimental data is limited by the number of decimals in which the data is saved. For example the pressure sensors have an accuracy of 1 kPa however the data is saved using two digits. As a result the available data has only a precision of 0.1 bar. This precision due to the rounding of the data is included in the second last column of table E.1.

Table E.1: On overview of the sensors in the system. When known the accuracy of the sensor is also included in the table as well as the precision due to rounding of the experimental data.

Sensors	Property	Accuracy	Precision data	Unit
FT10.01A, FT20.01A, FT30.01A	Density	-	0.1	[kg/m^3]
FT10.01B, FT20.01B, FT30.01B	Flow rate	0.15 %	0.1	[kg/h]
M10Power, P21Power, P31Power	Power	-	1	unknown
M10Spd, P21Spd, P31Spd	Rotational speed	-	1 %	[%]
PT10.01, PT10.02, PT10.03, PT10.04, PT20.01, PT20.02, PT30.01	Gauge pressure	0.01	0.1	[bar]
TT10.01, TT10.02, TT10.03, TT20.01, TT20.02, TT30.01, TT30.02, TT30.03, TT30.04, TT40.01	Temperature	0.03	0.1	[K]
V10.01	Valve	-	0.1	[%]

Not only the sensors but also the setup might influence the accuracy of the results. The pressure and temperature sensors are located in the pipes which connect the different components of the system. The

sensors are usually located somewhere in the middle of these pipes so the pressure sensors are not measuring the complete pressure drop in the pipes. Furthermore, the pressure sensors are not located at the same distance from the floor. As a result, the pressure measurements might also be affected by the hydrostatic pressure. These inaccuracies however can only account for small deviations (maximum about 0.1 bar) in the measured pressure drop.

Figure E.1: An overview of the system with the placement of the sensors.